UNIVERSITY OF CALIFORNIA
RIVERSIDE

Neuropathology, Neurodegeneration and Axon Loss During Alzheimer's Disease

A Dissertation submitted in partial satisfaction
of the requirements for the degree of

Doctor of Philosophy

in

Neuroscience

by

Christopher Arata Nishioka

September 2018

Dissertation Committee:
Dr. Richard Sun, Co-Chairperson
Dr. Iryna Ethell, Co-Chairperson
Dr. Seema Tiwari-Woodruff

The Dissertation of Christopher Arata Nishioka is approved:

_____

_____
Committee Co-Chairperson

_____
Committee Co-Chairperson

University of California, Riverside

Acknowledgements

The text of this dissertation, in part is a reprint of materials as they appear in the Journal of Alzheimer's Disease, March 2015; Journal of MRI, February 2017 as well as recently submitted manuscripts to Multiple Sclerosis and Related Disorders and Neuroimage. The co-author, Dr. Richard Sun directed and supervised the research which forms the basis for this dissertation.

Thanks to several UCR undergraduate and LLU medical students including Barsam Barsamanian, Jennifer Mei, Christina Poh, Andrea Cragoe, Samantha Luna, David Wooten and Chloe Su.

Advisory support from UCR and LLU faculty, including Richard Sun, Wei-xing Shi Iryna Ethell, Seema Tiwari Woodruff, and Hyle Park.

A very special thanks to my colleagues Ariel Liang, Stephen Ong and Aiken Chung who I owe a great deal for helping me during my time in graduate school.

Dedication

For my wife, May Nishioka, whose encouragement, love and support were the most important part of this journey.

ABSTRACT OF THE DISSERTATION

Neuropathology, Neurodegeneration and Axon Loss during Alzheimer's Disease

by

Christopher Arata Nishioka

Doctor of Philosophy, Graduate Program in Neuroscience
University of California, Riverside, September 2018
Dr. Richard Sun, Co-Chairperson
Dr. Iryna Ethell, Co-Chairperson

This dissertation seeks to clarify links between non-invasive radiological and optical biomarkers, neuropathology and neurodegeneration within axon tracts during neurodegenerative disease, with focus on Alzheimer's Disease (AD). Data contained in these studies were gathered from a variety of different model systems with different modes of neurodegeneration relevant to human clinical findings. Our studies utilized the visual system to model the axonal degeneration process and evaluate biomarkers of axon tract injury. First, a comprehensive analysis of visual system white matter integrity was performed in AD, MCI and control patients, using diffusion tensor images (DTIs) drawn from the Alzheimer's Disease Neuroimaging Initiative. Our findings establish the visual system as a white matter pathway affected during AD. Next, we used a retinal ischemia model to characterize spatiotemporal patterns of axonal degeneration in the visual system by DTI in Wallerian Degeneration Slow mice. Our results reveal an ability to identify propagating anterograde degeneration along the optic nerve and tract. Next, we used a Experimental Autoimmune Encephalomyelitis model to simulate retrograde axonal

degeneration in the visual system and characterize the longitudinal relationship between DTI-measured axon loss and optical coherence tomography measured retinal thinning.

Our data clarify the relationship between the biomarkers, and establish the correlation between each and magnitudes of axon loss. Next, we evaluated whether axonal transport function, a key putative factor in AD-related axonal degeneration could be related to DTI properties in the p301L tau transgenic model using Manganese-enhanced MRI. Our data expose a novel connection between restricted diffusion in the ON and compromised axonal transport function. Lastly, we tested whether retrograde axonal degeneration could be triggered by Aβ-induced tau pathology. Our results reveal a temporal pattern of damage that appears to emanate from the presyanpse toward cell bodies, and result in loss of white matter integrity in a manner similar to what is observed in humans during AD. Additionally, our experiments reveal the critical role of initial Aβ-induced tau phosphorylation, and imply that blocking this step by microtubule-stabilizing compounds may prevent downstream axon and cell loss. This process may be integral to understand the widespread white matter damage observed in Alzheimer's Disease.

TABLE OF CONTENTS

List of Figures

Introduction

Alzheimer's Disease (AD) was first characterized clinically and pathologically in 1906 by German neuropathologist Dr. Alois Alzheimer. Over 100 years later, AD is recognized as the most common neurodegenerative disease, affecting more than five million Americans in 2017 [1]. It is the 6th leading cause of death in the United States, with no available disease-modifying treatments to alter the disease course. Pathologically, the disease is identified by the presence of extra-cellular Amyloid-β (Aβ) plaques, intracellular neurofibrillary tangles (NFTs) in the brain and gradual brain atrophy. Clinically, the disease is characterized by devastating progressive, age-related decline in learning, memory and executive function. These impairments are substantial and become debilitating, necessitating round-the clock care for any affected individual. The cognitive decline during disease is paralleled by dysfunction and degeneration in brain networks, likely precipitated by disease pathology. These networks are composed of axon tracts, which integrate and process information in the Central Nervous System. Myelinated axons in these networks are fragile structures, in some cases stretching up to a meter in length, necessitating careful homeostatic balance for survival. This includes processes to regulate axonal transport, protein synthesis and degradation, cytoskeletal maintenance and energy production. Meeting these requirements are especially challenging in neurons with long axons, making axons a critical failure point in neurons during disease. Indeed, axon loss is a defining feature in AD, with projection neurons being disproportionally impacted [2]. Loss of axons is likely an important contributor to the observed deficits to brain network functional connectivity and coincident cognitive decline [3, 4].

While axons are lost during AD, it remains unclear what process underlies this specific pathology and whether this damage arises as a result of axon-specific insult. In response to injury, axons may degenerate in response to specific triggers; this is typically followed by retrograde degeneration resulting in later cell body loss [5, 6]. Alternatively, axons can degenerate as a consequence of initial cell body apoptosis [5-7]. While degenerative events in the cell body and axon are typically closely connected, they represent two distinct processes. Discovery of the spontaneous mutant Wallerian Degeneration Slow (WldS) mouse strain, which over-expresses a chimeric protein consisting of full-length Nicotinamide Mononucleotide Adenylytransferase 1 (NMNAT-1) and a fragment of the E4 ubiquitination factor (UBE4b), revealed that mechanisms governing axonal degeneration are different from those involved in cell body apoptosis [8, 9]. Neurons from these mice maintain functionally viable axons weeks after cell body apoptosis or axonal transection [8]. In contrast to axons, the WldS genotype appears to have no effect on the process or timing of cell body apoptosis [10, 11]. Several studies have narrowed the site of action of the WldS protein to the axonal compartment, and suggest that the protective effect of WldS may stem from substituting for NMNAT-2 depletion after axonal injury [12, 13]. Additional studies have identified several other proteins that appear to influence the process of axonal degeneration selectively [14-16]. Collectively, these findings demonstrate that the axon maintains a specialized destruction program that can initiate axonal degeneration in response to specific triggers. These triggers likely include several pathways but are thought to include activation of Death Receptor 6 (DR6) by APP, axonal transport defects and depletion of nicotinamide adenine dinucleotide

(NAD) [16-18] These findings raise important questions about the influence of different pathological triggers in AD on the process of axon loss. Currently, it remains uncertain whether axon-specific mechanisms may play a role in the observed axonal damage and loss.

Axon tract integrity is most commonly assessed *in vivo* through the use of noninvasive imaging techniques such as Diffusion Tensor Imaging (DTI). This technique is in widespread use to measure degeneration that occurs within white matter (axon loss and / or demyelination) during disease. Several lines of evidence suggest that DTI-detectable changes in white matter are paralleled by increases in canonical brain pathology during AD . However, the noninvasive nature of these biomarkers makes defining causal relationships difficult. It is yet unclear how these radiological biomarkers reflect disease-associated forms of axon loss or demyelination that can be clearly attributed to specific brain pathologies. Therefore, modeling these disease-associated forms of axonal degeneration is imperative for interpreting clinical datasets and testing new therapeutics to block these disease outcomes.

The study of axon loss during AD has traditionally only been possible though the use of functional assessments or histology from post-mortem samples. Accurate assessments of these changes are of utmost importance, given the devastating clinical effects perpetrated by AD. The advent and widespread adoption of clinical MRI has facilitated *in vivo* study of axon tracts within the brain by exploiting grey/white matter contrast from conventional MRI (T1/T2) sequences. Early volumetric studies comparing white matter volume between AD and control patients noted differences in corpus

callosum volume as well as prefrontal white matter volume [19, 20]. Studying alterations to white matter tracts during disease took on new dimension with the rise of diffusion-weighted imaging. Diffusion-weighted imaging, and its common application model, Diffusion Tensor Imaging (DTI) employ diffusion-sensitizing gradients, which allow assessment of the Brownian motion of water molecules in a particular direction within imaging voxels [21]. As random diffusion of water is shaped by structural elements (cell membranes, myelin sheaths, organelles) and their geometry within each imaging voxel the diffusion signal and derived DTI metrics reflect collective underlying tissue microstructure. These alterations to microstructure are not always detectable using standard MRI and provide a more sensitive metric to evaluate degeneration in the brain [22-24] . DTI is especially sensitive to changes that occur in white matter, due to its intrinsically ordered structure composed of bundles of myelinated axons. The ordered structure creates diffusional anisotropy (Fractional anisotropy or relative anisotropy, FA / RA), due to relatively free diffusion along the principal axis of fibers (Axial diffusion, AxD), and relatively restricted diffusion across fibers and myelin sheaths (Radial diffusion, RAD). The total magnitude of diffusion (AxD + RAD) is represented as TR, or the trace of diffusion. Under neurodegenerative conditions, loss of white matter tissue structure (by losing axons and/or myelin) leads to increases in diffusion across fibers, which necessarily decreases FA with coincident increases in RAD/TR. These changes are often referred to as signaling loss of "white matter integrity", which is a pathologically nonspecific term that may indicate demyelination, axonal degeneration or some combination of the two. Animal model studies suggest that DTI measurements may be

useful in acute circumstances to discriminate between axonal degeneration (reductions in AxD) from demyelination (increases in RAD) [25-27]. Measurements derived from DTI have been instrumental in defining the temporospatial profile of white matter disruption during prodromal, early and late stages of AD [28].

Since the development and subsequent widespread adoption of DTI in clinical settings beginning around 2000, many studies have examined microstructural white matter integrity in cognitively healthy patients in comparison to those with AD and its putative prodromal form Mild cognitive impairment (MCI). These studies often utilize a non-biased whole brain analysis approach termed Tract-Based Spatial Statistics "TBSS", allowing simultaneous, automated analysis of all major white matter tracts in the brain [29]. From these studies, several common findings have emerged. Among healthy aging populations, gradual loss of white matter integrity correlates with increasing age [30]. While reductions in white matter integrity seem to be a general feature of aging, patients in AD have an extreme version of these deficits. Patients with AD (and to a lesser extent MCI) manifest with significant reductions in FA and increases in RAD / TR in several specific white matter tracts, relative to age-matched healthy controls. While results from individual studies vary, regional differences between AD and controls typically include the forix, uncinate fasciculus, superior longitudinal fasciculus, posterior cingulum, genu and splenium of the corpus callosum [28, 31, 32]. These regions appear to be selectively vulnerable in AD, and may show integrity changes at the earliest clinical stage during MCI. The degree of these alterations in vulnerable regions correlates with cognitive

measures in AD patients, and may be useful to predict clinical conversion between MCI and AD [33-35].

Despite a wealth of DTI studies characterizing the alterations to white matter during AD and MCI, the relationships between specific forms of brain pathology and focal alterations to white matter tracts are not clear. However, biomarker data gathered during the course of DTI studies can help contextualize the findings and may be useful to understand the factors involved in changing microstructural integrity. Recent work has focused on CSF biomarkers of the two most high-profile pathological factors in AD, Aβ and tau. Both proteins are thought to play neurotoxic roles in AD, when they accumulate in neurons (tau) and in extracellular plaques (Aβ). Levels of Aβ in the CSF decrease during AD, likely reflecting enhanced retention in the brain, while levels of tau and its hyperphosphorylated variant increase, potentially reflecting release from neurons. These biomarkers give clues about the general levels of these proteins in the brain, but offer no information about their spatial distribution. Several studies have identified significant relationships between elevated levels of tau and reductions in white matter integrity (decreased FA, increased RAD). Stenset et al. found relationships between elevated CSF tau and changes in Cingulum integrity by DTI [36]. A similar correlation was identified between total CSF Aβ and Cingulum FA in AD patients [37]. These trends also appear in cognitively healthy adults with family history of AD. Bendlin et. al found tau and tau/Aβ levels at baseline correlated to changes in white matter integrity 3.5 years later, in regions adjacent to gray matter structures affected in early stages of the disease [38]. In a detailed clinical study by Kantarci et. al. cognitively healthy and MCI patients were stratified as

Aβ+/- (assessed using Aβ tracer 11-C Pittsburgh compound-B PET) and neurodegeneration +/- (using high resolution structural MRI of the hippocampus and hypometabolism via FDG PET). This study revealed that FA reductions in the Fornix (the most vulnerable white matter tract assessed in the study) were not associated with amyloid load without coincident neurodegeneration [39]. However, MCI patients both Aβ+ and neurodegeneration+ had more widespread FA decreases than patients classified as Aβ- and neurodegeneration+. This study suggests that Aβ may play a role in white matter damage as the disease progresses, though may not be sufficient by itself. A study by the same research group has recently made the first comparisons between antemortem DTI and postmortem histopathology in AD patients. This study found significant relationships between extent of tau neurofibrillary tangle (NFT) pathology (Braak stage) and FA/Trace Diffusion in several vulnerable white matter tracts, including the Fornix and Cingulum [40]. Collectively, these results suggest that tau and its aggregate form in NFTs may play a central role, with Aβ playing a supporting role in causing white matter disruption and axon loss.

Amyloid-beta is thought to play a critical initiation role during AD. Derived from the Amyloid Precursor Protein (APP), Aβ is released from presynaptic terminals after APP is sequentially cleaved by β and γ secretase enzymes. Aggregates of Aβ in brain tissue of AD patients are a cardinal feature of the disease. Several lines of evidence suggest that Aβ may play a central role in disease pathogenesis. Mutations in either APP or elements of the Aβ processing pathway are known to cause autosomal dominant, early onset familial forms of AD [41]. These genetically linked cases of AD are thought to result

from either an increased level of Aβ generation or enhanced production of an aggregation prone form of the peptide [41]. While the fraction of familial AD cases among overall AD patients is low (~1-5% of total), they share identical neuropathological features, which has helped establish the importance of Aβ to disease onset [41]. Studies assessing Aβ deposition noninvasively (by Positron Emission Tomography, PET) have established that among aged adults, worsening cognitive status (In Healthy Control, MCI and AD patients) is associated with a greater share scored as Aβ+ [42, 43]. Interestingly, 14% of healthy control aged adults scored as Aβ+. These patients perform significantly worse than Aβ- patients in tests of verbal and visual episodic memory, and show greater declines on cognitive tests after 36 months [43, 44]. These data and others strongly implicate Aβ accumulation in the process of disease initiation. However, several studies have noted poor correlation between amyloid load assessed by histology and cognitive status in AD patient brains at autopsy [45-47]. Additionally, numerous clinical trials testing drugs which target Aβ, either by preventing aggregation, production or direct removal have generally failed to measurably alter AD progress [48]. These findings suggest that Aβ deposition is critical to trigger disease, but may not drive disease progress. Altering disease progress may require targeting processes presumed to occur downstream, such as the onset of tau NFT pathology. Notably, tau NFT pathology has been shown to correlate with cognition and neurodegeneration to a greater extent than Aβ pathology [49, 50].

Neurofibrially tangle pathology in the brain, originally identified by Alois Alzheimer, is composed of abnormal aggregations of insoluble, hyperphosphorylated tau. The shift from normal to disease-associated forms of tau is presumed to be a crucial step

that opens the door for neuronal dysfunction and/or death. Under basal conditions, tau is a primarily a neuronal protein enriched in the axonal compartment [51]. The protein exists as six main alternatively spliced isoforms, that differ based upon an N-terminal region and a repeat microtubule binding domain [52, 53]. The protein is subject to numerous post-translational modifications, including >80 potential phosphorylation sites [54]. In healthy neurons, tau is lightly phosphorylated (2-3 moles of phosphate per mole protein) and is primarily bound to microtubules in the axon [55]. Several lines of evidence suggest that this association may be important to regulate microtubule assembly and stability [56-58]. In addition to microtubules, tau is also known to bind to an array of different kinases, cytoskeletal proteins and signaling lipids, hinting that tau may have a wide variety of potential roles beyond that of a cytoskeletal protein in the axon [59].

During AD, tau is thought to undergo a dramatic shift in role. In contrast to basal conditions, disease-associated forms of tau are highly phosphorylated (2-3x more phosphate per mole protein) [54]. These hyperphosphorylated forms of tau can be induced in transgenic tau models by incorporation of a mutant tau variant (p301L) initially identified in Frontotemporal Dementia with Parkinsonism linked to chromosome 17 [60]. This mutation promotes the hyperphosphorylation and aggregation of tau in a manner similar to that observed during AD [61]. Incorporation of this mutation is widely used to study tauopathy, as overexpression of the wild-type human tau transgene does not result in overt tau pathology [62]. Evidence from p301L tau models suggest that tau phosphorylation is carried out by several kinases, including Glycogen Synthase Kinase 3 (GSK-3), Cyclin-dependant kinase 5 (CDK-5), Casein Kinase 1 (CK-1) and Protein

Kinase A (PKA) [63-67]. These kinase activities are presumed to be driven in part by upstream activation from Aβ. Experimental mouse models have demonstrated enhanced neurofibrillary tangle pathology in P301L tau mice crossed with Aβ-expressing mice or injected with exogenous Aβ [68, 69]. Hyperphosphorylated forms of tau have weaker binding affinity for microtubules, causing them to dissociate and increase the cytosolic concentration of free tau [70]. This free, hyperphosphoryated tau has a more compact, folded conformation and a propensity to aggregate [71]. The abnormal forms of tau also undergo a redistribution throughout the neuron, invading the somatodendritic compartment [54]. These disease-associated forms of tau are also resistant to proteosomal breakdown or autophagy, preventing clearance from neurons [72-74]. However, there is uncertainty over which form(s) of tau may be the most disease-relevant. Tau exists as a spectrum in neurons during AD, in various conformations, cell compartments, phosphorylation states and sizes (monomer, oligomer and insoluble aggregate). These abnormal forms of tau are hypothesized to take on new roles and mediate toxicity potentially through a gain-of-function mechanism [59].

Conversion of tau from a primarily microtubule-bound form in the axon to a hyperphosphorylated form distributed throughout the neuron is hypothesized to have several negative consequences to neuronal networks. A recently uncovered dimension to this issue concerns the ability of tau pathology to be transmitted through axons and spread between neurons in a prion-like manner [75]. This idea comports with evidence from human brain samples, in which a characteristic pattern of tau pathology progression is evident across the disease, classified by Braak stage [76]. Tau pathology is first observed in

the locus coeruleus and several additional subcortical nuclei (Subcortical pretangle stages a-c), and may represent a unique pre-AD pathology. At later stages, pathology becomes apparent in the transentorhinal region (Stage I), Entorhinal Cortex (stage II) then spreads to the hippocampal formation (Stage III) and later throughout the neocortex (Stages IV-V-VI) [76]. Increasing Braak Stage correlates with likelihood of dementia, with >90% of patients classified as stage V-VI manifesting with either moderate or severe dementia [77]. Pathological spread of tau can be modeled *in vivo* using tau transgenic mice, and amplified by injections of either Aβ or misfolded tau seeds [78-81]. Early experimental evidence with these models have linked spreading tau pathology to disruption of functional connectivity, compromised cognitive performance and loss of neurons in affected circuits [80, 82, 83].

Negative consequences of abnormal tau may also include deficits to normal axonal transport, which is critical for axonal survival. Deficits in this process are common to a wide variety of neurodegenerative diseases, including AD [84, 85]. Evidence for the importance of axonal transport was seen in loss of function mutations to molecular motor proteins, which move axonal cargos along microtubule networks. These mutations to kinesin or dynein impair fast axonal transport and can cause a characteristic 'dying-back' pattern of axonal degeneration [18, 86, 87]. Deficits to transport in AD have also been linked to the appearance of abnormal axons observed in post-mortem tissue. These axons are distinguished by focal swellings with internal accumulations of axonal cargos, transport proteins and organelles as well as phospho-tau and other microtubule-associated proteins [88-90]. Similar pathological changes are observed in AD mouse models that over-

express Aβ and tau [12, 13]. Experiments with tau mouse models have revealed that a common phenotype is reduction of axonal transport velocity [91-93]. These studies, often accomplished using Manganese Enhanced MRI (MEMRI) have demonstrated that these alterations to transport are coincident with the onset of phospho-tau pathology [94]. Intriguingly, these alterations in transport also support a role for Aβ. Using a cell culture model, Vossel et. al. have demonstrated that reductions in axonal transport can also be rapidly induced using Aβ, but blocked by tau ablation [95, 96]. Experimental evidence for several possible mechanisms has emerged. These alterations may stem from phospho-tau binding to kinesin adapter protein JIP1 and interfering with its function in axonal cargo loading [97]. Several recent studies also support a pathway involving hyperphosphoylated tau filaments inhibiting transport via activation of protein phosphatase 1 (PP1) and GSK-3. Active GSK-3 can phosphorylate kinesin light chain subunits, promoting the release of cargo from molecular motors [88, 96, 98]. Long term suppression of transport via these mechanisms is hypothesized to starve presynaptic terminals and distal sites within axons of vital proteins, nutrients and mitochondria necessary for maintenance, and lead to dying-back of the axon [99]. This process my account for the observed pattern of synapse and axon loss preceding overt cell loss during AD.

In addition to gain-of-function mechanisms, tau may also initiate axonal dysfunction through parallel loss-of-function mechanisms. Due to disassociation from microtubules and mislocalization in the somatodendritic compartment, it has been suggested that tau's native role in the axon may go unfilled. This may include actions as a microtubule stabilizer under basal conditions. This idea has been bolstered by evidence of

abnormal microtubule dynamics in neurons in AD and AD mouse models. Several studies have found shorter and less numerous microtubules in AD brain tissue and reductions in microtubule density among tau transgenic mouse models [100-102]. A study using deuterium labeling of amino acids revealed that two AD tau mice lines had 'hyperdynamic microtubles', with much larger shares of newly synthesized tubulin incorporated into axonal microtubules, relative to controls [103]. This suggests that axonal microtubules are less stable in the presence of pathogenic tau. Evidence from these studies have been challenged by the relatively mild phenotype of tau knockout mice, though these deficits may be compensated for by increases in other microtubule-binding proteins such as MAP1A [104, 105]. Several studies have explored the use of microtubule stabilizing drugs to correct potential deficits in microtubule stability. This strategy was first tested in tau transgenic mice using Paclitaxel, though its use is limited by blood-brain permeability [106]. More recent studies have utilized a derivative compound, Epothilone D, which shows permeability through the blood brain barrier and retention in the CNS [107]. These early studies have shown evidence that microtubule-stabilizing drugs correct deficits in learning/memory, axonal transport, microtubule density and dendritic spine loss in tau models [101, 106, 108, 109]. The in vivo studies have shown that long term treatment (3 months) using these drugs was sufficient to reverse deficits when administered before or after existing tau pathology. Surprisingly, these studies also showed evidence that these compound may reduce the accumulation of tau pathology, through unclear mechanisms. While several of these studies show beneficial effects of EpoD treatment, it remains ambiguous what mechanism(s) and site of action account for

its impact. Additionally, it is unclear whether its effect on reducing tau pathology is relevant to its effects on neurodegeneration.

In contrast to axon-specific mechanisms, axon loss may follow directly from synapse elimination and/or cell death driven by hyperphosphorylated tau acting at the post-synapse. Indeed, synapse loss and NFTs are the best correlates to cognitive impairment during AD. From post mortem synaptoneurosomal fractions, hyperphosphorylated forms of tau have been found at both pre and post synaptic terminals in AD but not control patients [110]. Simulation of these conditions has been explored using cultured hippocampal neurons, which develop somatodendritic tau inclusions after treatment with Aβ. This increase in mislocalized tau was associated with reductions in dendritic spines, local increases in Ca^{2+} and loss of microtubules [111]. Additionally, Ittner et. al. have shown data linking somatodendritic-tau to the targeting of Src kinase Fyn to the post-synapse [112]. This interaction leads to Fyn-mediated phosphorylation of the NMDA receptor, and stabilization of the Fyn/PSD-95 interaction, which promotes Aβ-driven excitotoxicity. These pathways may independently or synergistically work to promote postsynapse loss and/or neuronal loss during disease. It is unknown if these mechanisms play a role in triggering axon die-back during AD, though several examples from developmental biology suggest a close connection between synapse elimination and axon pruning [113].

Understanding how axon tract damage is related to human clinical data requires a model that can be analyzed using translational (noninvasive) biomarkers. Several mouse models of AD have been examined using DTI to discern if they can serve as reliable

models in this regard. To date, these studies have utilized APP-overexpressing strains, tau overexpressing strains and mixed APP/tau strains. Among APP-expressing lines, data have been mixed. Studies by Song and Sun et. al. found broad reductions in AxD, FA and increases in RAD in several white matter tracts in aged APP mice (12-18month APPsw and PDAPPs) compared with age-matched controls [2, 71]. However, two studies using another APP over-expressing strain (12-14 month and 16-18 month APP/PS1s) by Shu et. al. and Wiesmann et. al. found strikingly different patterns of white matter alterations by DTI. Shu et. al. reported increases in AxD, FA and reductions in RAD in white matter, while Wiesmann found no major differences within white matter tracts between transgenic mice and controls [114, 115]. Among transgenic lines carrying P301L mutant tau, two experiments have independently shown evidence of reduced FA within the corpus callosum of aged (8-8.5 month) rTg4510 mice, compared with age-matched WTs [116, 117]. DTI alterations have also been explored in triple-transgenic mice (3xTg), overexpressing APP and P301L tau. Surprisingly, in a study by Kastyak-Ibrahim et. al. no differences were found in any DTI metric (FA, AxD, TR or RAD) in white matter regions assessed (Fornix, Corpus Callosum, External Capsule) between aged 3xTg mice (11-17 months) and age-matched WTs [118]. Another transgenic model exhibiting amyloid and tau pathology (*APPSwDI*$^{+/+}$*ImNos2*$^{-/-}$) was reported to show reductions in FA and AxD, with increases in RAD in white matter pathways linked to hippocampal structures [119]. From these available studies, pure tauopathy models have shown the most reliable changes in DTI metrics, although it is unclear why such large degrees of variability exist between models. Several of these mouse studies have shown general associations between the

onset of brain pathology (Aβ or tau) and onset of DTI alterations in vulnerable white matter regions [2, 71, 116, 119, 120]. However, from these studies it remains ambiguous how brain pathology is contributing to the observed DTI changes. In principle, these changes may stem from direct perturbation of water diffusion or by directly or indirectly precipitating loss of structural elements in white matter (axons, microtubules, myelin sheaths, etc). A more structured analysis is required to discern causality, in order to link defined, localized pathologies with subsequent alterations in DTI properties and measures of neurodegeneration (loss of axons, cells).

The visual system may serve as a tractable model to unravel the complex underlying relationships between AD pathology, neurodegeneration and noninvasive biomarkers. This system, composed of the Optic nerve (ON) and Optic Tract (OT) have several unique anatomical advantages for studying neurodegeneration *in vivo*. Composed of Retinal Ganglion cells (RGC) axons, the ON and OT form a homogeneous fiber bundle uninterrupted by interneurons spanning ~5mm in the mouse. Its length allows visualization of separate axonal subdomains proximal (ON) and distal (OT) to the cell body. The tract is partially separate from the brain (in the ON) and is relatively large diameter (~225μm), makes identification, segmentation and DTI measurements straightforward. The ON and OT are also amenable to quantitative histology, allowing for counts of individual axons and myelin sheaths. Additionally, the somatodendritic compartment of RGCs exist in the most superficial layers of the retina (Retinal Nerve Fiber Layer, RNFL / Ganglion Cell Layer, GCL and Inner Plexiform Layer, IPL), permitting direct visualization through Optical Coherence Tomography (OCT). This

optical technique allows depth imaging of retinal layers, with resolution down to ~2μm, which can discern small changes in cell layer thickness [121]. Neurodegenerative diseases with prominent ON damage (as in Glaucoma and Multiple Sclerosis) show reductions in these layers' thickness, presumed to reflect RGC atrophy and loss [122, 123]. Several studies have also found reductions in these layers' thickness among AD patients [124-126]. The unique ability to simultaneously visualize axon and cell body compartments in the visual system may help disentangle the phenomena of axonal degeneration from cell body loss. This distinction is critical for understanding whether mechanisms governing neurodegeneration operate at the cell body or axon level. This tract has been used as a testbed to simulate various controlled modes of axonal degeneration. This includes as a model to experimentally induce Wallerian Degeneration (as in retinal ischemia models) and dying-back degeneration (in Experimental Autoimmune Encephalomyelitis, EAE) [27, 127, 128]. This flexibility allows patterns of biomarkers, including DTI and OCT measures to be linked back to definitive axonal pathologies.

Work is yet required to understand the full scope of pathological changes that accompany and precipitate axonal degeneration during AD. A more full understanding of how imaging biomarkers relate to changes at a cellular level will help bridge the divide between clinical datasets and basic science.

Chapter I:

Diffusion Tensor Imaging Reveals Visual Pathway Damage in Patients with Mild Cognitive Impairment and Alzheimer's Disease.

Abstract

Visual deficits are commonly seen in patients with Alzheimer's disease (AD), but postmortem histology has not found substantial damage in visual cortex regions, leading to the hypothesis that the visual pathway, from eye to the brain, may be damaged in AD. Diffusion tensor imaging (DTI) has been used to characterize white matter abnormalities. However, there is a lack of data examining the optic nerves and tracts in patients with AD. In this study, we used DTI to analyze the visual pathway in healthy controls, patients with mild cognitive impairment (MCI) and AD using scans provided by the Alzheimer's Disease Neuroimaging Initiative (ADNI). We found significant increases in the total diffusivity (TR) and radial diffusivity (RAD) and reductions in fractional anisotropy (FA) in optic nerves among AD patients. Similar but less extensive changes in these metrics were seen in MCI patients as compared to controls. The differences in DTI metrics between groups mirrored changes in the splenium of the corpus callosum, which has commonly been shown to exhibit white matter damage during AD and MCI. Our findings indicate that white matter damage extends to the visual system, and may help explain the visual deficits experienced by AD patients.

Introduction

Alzheimer's Disease (AD) is a progressive neurodegenerative disease characterized clinically by memory loss and cognitive impairment and pathologically by amyloid plaques, neurofibrillary tangles and brain volume shrinkage [129]. In vivo neuroimaging using Positron emission tomography (PET) and Magnetic Resonance Imaging (MRI) are able to reveal amyloid plaques and brain atrophy, which both occur mostly within gray matter regions of AD patients [130]. In white matter though, abnormal MRI signals have been found in patients with AD [28, 131, 132] as well as patients with mild cognitive impairment (MCI) [133-135]. Evidence now indicates that white matter damage coincides with early pathophysiological events in gray matter. This damage may play a critical role in the neurofunctional declines seen in patients with AD.

Among white matter tracts in the brain, the visual pathway is unique in structure. Neurons that compose the optic nerve and tract have their cell bodies (retinal ganglion cells, RGCs) outside the brain within the retina [136]. Despite the relatively isolated RGC location, the visual system like other sensory systems, declines during AD [137]. Many AD patients suffer from complex visual disturbances and have worse color vision and contrast sensitivity when compared to similarly aged controls [138]. Additionally, the severity of these visual deficits is associated with lower clinical dementia rating [137]. Despite impaired visual ability, the visual cortex is relatively protected from atrophy and disease pathology in AD [137, 139-141], leading to the hypothesis that the visual pathway, from eye to the brain, may be damaged in AD.

While abnormal white matter has been found in various brain regions in AD, there is a lack of imaging data for the visual pathway. Direct evaluation of the visual pathway white matter can be accomplished through the use of diffusion tensor imaging (DTI) [21, 25, 142]. This novel MRI modality measures the diffusion of water molecules and is sensitive to microstructural changes in live tissue. When applied to the brain, DTI shows white matter as areas with high diffusion anisotropy, due to the organized parallel fiber bundles, in contrast to low anisotropy within the gray matter and ventricles. Disruptions in white matter structure usually lead to a reduction in diffusion anisotropy, as quantified by Fractional Anisotropy (FA) and Relative Anisotropy (RA) [21, 25, 142]. In addition, DTI-derived axial diffusivity (AxD) and radial diffusivity (RAD) quantify water diffusion parallel and perpendicular to fiber tracts, respectively. Specific white matter pathologies, such as demyelination and axonal degeneration, have been shown to change RAD and AxD, respectively [25-27, 143-145].

DTI studies have previously demonstrated that white matter damage occurs in distinct regions during AD and MCI [28, 133, 146]. However, to the best of our knowledge, there is no published study using DTI to examine the visual pathway in AD. In this study we worked on image data provided by the Alzheimer's Disease Neuroimaging Initiative (ADNI). DTI parameters were measured in the optic nerves and tracts of ADNI participants. We also measured DTI changes within the splenium of the corpus callosum, in order to reference our findings against a site commonly seen to exhibit white matter damage during MCI and AD [28, 147]. The findings of this study are of potential relevance to early

diagnostic criteria and to gain a greater understanding of the underlying visual problems in AD.

Methods

Data used in the preparation of this article were obtained from the Alzheimer's Disease Neuroimaging Initiative (ADNI) database (adni.loni.usc.edu). The ADNI was launched in 2003 by the National Institute on Aging (NIA), the National Institute of Biomedical Imaging and Bioengineering (NIBIB), the Food and Drug Administration (FDA), private pharmaceutical companies and non-profit organizations, as a $60 million, 5-year public-private partnership. The primary goal of ADNI has been to test whether serial magnetic resonance imaging (MRI), positron emission tomography (PET), other biological markers, and clinical and neuropsychological assessment can be combined to measure the progression of mild cognitive impairment (MCI) and early Alzheimer's disease (AD). Determination of sensitive and specific markers of very early AD progression is intended to aid researchers and clinicians to develop new treatments and monitor their effectiveness, as well as lessen the time and cost of clinical trials.

The Principal Investigator of this initiative is Michael W. Weiner, MD, VA Medical Center and University of California–San Francisco. ADNI is the result of efforts of many co-investigators from a broad range of academic institutions and private corporations, and subjects have been recruited from over 50 sites across the U.S. and Canada. The initial goal of ADNI was to recruit 800 subjects but ADNI has been followed by ADNI-GO and

ADNI-2. To date these three protocols have recruited over 1500 adults, ages 55 to 90, to participate in the research, consisting of cognitively normal older individuals, people with early or late MCI, and people with early AD. The follow up duration of each group is specified in the protocols for ADNI-1,ADNI-2 and ADNI-GO. Subjects originally recruited for ADNI-1 and ADNI-GO had the option to be followed in ADNI-2. For up-to-date information, see www.adni-info.org.

Thirty subjects were selected in each cohort made of healthy control, MCI and AD-classified patients. Within each cohort, subjects were evenly split by gender and were selected based upon similar characteristics between groups (Table 1.3). Subjects were excluded from selection if they had been diagnosed with any variant of glaucoma, macular degeneration, or complained of blurry vision. Thirty patients per group maximized the use of the ADNI DTI data, while maintaining neutral gender balance. Selection of greater numbers would have necessarily resulted in skewed male/female ratio. Each patient underwent MRI scans on a 3-Tesla GE Medical Systems scanner. For our analysis, we used two sets of scans collected, an anatomical T1-weighted spoiled gradient echo (256x256 matrix; 1.2 x 1 x 1mm^3 voxel size; TI=400ms; TR=6.984ms; TE= 2.848ms; flip angle= 11^0) along with a DTI scan. The DTI includes a group of diffusion-weighted images (256x256 matrix; 1.367x1.367x2.7 mm^3 voxel size; 35 mm field of view) comprised of 5 B0 images and 41 diffusion-sensitized images (B=1000 s/mm^2).

Image Processing

MRI scans were downloaded from the ADNI database. Diffusion-weighted scans were processed within DTIPrep to eliminate artifacts from head motion, eddy currents, and gradient distortions [148]. Processed diffusion-weighted images passing DTIPrep quality control were then loaded into 3D slicer (www.slicer.org). The B0 images from the diffusion-weighted scan were registered to a stationary T1 scan for anatomical reference. The registration protocol utilized the Brainsfit Module and relied upon rigid, affline and Bspline transforms. A deformation field from these transforms was then used to register DTI maps. All images were carefully checked to ensure tight correspondence between the T1 and the resulting DTI. Maps for five DTI indices, including fractional anisotropy (FA), trace diffusion (TR), axial (AxD), radial (RAD) diffusivity and eigen3 ($\lambda 3$) were generated using 3D slicer [21, 144].

Analysis Methods

Regions of interest were selected from optic nerves (Figure 1.3), optic tracts (Figure 1.4 and 1.5), and the splenium of corpus callosum (Figure 1.6). The optic nerve approximately 3 mm rostral to the optic chiasm was identified and selected manually using the T1 reference scan in conjunction with the FA and Minimum Eigen ($\lambda 3$**)** map (Figures 1.3 and 1.5). This section could be precisely identified in each subject by following the optic chiasm (caudal to rostral) until it split into two optic nerves (Figure 1.3). The optic nerve ROI was selected in the first section showing two separate optic nerves, rostral to the optic chaism. To minimize partial volume effects, ROIs were

selected in one coronal slice which showed the transected optic nerve clearly as two round regions (Figure 1.3). Using a similar method, the optic tract approximately 14 mm caudal to the optic chiasm was identified as two round areas in coronal section and selected using the T1 scan in combination with the registered FA map (Figures 1.4 and 1.5). These ROIs were chosen based upon their ability to be selected easily and unambiguously. All ROIs for each section are included in the supplemental figures. The splenium was selected using the DTI within 5 mid-sagittal sections and identified using morphology as the most caudal, enlarged portion of the corpus callosum (Figure 1.6). Any scan showing distortion of the optic nerve or tract around the ROI was excluded from analysis. Among the 89 subjects, six optic nerves were excluded from analysis (2 control, 2 MCI, 2 AD), and one optic tract (AD). No corpus callosum scans were excluded.

Statistical Analysis

Group comparisons of personal characteristics (age, education, body mass index) and neuropsychological data (MMSE scores) were made by non-parametric Kruskal-Wallis analysis of variance (ANOVA), with post-hoc Mann-Whitney U test. Within each group, collected DTI data was tested for normality using the D'Agostino-Pearson omnibus normality test. The test did not show any significant deviations from normality within the groups. Comparisons of DTI measures (TR, FA, RAD, AxD) within each ROI were made using a one-way ANOVA followed by Tukey's post-hoc test to examine differences

between the three patient groups. For each analysis, $p<0.05$ was considered significant. Statistics were performed using Prism Graphpad (San Diego, CA).

Results

The MCI, AD and control groups did not significantly differ in terms of their age, gender bias, years of education or body mass index (BMI). They did significantly differ in terms of their MMSE score, reflecting reduced cognitive ability of the MCI and AD groups compared with controls, as well as a significant difference between MCI and AD patients (Table 1.1).

DTI in Optic Nerves

Analysis of sections from the optic nerves of AD, MCI and control patients revealed key differences in several DTI indices. The AD and MCI patient cohorts showed significant ($p<0.05$) increases in TR and RAD when compared with the control group. The AD group mean TR value was 24.4% higher, while MCI patients' rose 16.6%. Relative to controls, AD cohort RAD increased by 29.5%, while it rose by 19% among the MCI cohort. FA values among cognitively impaired patients were significantly reduced, 11.6% among MCI patients and 18.6% in the AD cohort. Measures of AxD increased among MCI (8.6%) and AD (13.9%) patients relative to controls, but only met statistical significance in the AD patient group.

DTI in Optic Tracts

Within the optic tract, DTI changes among AD and MCI patients (relative to controls) followed similar patterns to that of the optic nerve. MCI and AD patient cohorts showed consistent reductions in FA, and increases in TR, AxD and RAD. Among AD patients, mean TR, AxD and RAD were increased by 12.3%, 6.9% and 18.9% respectively. Mean FA was reduced by 8.2%, relative to controls. MCI patient group differences followed similar trends, with increases in TR (5.9%) and RAD (11.6%). Mean FA among MCI patients was reduced by 6.1%. These changes between groups, while trending in similar directions as the AD group, did not meet statistical significance either via ANOVA, or with use of Tukey's post-hoc tests.

DTI in Corpus Callosum

The splenium of the corpus callosum exhibited DTI changes consistent with what was seen in the visual white matter tracts. The splenium in our MCI and AD patient cohorts had significant changes in FA, TR and RAD values vs. controls. Mean FA was reduced in these cohorts by 5.2% in MCI patients ($p<0.01$) and 5.2% in AD patients ($p<0.001$). TR increased among MCI (5.8%, $p<0.05$) and AD (8.7%, $p<0.01$) patients as well as measures of RAD, which increased by 20.6% in MCI ($p<0.01$) and 26.5% ($p<0.001$) in AD cohorts. The AxD measure marginally increased in AD (1.7% increase) and MCI (0.6%) without any significant change.

Discussion

Our study demonstrates that the visual pathway from eye to the brain is affected during the degeneration process in AD and MCI. Increases in TR, RAD and reductions in FA were found within optic nerves among the AD and MCI cohort compared to a similarly aged, gender-balanced control group. Similar, but less extensive changes were also seen in the optic tract. These diffusional differences in the visual pathway mirror those in the splenium of the corpus callosum, which has been shown in previous studies to be affected during MCI and AD [28]. To the best of our knowledge, this is the first study to show DTI-detected visual pathway injury in AD and MCI patients. Our findings raise the possibility that damage within the visual white matter tracts may be responsible for visual deficits experienced by AD patients.

Results from several studies have shown Alzheimer's patients perform poorly on low-level measures of visual ability. These deficits have been demonstrated in tests of stereo acuity, color discrimination, contrast sensitivity, visual processing speed and visual field coverage [138, 149]. AD patients also have a significantly slower pupillary light reflex as compared to controls [150]. Evidence from these studies showed clearly that visual problems are widespread among AD patients and in some cases, correlate with the severity of dementia [151].

Atrophy or dysfunction within the primary visual cortex, while apparent in a small (~5%) subset of patients [152], may not fully account for the general visual problems experienced

by AD patients. Evidence from in vivo imaging and post-mortem studies largely suggest that the visual cortex is not heavily impacted during AD or MCI. MRI studies measuring cortical thinning show relative sparing of the visual cortex grey matter from atrophy during MCI and early onset AD [139, 140]. Additionally, primary visual cortex glucose metabolism activity is relatively preserved in AD subjects (in contrast to adjacent cortical areas) as measured by [^{18}F] flurodeoxyglucose PET [153]. These data correspond well with autopsy studies showing the visual cortex to be relatively spared by neurofibrillary tangles and Aβ plaque pathology [137, 141]. Visual deficits among AD patients are not easily explained by visual cortex dysfunction, which may hint at other mechanisms that contribute to the general visual problems that occur during AD.

Several pieces of evidence from histology studies, as well as recent *in vivo* imaging data using optical coherence tomography (OCT) may help account for visual deficits in AD. Studies examining retinas from post-mortem samples have found that RGC loss occurs during the course of AD, and may be a feature of MCI. A study by Blanks, et. al. found a 25% total reduction among neurons in the ganglion cell layer in AD, compared to controls [154]. An additional histological study by Hinton et. al found similar reductions in RGCs among AD patient retinas [155]. The use of OCT has made non-invasive measures of the ganglion cell layer in the retina possible [156]. Several studies have utilized this technique to quantify the retinal ganglion nerve fiber layer (RNFL) thickness in patients with AD and MCI. Studies by Parisi et. al. and Paquet et. al. have used this technique and independently shown reductions in RNFL thickness among AD patients as compared to

similarly aged controls [126, 157]. Interestingly, data from Paquet et al demonstrated cognitive decline-dependent reductions in RNFL thickness, with MCI, AD and severe AD all showing progressively greater degrees of thinning [126]. These lines of evidence demonstrate that cell bodies of optic nerves are lost during AD and MCI, and imply that the degree of loss may correspond to disease severity. Furthermore, loss of cell bodies may be concomitant with a loss of axons and associated myelin sheaths within the white matter of the optic nerve and tract.

Use of DTI allows for interrogation of microstructural change within the white matter. DTI metrics (TR, FA, AxD, RAD) are each sensitive to different features of white matter pathology, making them ideal to study degeneration within the white matter [25-27, 143-145]. Studies using DTI in conjunction with histology have validated these associations by using preclinical mouse models of myelin damage [27, 143, 145]. Specifically, cuperizone-induced myelin loss led to reduced diffusion anisotropy and increases in RAD and TR [145]. Our previously used animal models of AD show that reduced diffusion anisotropy and increased RAD appear during white matter degeneration, complete with axonal loss and evidence of demyelination [144]. An additional study using a rat model of glaucoma showed similar diffusion changes in the optic nerve in response to induced RGC loss [158]. Research using human post-mortem brains found similar relationships between histological determinations of myelin content, axon counts and reductions in FA as well as increases in TR. These results indicate that reduced FA and increased TR are associated with reductions in myelin and axon numbers [159]. Although it is difficult to

speculate on the potential condition of the optic nerves and tracts in our subject pool of MCI and AD patients, collective evidence supports the possibility that our DTI results reflect gradual axonal loss and myelin disruption in the visual pathway among our MCI and AD patients.

Accumulating evidence suggests that the cognitive decline that defines MCI may stem from the development of early AD pathology [160]. Recognizing the clinical presentation and understanding the pathophysiological changes during the pre-dementia stage is critical to develop a therapeutic strategy for AD. The formal classification of MCI has been recently clarified to define a pre-dementia stage distinct from normal aging, when patients suffer a decline in memory and cognitive faculties [23]. Relative to healthy controls, MCI patients may present significantly lower levels of CSF Aβ and higher levels of PET amyloid-tracer uptake and binding, reflecting higher levels of accumulation within the brain - a classic hallmark of AD [130]. MCI cohorts also have significant changes in other biomarkers that are associated with AD including CSF Tau/phopho-tau levels [130, 160]. All these pieces of evidence support the idea that MCI represents an intermediate state between AD and healthy aging. In addition to the changes in Aβ and Tau, white matter disruptions may also be present. We saw evidence for this in our study, with increases in TR and RAD, and decreases in FA in the optic nerve and splenium of the corpus callosum among the MCI patients. Our findings are in agreement with previously reported studies suggesting white matter disruptions occur during this prodromal stage of AD [133-135]. White matter is composed of axonal bundles and embeds the connectomic

features of each individual. Disruption of these connections directly affects neural networks, which may play an important role in causing the clinical presentations of MCI, seen in memory decline and cognitive impairment [161].

Many previous studies have leveraged DTI to identify sites of white matter damage in the brains of AD and MCI patients [133-135], but these studies have largely ignored white matter within the visual pathway. While this pathway makes up a large section of white matter, it lies partially below the brain and is vulnerable to automatic exclusion by MRI pre-processing tools, such as skull-stripping algorithms. The optic nerves are also quite narrow, and their positions vary largely among individuals (see supplemental data) making it challenging for voxel-based morphometry approaches to identify it. We also attempted to apply fiber tracking algorithms to identify the whole extent of the visual pathway, but never obtained satisfactory results. This is due in part to the extremely narrow dimensions of the nerves, high angular turning of the fibers in some individuals, crossing fibers in chiasm, and adjacency to various white matter tracts.

Our ROI approach yields reliable and accurate measurements of DTI in optic nerves and tracts. The disadvantage was being more labor intensive and not measuring the whole extent of the optic nerves and tracts. Despite its small size, the optic chiasm has a unique "X" structure and can be easily identified on an axial brain image, which provides a reliable landmark to guide the selection of optic nerves and tracts (Figure 1.5). To assure correct selections of these regions, we always reviewed 10-12 contiguous coronal slices

anterior and posterior to the chiasm. The left and right optic nerves would merge in the chiasm, then split into left and right optic tracts.

One caveat to this study is the influence of partial volume effects, which reduce the sensitivity of our measurements in characterizing injured nerves. Instead of selecting the ROI on the axial/sagittal views of these nerves, we selected the ROI in the coronal view to minimize the partial volume effect. Optic nerves and tracts are thin. Even with careful ROI selection, partial volume effects could not be completed avoided. For future study, we recommend DTI scans with increased spatial resolution. We believe the trend would be the same but should provide a better sensitivity to characterize abnormality of the visual pathways in AD.

While the ADNI database does contain many more subjects than we analyzed, only a subset of those underwent DTI. Within the datasets we have explored, there were 1,879 subjects recruited in the ADNI database, among which, 49 AD, 133 MCI and 66 controls had DTI scans. Patients with blurry vision or glaucoma were excluded to avoid the confounding factors to our analysis. We are using the maximum number of subjects available, without a gender imbalance between groups.

In conclusion, white matter damage in AD as detected by DTI extends to the optic pathway. Significant DTI changes including increases in TR and RAD, and decreases in FA occur early in MCI cohorts. These changes also occur in AD cohorts, compared to

similarly aged, gender-matched controls. This finding may help contextualize OCT data from several studies showing reductions in RGCs among AD patients [124, 126] and clinical data demonstrating AD-associated visual deficits [137, 138].

Acknowledgement

This study was partly supported by NIH R01NS062830.

Data collection and sharing for this project was funded by the Alzheimer's Disease Neuroimaging Initiative (ADNI) (National Institutes of Health Grant U01 AG024904) and DOD ADNI (Department of Defense award number W81XWH-12-2-0012). ADNI is funded by the National Institute on Aging, the National Institute of Biomedical Imaging and Bioengineering, and through generous contributions from the following: Alzheimer's Association; Alzheimer's Drug Discovery Foundation; BioClinica, Inc.; Biogen Idec Inc.; Bristol-Myers Squibb Company; Eisai Inc.; Elan Pharmaceuticals, Inc.; Eli Lilly and Company; F. Hoffmann-La Roche Ltd and its affiliated company Genentech, Inc.; GE Healthcare; Innogenetics, N.V.; IXICO Ltd.; Janssen Alzheimer Immunotherapy Research & Development, LLC.; Johnson & Johnson Pharmaceutical Research & Development LLC.; Medpace, Inc.; Merck & Co., Inc.; Meso Scale Diagnostics, LLC.; NeuroRx Research; Novartis Pharmaceuticals Corporation; Pfizer Inc.; Piramal Imaging; Servier; Synarc Inc.; and Takeda Pharmaceutical Company. The Canadian Institutes of Health Research is providing funds to support ADNI clinical sites in Canada. Private sector contributions are facilitated by the Foundation for the National Institutes of Health (www.fnih.org). The grantee organization is the Northern California Institute for

Research and Education, and the study is coordinated by the Alzheimer's Disease Cooperative Study at the University of California, San Diego. ADNI data are disseminated by the Laboratory for Neuro Imaging at the University of Southern California.

Group Demographic Information

	Control	MCI	AD	*p* value
N	30	30	29	
Sex (M/F)	15 / 15	15 / 15	15 / 14	
Age (yrs)	70.9 (5.4)	71.1 (5.9)	72.1 (7.2)	0.727
Education (yrs)	16.7 (2.7)	15.8 (2.6)	16 (2.5)	0.328
Body Mass Index	28 (4.3)	28 (5.5)	25.9 (5)	0.184
Mini Mental State Exam	28.7 (1.5)	27.3 (1.9)	23.5 (1.7)	**<0.0001**
p value vs. Ctrl		**0.0016**	**<0.0001**	
p value vs. MCI			**<0.0001**	
Mean (SD)				

Table 1.1 Bold Numbers indicate significant p values ($p<0.05$)**.** Group comparisons made with a non-parametric Kruskal-Wallis analysis of variance (ANOVA), pair-wise comparisons made using post-hoc Mann-Whitney U test

DTI Measures from Control, MCI and AD Cohorts

	Control Mean (SD)	MCI Mean (SD)	AD Mean (SD)	One-way ANOVA *p value*
ON FA	0.43 (0.06)	0.38 (0.08)	0.35 (0.07)	**0.0005**
ON TR	4.09 (0.72)	4.77 (0.96)	5.09 (0.90)	**0.0001**
ON AxD	2.09 (0.33)	2.27 (0.36)	2.38 (0.36)	**0.0112**
ON RAD	1.05 (0.24)	1.25 (0.32)	1.36 (0.28)	**0.0004**
OT FA	0.49 (0.09)	0.46 (0.09)	0.45 (0.09)	0.0946
OT TR	4.07 (0.97)	4.31 (0.97)	4.57 (1.34)	0.2288
OT AxD	2.16 (0.41)	2.20 (0.36)	2.31 (0.53)	0.4169
OT RAD	0.95 (0.29)	1.06 (0.31)	1.13 (0.41)	0.1449
CC FA	0.77 (0.03)	0.73 (0.14)	0.73 (0.05)	**0.0001**
CC TR	2.42 (0.15)	2.56 (0.44)	2.63 (0.27)	**0.0065**
CC AxD	1.75 (0.10)	1.74 (0.28)	1.78 (0.12)	0.4128
CC RAD	0.34 (0.05)	0.41 (0.10)	0.43 (0.09)	**<0.0001**

Table 1.2 Abbreviations: ON = optic nerve; OT = optic tract; CC = splenium of the corpus callosum TR, AxD, RAD measures in units of 10^{-3} mm^2/sec. Bold numbers indicate significant p values

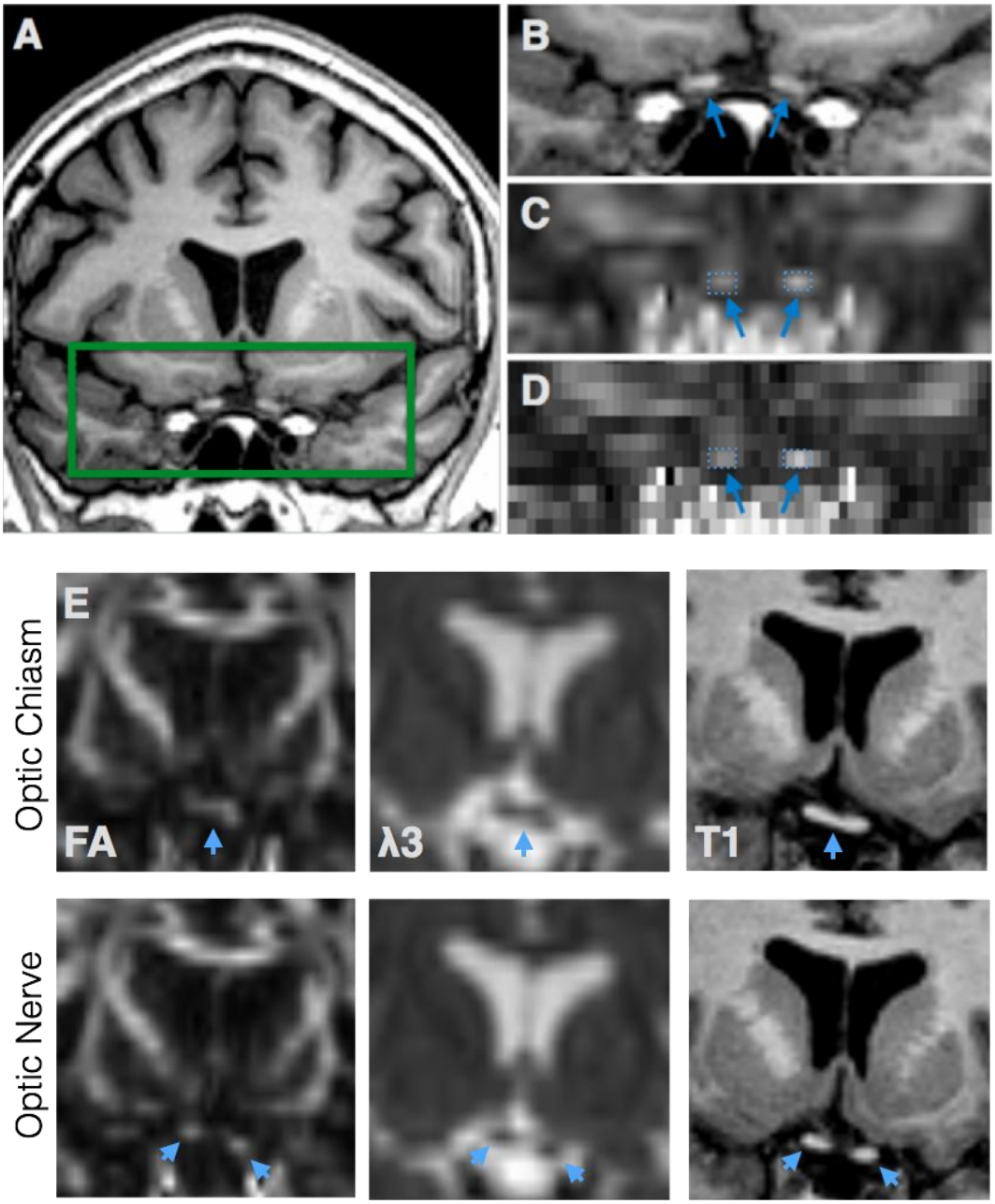

Figure 1.3 The Optic Nerve ROI A. T1 anatomical scan shows the region of the optic nerve ROI in coronal section. The rectangle was expanded (B) with corresponding FA map (with interpolation, C and without, D). Optic nerves identified with arrows, with selected ROIs (comprising 2-3 voxels on each side) outlined in blue. E. Upper row shows the optic chiasm (arrows) in FA, λ3 and T1 section before it splits into two optic nerves in the next slice (lower row)

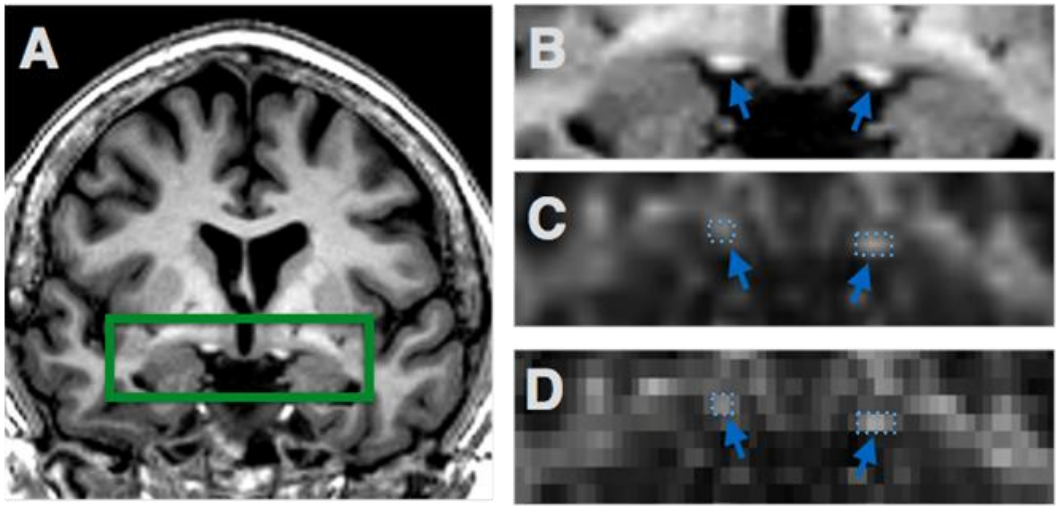

Figure 1.4. Optic Tract ROI A. T1 anatomical scan shows the region of the optic tract (A). The green rectangle was expanded in (B), with the registered FA map (C,D) where the optic tract is identified with arrows and selected ROIs outlined in blue.

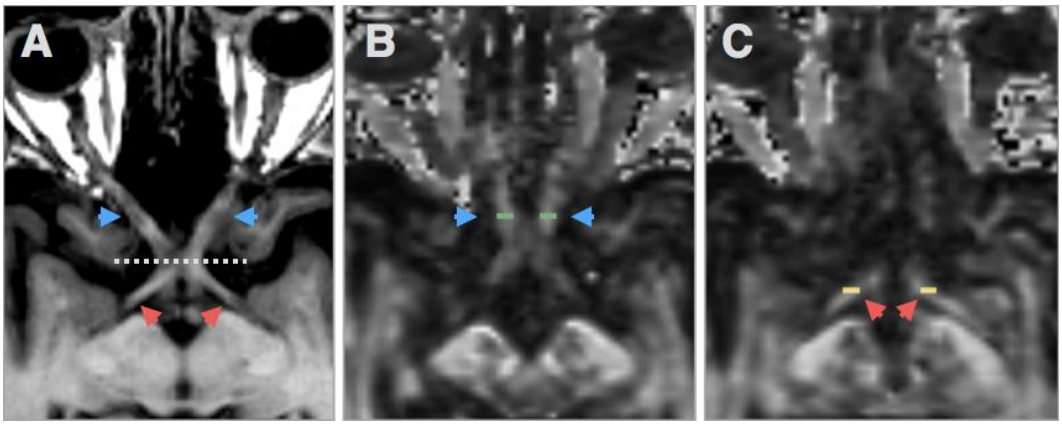

Figure 1.5 ON and OT ROIs in axial section A. Axial T1 section showing the optic nerve (blue arrows) and optic tract (red arrows) separated by the optic chiasm (dotted line). B. FA map showing the position of the optic nerve ROI (green rectangles) in axial section. C. Optic tract ROI shown on FA map in axial section.

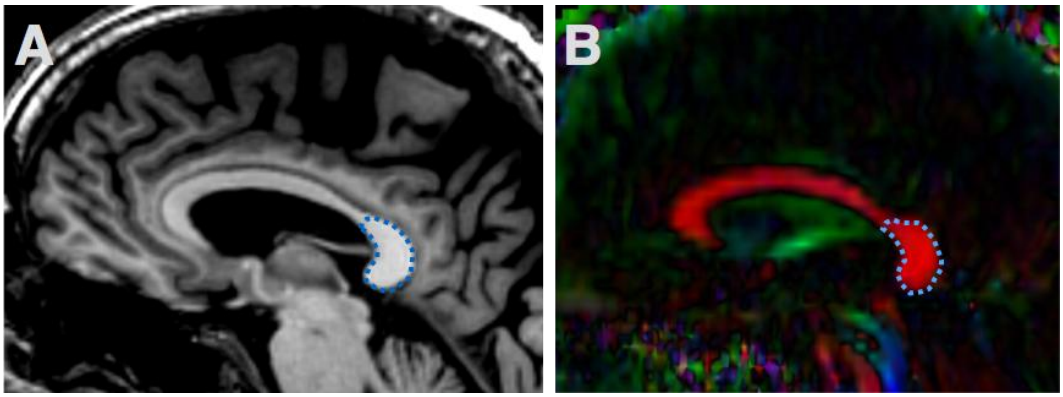

Figure 1.6 A. Splenium of the corpus callosum ROI. The corpus callosum is easily identified with a saggital T1 image (A) and DTI (B). The splenium ROI is outlined in blue.

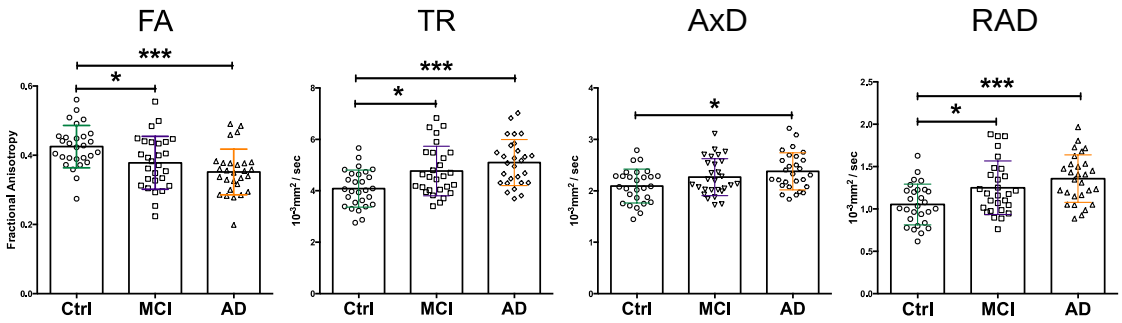

Figure 1.7. **Optic Nerve DTI Measures.** Optic nerves from AD and MCI patients show significant changes in FA, TR and RAD versus healthy controls. Data-points shown with overlapping mean ±SD. Statistical tests between groups performed with Tukey's post-hoc test after one-way ANOVA (*, $p<0.05$; ***, $p<0.0001$)

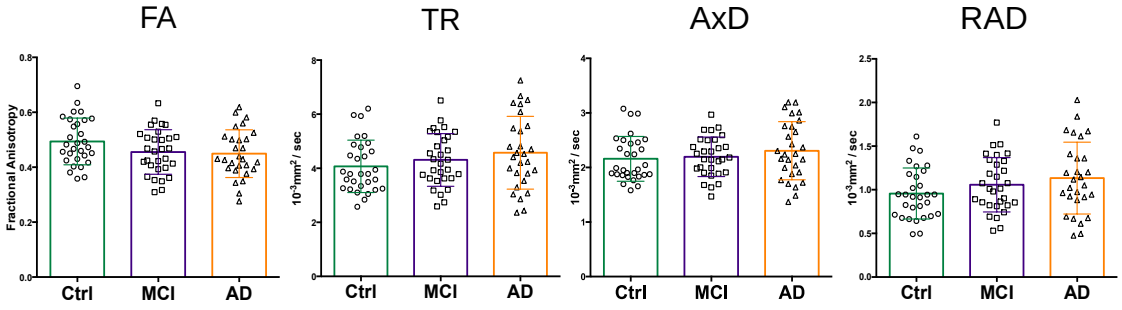

Figure 1.8. Optic Tract DTI Measures. Optic tract measures showed trends toward reductions in FA among AD patients, as well as increases in TR and RAD.

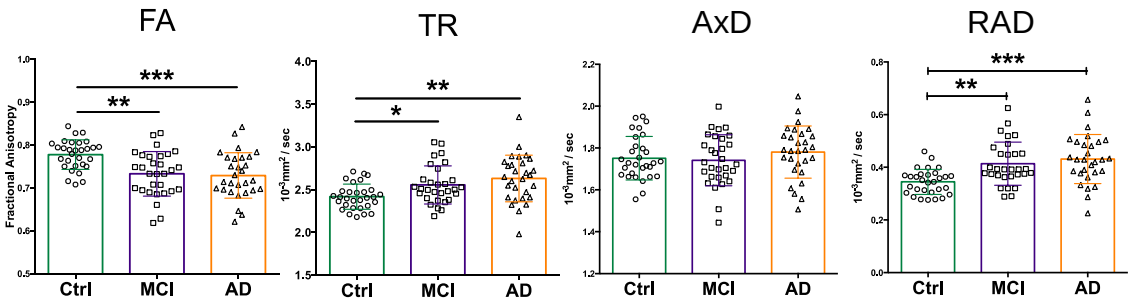

Figure 1.9 Splenium of the corpus callosum DTI Measures. DTI Measures of the splenium show significant differences in diffusional metrics between control, MCI and AD patients cohorts. Patients with AD and MCI have significant increases in TR and RAD, and significant reductions in FA vs. healthy controls. Statistical tests between groups performed with Tukey's post-hoc test after one- way ANOVA (*, $p<0.05$; **, $p<0.01$; *** $p<0.001$)

Chapter II:

Anterograde-propagation of axonal degeneration in the visual system of WldS mice characterized by DTI.

Abstract

Purpose: To evaluate the feasibility of using Diffusion Tensor Imaging (DTI) to characterize the temporospatial profile of axonal degeneration and its relation to blood-brain-barrier (BBB) permeability.

Materials and Methods: Longitudinal DTI was performed in Wallerian degeneration slow (WldS) mice following retinal ischemia. In parallel, Gadolinium (Gd)-enhanced T1-weighted imaging (Gd-T1WI) was performed to evaluate BBB permeability in white matter during axonal degeneration. To confirm the *in vivo* findings, immunohistochemistry using SMI-31 and MBP was performed to examine the axons and myelin, respectively, and Evans Blue was used to evaluate the permeability of the BBB.

Results: Reduced axial diffusivity was found in the optic nerve (ON, -15%, p=0.0063) one week and optic tact (OT, -18%, p=0.0077) two weeks after retinal ischemia, which were respectively associated with an 11% (p=0.0116) and 25% (p=0.0001) axonal loss. Increased radial diffusivity was found 1-2 weeks after the co-located decrease of axial diffusivity (35% increase, p = 0.0388 in the ON at week 2 and an 80% increase, p = 0.0015 in the OT at week 4). No significant changes were observed using Gd-T1WI (p = 0.13 - 0.75), although an approximately 1-fold increase in Evans blue staining intensity was found in the injured ON and OT starting one week after retinal ischemia.

Conclusions: We demonstrate the utility of DTI to characterize anterograde-propagating axonal degeneration through the ON and OT following retinal damage. Evans blue

staining revealed serum albumin accumulation at injured sites, though there was no BBB leakage detectable using Gd-T1WI.

Introduction

Axonal degeneration is a common feature of many neurological diseases [162, 163]. Damage to neuronal cell bodies or axons may trigger axonal degeneration, which can precipitate secondary degeneration along axons toward remote sites. Distinct patterns of degeneration exist and may depend upon the types of nerve fibers and initial causes of damage [164-166]. Use of non-invasive tools to characterize patterns of degeneration in disease may provide useful insights into disease course and pathogenesis.

Diffusion Tensor Imaging (DTI) is a clinically available imaging tool, which is sensitive to white matter disruption, including damage to axons [25, 167]. Although several studies have used DTI to characterize axonal degeneration [168-171], most studies were conducted in humans, with a lack of histological data to confirm the *in vivo* findings. Furthermore, no studies have systematically collected data from multiple locations along fiber tracts during degeneration, making it difficult to derive a spatial profile of axonal degeneration. It is therefore critical to utilize animal models, with histological follow-up, to evaluate the feasibility of using DTI to characterize the temporospatial profile of axonal degeneration.

Among neurological diseases, axonal degeneration in Multiple Sclerosis (MS) is especially critical, as it may lead to permanent disability of patients who initially were in the Relapsing-Remitting status [172]. In MS, gadolinium (Gd)-enhanced T1-Weighted Magnetic Resonance Imaging (Gd-T1WI) is routinely used to detect inflammation [173-175]. However, focal inflammatory damage in white matter may trigger axonal degeneration, which can spread degenerating lesions to remote sites in the brain [176-178]. It is not certain whether the BBB remains intact in regions remote from initial inflammation, considering that cellular debris removal and pro-inflammatory cytokine release may occur as a result of local axonal degeneration [179, 180]. Although studies support the idea that white matter with axonal degeneration does not show enhancement on Gd-T1WI [181, 182], data with supportive evidence are limited. It is therefore of interest to use an animal model to explore the changes in BBB permeability using Gd-T1WI in parallel with DTI during white matter axonal degeneration. The purpose of this study is to evaluate the feasibility of using DTI to characterize the temporospatial profile of axonal degeneration and to understand its relation to BBB permeability.

Materials and Methods

Animal groups and treatment methods

This study was conducted in accordance with National Institutes of Health guidelines and Statement for the Use of Animals in Ophthalmic and Visual Research, and was approved by the Institutional Animal Care and Use Committee.

Twenty-eight 8-week-old female Slow Wallerian Degeneration (WldS) mice were used. Transient retinal ischemia was performed on the right eye of each mouse. The detailed procedure was described previously [25, 27, 183, 184]. In brief, animals were anesthetized by 1.5% isoflurane/oxygen using an isoflurane vaporizer (Vet Equip, Pleasanton, CA). The body temperature was maintained using an electric heating pad under a dissecting microscope. A 30 Gauge needle was connected to a saline reservoir hung 1.5 m above the operating table. This needle was inserted into the vitreous space of the right eye for one hour. The left eyes were left intact to serve as the internal control for each animal.

MRI-DTI

Seven mice were used for longitudinal DTI evaluation. Imaging was performed 3 days and 1, 2, and 4 weeks after retina ischemia. Animals were anesthetized using 1.5% isoflurane/oxygen using an isoflurane vaporizer (Vet Equip, Pleasanton, CA). Core body temperature was maintained by a circulating warm water pad. The mouse was placed in a holder to immobilize the head. A 7-cm inner volume coil was used as a transmitter coil and a 1.5-cm inner diameter surface coil was used as a receiver to collect data on a Bruker BioSpec 4.7T small animal MRI instrument.

Spin-echo DTI was performed with repetition time (TR) 2 s, echo time (TE) 29 ms, time between gradients (Δ) 20 ms, gradient duration (δ) 3 ms, and six-direction diffusion scheme with b-values of 0 and 0.85 ms/μm^2. Field of view was 1.5 cm x 1.5 cm, and the matrix of 128 x 128 was zero-filled to 256 x 256. Thirteen contiguous slices with 0.5 mm

thickness were collected to cover optic nerves and tracts [127]. Data were collected three times. An ordinary-least-squares method was used to derive tensors on a voxel-by-voxel basis using software written in Matlab (MathWorks, Natick, MA, USA) [185]. The eigenvalues (λ_1, λ_2, and λ_3) of diffusion tensors were used to calculate axial diffusivity (AxD), radial diffusivity (RAD), relative anisotropy (RA), and trace of the diffusion tensor (TR) defined by the following equations:

$$TR = \lambda_1 + \lambda_2 + \lambda_3 \quad [1]$$

$$AxD = \lambda_1 \quad [2]$$

$$RAD = 0.5 \times (\lambda_2 + \lambda_3) \quad [3]$$

$$RA = \frac{\sqrt{(l_1 - Tr/3)^2 + (l_2 - Tr/3)^2 + (l_3 - Tr/3)^2}}{\sqrt{3}\,(Tr/3)} \quad [4]$$

Gd-T1WI

Omniscan (gadodiamide, GE Healthcare) was mixed with Saline (Lactated Ringer's Injection, USP) and Heparin (Heparin Sodium Injection, USP) in a 1:2.5:2.5 ratio. A triple dosage of Gd solution (0.3 mmol/kg or ~ 90 µl injection for a 25 g mouse) was injected via a tail vein. At one and four weeks following retinal ischemia, seven mice were anesthetized and placed in a holder to immobilize the head. The 4.7 T MRI, which was used for DTI collection, was not available for use, so a 3-cm volume coil was used to collect data in a Bruker 11.7T small animal MRI instrument. T1 weighted images (T1WIs) were collected using a spin-echo sequence with TR 500 ms and TE 14.5 ms. Nine contiguous slices were gathered with slice thickness of 0.75 mm to cover the left

and right optic nerves and tracts. Field of view was 1.5 cm x 1.5 cm, and the matrix of 128 x 128 was zero-filled to 256 x 256. T1WIs were acquired before and 5 minutes after the Gd injection. In addition to T1WIs, a T2-weighted Rapid Acquisition with Refocused Echoes (RARE) with TR 1s, echo train 4, and effective TE of 28 ms were collected with geometric parameters matching T1WIs to provide images to visualize the ON and OT [186].

Regions of Interest (ROI) Analysis

From our DTI data, regions of interest (ROIs) including the ON and OT were selected manually using RA and RAD maps. The ON and OT appear bright on RA and dark on RAD in comparison to neighboring CSF and grey matter. In both healthy and injured conditions, the intensity contrast remained suitable for ROI selections (Figure 2.1). For Gd-T1WI measurements, selections were performed using RARE images collected immediately prior to the Gd-T1WI scan. Using RARE images, white matter from the ON and OT was identified based on intensity contrast, with white matter appearing darker than surrounding grey matter and CSF. For each ROI, only the central portion of the ON and OT was selected. For the ON, ROIs were selected from the central 2x2 - 3x3 portion of voxels. Each ON measurement is composed of selections from two contiguous slices. For the OT, the central 25-30 voxels were selected. ROI analysis was performed in a blind fashion by J. Mei and C. Nishioka; both have more than 3 years of experience in mouse brain imaging [144, 185, 187].

Evans Blue Assessments

Mice 1, 2, and 4 weeks after retinal ischemia (N = 7) received a tail vein injection at a dosage of 1 mL/Kg of 2% Evans Blue tracer (E-2129, Sigma, St. Louis, MO) dissolved in normal saline. One hour after the injection, animals were anesthetized and transcardially perfused with PBS followed by formalin. The brains were quickly removed, post-fixed for 1 hour then sunk in 30% sucrose. Brain blocks were snap-frozen in dry ice. For each mouse brain, 2-mm blocks anterior and posterior to Bregma were cut for sections of optic nerve and optic tracts, respectively. Cryostat sections with 20-μm thickness were prepared for fluorescent microscopy. An Olympus FluoView Confocal microscope with laser wavelength of 620 nm was used to examine the brain sections. The Evans Blue extravasation was quantified by measuring signal intensity using ImageJ software.

Immunohistochemistry of SMI-31, MBP and Iba1

A 4-mm-thick coronal section (-1 to +3 mm of Bregma) was obtained from each brain and embedded in paraffin. The integrity of axons was evaluated using a primary antibody against phosphorylated neurofilament (pNF, SMI-31, 1:1000; Sternberger Monoclonals, Lutherville, Maryland), and myelin integrity was assessed with a primary antibody against myelin basic protein (MBP, 1:250; Zymed Laboratories Inc., South San Francisco, CA) at 4°C overnight [25]. Following three 5 minute washes in PBS, sections were incubated in fluorescent secondary antibodies for one hour at room temperature (1:200, anti-mouse conjugated to Alexa 488 for SMI-31, 1:200, anti-rabbit conjugated to Texas red for MBP; Molecular Probes). The ionized calcium-binding adapter molecule 1

(Iba1) was used to evaluate macrophages / microglia. Brain slices were cut on a microtome at 5uM. Sections were incubated with primary antibody (Wako Rabbit anti-Iba1, 0.25 ug/mL) overnight at room temperature. Sections were then washed with PBS, and incubated in biotinylated secondary antibody (Vector) for 30 minutes. Sections were then washed, and incubated in strepavadin-HRP (Vector) for 30 minutes. After washing, sections were developed with DAB substrate.

Histological sections were examined using an Olympus Fluoview Confocal Microscope equipped with a 60× oil objective by H. Liang, who has more than 5 years of experience of microscopic imaging [127]. Under a microscope, images were taken from the central portions of the left and right ON and OT respectively. The positively labeled axons were counted through the central 100 × 100 μm^2 region.

Statistical Analysis

Data are presented as mean ± standard deviation. Changes in diffusion metrics and Evan's blue staining were computed by calculating the diffusional asymmetry (injured side, left ON and right OT divided by the contralateral control side). Comparisons between asymmetry metrics were performed using a one-way analysis of variance (ANOVA) followed by a post-hoc Dunnett's test to compare each timepoint to baseline (day 0) measures. Immunohistochemistry comparing axon/myelin/Iba1 staining and Gd-enhancement data between injured and control ONs/OTs were performed using a

student's t-test. Data analysis was conducted using Prism Graphpad. $p < 0.05$ was considered to be statistically significant.

Results

In vivo DTI Findings

The ROI measurements from the ON and OT after retinal ischemia are summarized in Figure 2.2B. In the ON, AxD asymmetry measures gradually decreased across the time-course, reflecting reductions in AxD in the injured nerve, relative to the control side. Asymmetry at baseline (1.05) decreased by 19% after one week (0.849, ns), 25% after two weeks (0.784, $p<0.01$), 35% after three weeks (0.685, $p<0.001$), eventually reaching a 32% reduction (0.714, $p<0.001$) after four weeks. The changes in AxD were delayed in the OT, relative to the ON. Changes in OT AxD asymmetry were significant beginning after three weeks with a 22% reduction relative to baseline (0.756, $p<0.01$), with a similar 23% reduction after four weeks (0.743, $p<0.01$).

Significant increases in RAD asymmetry, reflecting increases in diffusion within injured nerves were found one week after the co-located decrease of AxD. In the ON, RAD did not show significant increases versus baseline asymmetry (1.01) until three weeks after retinal ischemia (1.86, $p<0.05$). Similar magnitudes of change were observed after four weeks (1.80) though they were not statistically significant. In the OT, RAD asymmetry increases reached statistical significant after four weeks (1.86, $p<0.05$)

Significant reductions in RA asymmetry in the ON and OT were also observed, with reductions versus baseline measures (1.01) in the ON after two (0.86, $p<0.05$), three (0.757, $p<0.001$) and four (0.76, $p<0.001$) weeks. In contrast to the ON, significant changes in OT RA asymmetry were only significant after four weeks (0.701, $p<0.01$).

Reductions in TR asymmetry were also apparent in this model. Relative to baseline asymmetry (1.11), significant reductions were apparent after one week (0.87, $p<0.05$) and again at each subsequent timepoint after 2 (0.86, $p<0.05$), 3 (0.82, $p<0.01$) and 4 (0.86, $p<0.05$) weeks. Relative to the ON, changes in OT asymmetry versus baseline (0.992) were only significant after three weeks (0.86, $p<0.05$).

Immunohistochemistry of SMI-31 and MBP

The immunohistochemical examination using SMI-31 showed that axonal density was reduced by 11% ($p = 0.0116$), 23% ($p = 0.0003$), and 41% ($p = 0.0013$) in the injured ON at one, two, and four weeks after retinal ischemia, respectively. In the OT, axonal density was not changed after one week, but was reduced by 9% ($p = 0.0056$) and 39% ($p = 0.0091$) at two and four weeks after retinal ischemia (Figure 2.3). The immunohistochemical examinations using MBP showed no significant changes in the ON and OT before one and two weeks after retinal ischemia, but showed ~30% reduction ($p = 0.0001$ in ON and $p = 0.0086$ in OT) of myelinated axon counts in both regions of WldS mice four weeks after retinal ischemia (Figure 2.4).

Gd-T1WI

There was no noticeable signal enhancement in the brain after Gd-T1WI at any time point after retinal ischemia (Figure 2.5). Our ROI analysis found no changes in enhancement within the injured ON and OT, compared to controls. Outside the brain, noticeable enhancement was present in several regions, including the pharyngeal wall, which showed a 4 – 6 -fold increase ($p = 0.0001$) in signal enhancement (Figure 2.5c).

Evans Blue staining

As shown in Figure 2.6, the injured ON and OT showed a 1 – 2 -fold increase in staining intensity compared to controls beginning one week after retinal ischemia. These differences were statistically significant in the damaged ON at 2 weeks and damaged OT at 1 and 2 weeks after retinal ischemia.

Iba1

As shown in Figure 2.7, slightly enhanced coverage of Iba1 was found in the injured ON and OT two weeks after retinal ischemia. This elevation of Iba1 reached significance (~ 4-fold increase) after four weeks in both the ON and OT.

Discussion

Decreases in AxD followed by increases in RAD have been reported to detect axonal and myelin damage in white matter with axonal degeneration [25, 184, 188]. Using WldS mice, we observe the same DTI alterations in ON and OT after retinal ischemia. The damage to axons followed by co-located myelin loss were detected by DTI and confirmed by histology. This pattern of observed DTI changes reveals the temporal evolution of

pathology during and following acute axonal degeneration. The same array of DTI changes have also been reported in humans during Wallerian degeneration [168-171], suggesting some commonalities in axonal degeneration across diseases and species.

In addition to characterizing the temporal evolution of axonal degeneration, it is also important to understand its spatial evolution. Both ON and OT contain axons originating from the same neurons in the retina. We have previously attempted to use DTI to track degeneration in the ON and OT after retinal ischemia. Using wild type mice, we found that both the ON and OT exhibited axonal disruption concurrently three days after retinal ischemia [25, 184, 188]. This rapid degeneration did not allow us to differentiate the regional variation between the ON and OT. This fast form of degeneration in mice may not reflect the slower process of axonal degeneration in the human CNS [166, 189].

In our experiment using WldS mice, the axonal damage in the OT (the distal portion of RGC axons) was detected after axonal damage in the ON (a proximal portion of RGC axons), suggesting an anterograde degeneration process propagating from cell bodies toward the axonal terminals. Several previous studies have attempted to characterize the spatial-temporal profile of axonal degeneration. *In vitro* work by George et. al. examined granular disintegration of the cytoskeleton in a rat dorsal radiculotomy model and estimated a degeneration speed of ~ 3 mm/hr along axons emanating from the initial damage sites [165]. Data by Öztürk et. al. supports the idea that there are distinct axonal degeneration patterns, either with fragmentation or retraction steps during dying-back

degeneration. These patterns were related to the survival or death of the neuronal cells [164]. As such, different spatial patterns of axonal degeneration may represent pathways critical to neuronal fate in neurodegenerative conditions. Our study does not intend to predict axonal degeneration rates in humans based on our animal data. Instead, our study illustrates the possibility of using longitudinal DTI to characterize ongoing axonal degeneration and to differentiate subtypes of neurodegenerative conditions. This characterization may allow for differentiation from occurrences of 'dying back' degeneration, which has been implicated in several diseases including Amyotrophic Lateral Sclerosis (ALS) [190].

In MS, Gd-T1WI is routinely used to detect active inflammatory lesions. While focal damage can precipitate axonal degeneration towards remote brain areas, white matter with axonal degeneration is generally considered to appear normal without enhancement on Gd-T1WI [181, 182]. As predicted, we found no visible enhancement within the injured ON and OT after retinal ischemia. However, when the tissue was examined using Evans Blue, higher signal was observed, suggesting an infiltration and accumulation of serum albumin into the damaged white matter. To explain this, we note that several studies have confirmed that extensive inflammatory activities exist in damaged white matter without causing enhancement on Gd-T1WI [191, 192]. Albumin is long known to be one of the acute-phase proteins in response to inflammation [193]. As its key functions involve wound healing [194], we speculate that albumin may be transported into the injured sites for tissue repair.

Previous studies have suggested that microglia/macrophage activity in axonal degeneration within the CNS is delayed compared to degeneration in the peripheral nervous system (PNS) [165, 182, 195]. As such, the delayed microglia/macrophage activity in our study was not a surprise. It is noted that even when significant microglia/macrophage activity was detected at the final time point, there was still no BBB leakage detectable by Gd-T1WI. Our data supports the view that BBB permeability remains low in white matter with extensive axonal degeneration and inflammation. According to our results, it seems likely that Gd-T1WI can specifically detect initial autoimmune lesions in MS without confounding factors from secondary axonal degeneration.

While our study demonstrates the capability of DTI to characterize the temporospatial profile of axonal degeneration, limitations must be considered before generalizing our results to other models systems and human disease. Our study was conducted using WldS mice, which show delayed axonal degeneration [9, 196]. This form of degeneration is more gradual than the rapid process in wild type mice and may reflect different underlying mechanisms. Considerations of our procedure are also relevant to interpreting the results. Within our experimental procedure, ROI selections were made by two experienced operators manually. Studies using more objective approaches, such as automatic white matter segmentation [197], as well as with a larger amount of samples, may provide data to better describe the temporospatial profiles of degeneration. Further research is required for understanding to what degree our findings can be generalized to other white matter pathways in wild type mice and in conditions of human disease.

In conclusion, using longitudinal DTI on ON and OT of mice after retinal ischemia, decreased AxD followed by increased RAD were observed and these changes were associated with the axonal damage followed by myelin loss. The early ON damage followed by OT damage shows the spatial evolution of axonal degeneration that propagates from cell bodies to distal axonal terminals. Injured white matter within the ON and OT appear normal on Gd-T1WI, which is consistent with clinical findings in MS. While the BBB remains tight, infiltration and accumulation of albumin detectable by Evans Blue suggests an early inflammatory response in the degenerating nerves.

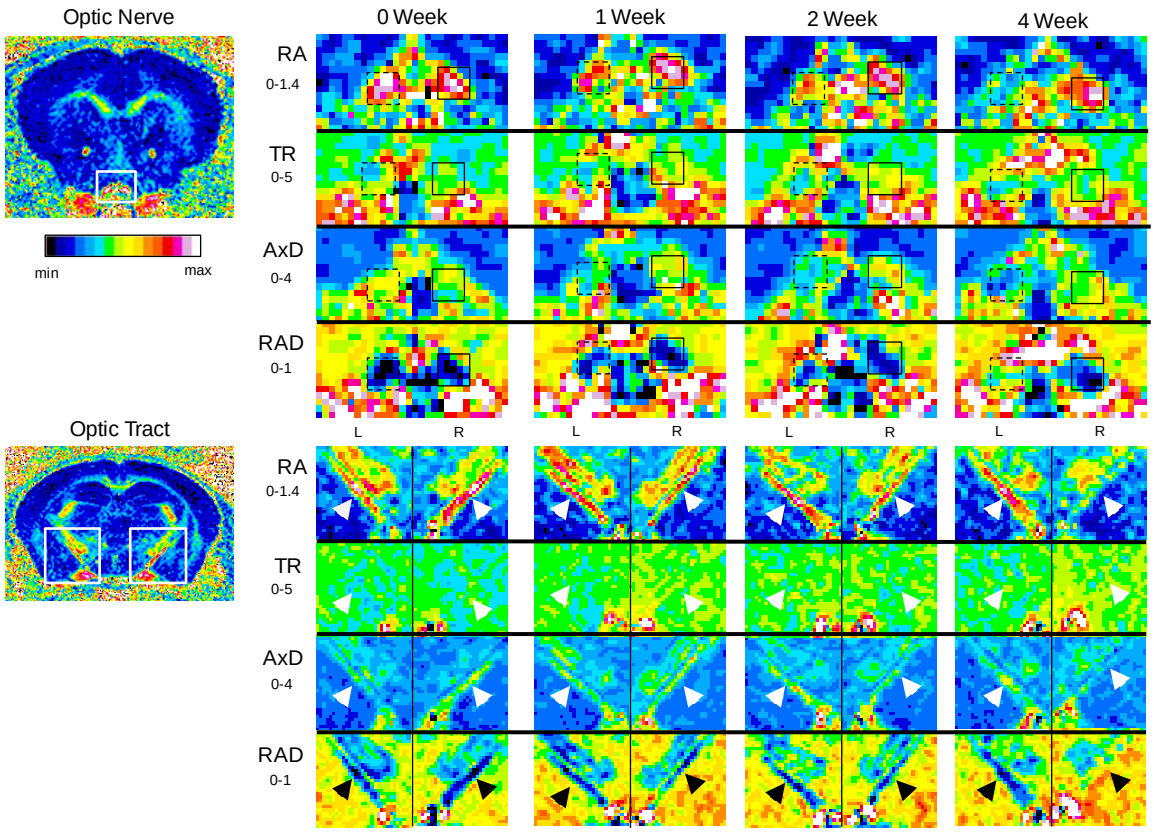

Figure 2.1 DTI maps of ON and OT in mice after retinal ischemia Individual metrics are pseudocolored to show relative differences between the injured and control tracts. The injured ON is on the left, indicated by dashed boxes, with corresponding control ON to the right. The majority of RGC axons cross the chiasm and project into the opposite hemisphere of the brain, so the right side of the OT is injured (all OTs shown by white and black arrows). Longitudinal changes first appear in the ON after 1-2 weeks by relative reductions in TR, AxD and RA within injured nerves. Later alterations in the OT by reductions in RA, TR AxD and RAD manifest after 4 weeks. TR, AxD and RAD measures in units of 10^{-3} mm^2/s.

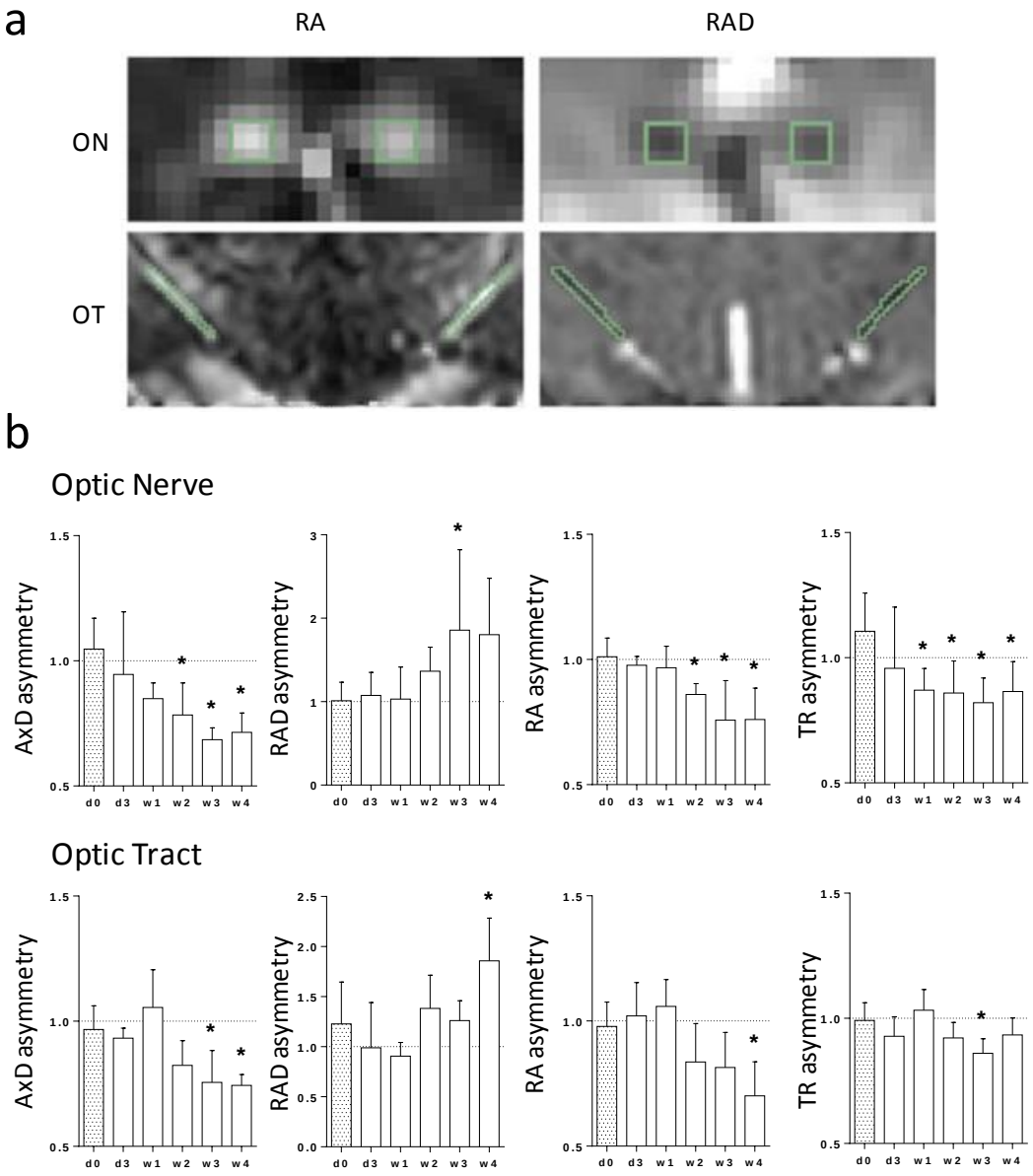

Figure 2.2 DTI asymmetry metrics from the ON and OT in mice after retinal ischemia The top panel (A) shows an example of ROI selections from the ON and OT on RA and RAD maps. ROIs were selected in the central portion of ON and OT using synchronized tracing on RA and RAD maps. The bottom panel (B) shows a summary of the measurements. The injured ON and OT showed gradual decreases in AxD , RA and TR asymmetry and gradual increases in RAD asymmetry relative to baseline measures (day 0 measures, d0, shaded bars). The significant changes in DTI asymmetry occur 1 – 2 weeks before changes manifest in the OT. The "*" indicates significant differences at $p < 0.05$, compared with baseline measurements of asymmetry.

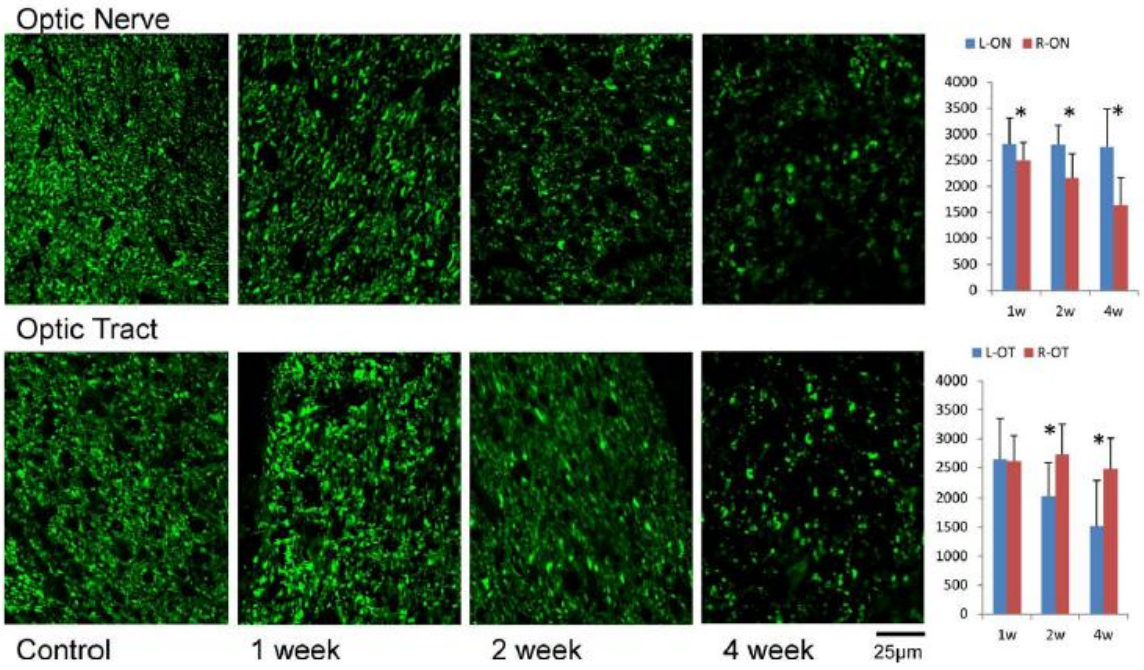

Figure 2.3 SMI-31 immunohistochemistry in the ON and OT after retinal ischemia The density of SMI-31 positive axons (axon counts in 100x100 μm^2) is summarized in the bar graphs (right, N = 7). The "*" indicates significant changes ($p < 0.05$). The right ON and left OT showed degeneration as gradual loss of SMI-31 axon counts, examined at 1, 2, and 4 weeks after retinal ischemia. The loss of axons was significant in the ON beginning at week 1, but gained significance in the OT after two weeks.

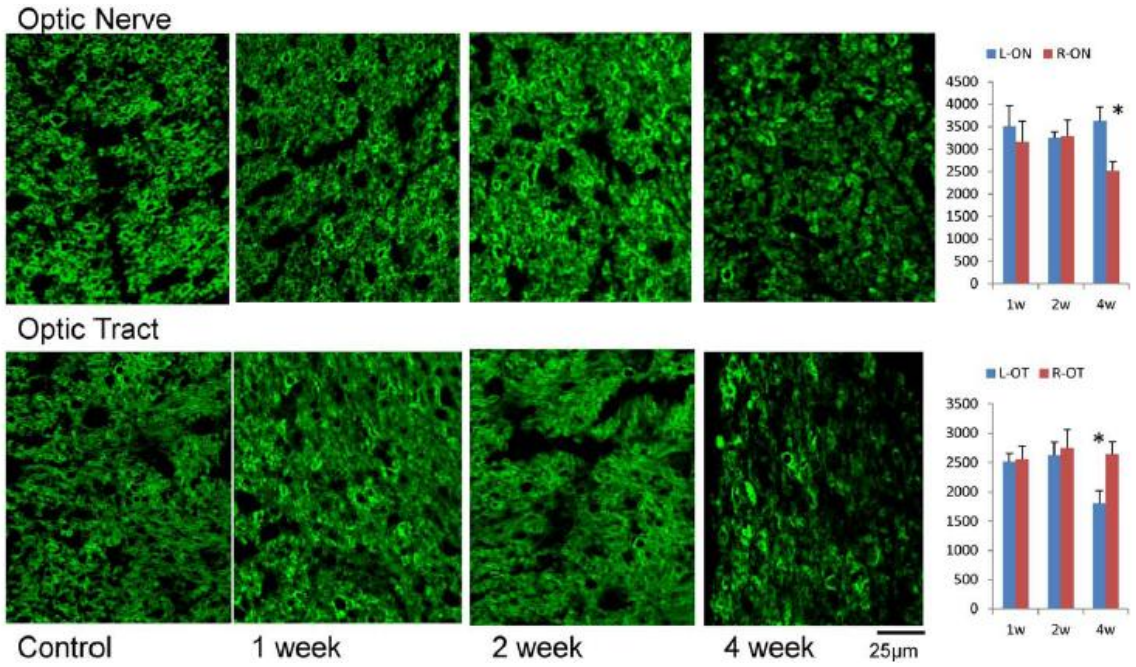

Figure 2.4 MBP immunohistochemistry in ON and OT after retinal ischemia The density of MBP positive axons (axon counts in 100x100 μm^2) is summarized in bar graphs. The "*" indicates significant changes ($p < 0.05$). Both ON and OT showed significant myelin loss four weeks after retinal ischemia.

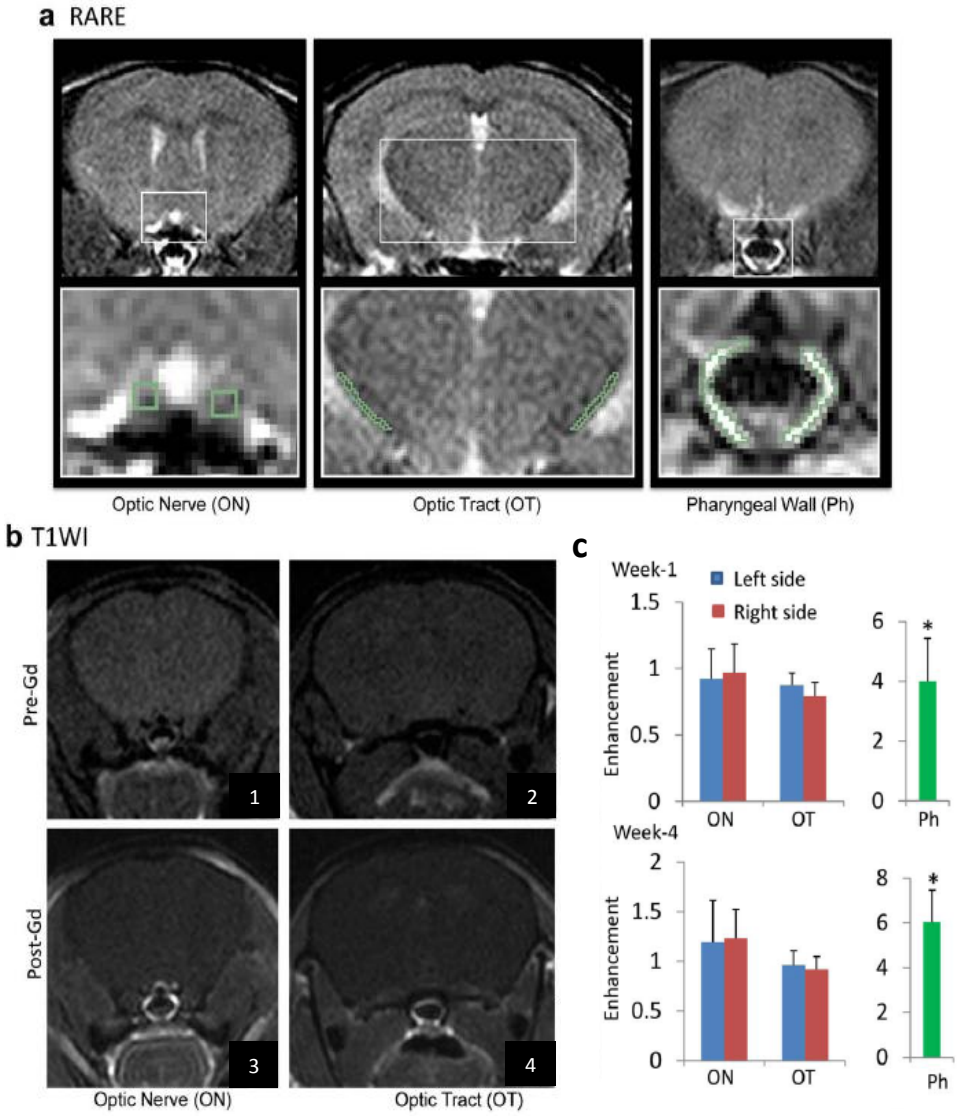

Figure 2.5 Gd-T1WI of mice after retinal ischemia Panel A shows examples of RARE images, which provide contrast between grey matter, white matter, and CSF, allowing identification of the ON and OT. Panel B shows examples of T1WI images before and after Gd injection. Pictures 1 and 2 show pre-Gd T1 ON and OT, with 3 and 4 showing the regions post-Gd-T1. There is no significant enhancement in the brain, including either in the ON or OT (c). Noticeable enhancement was found in several regions outside the brain, including the pharyngeal wall, which showed a 4 – 6 -fold enhancement over baseline (Ph, green bar). "*" indicates significance at $p<0.05$.

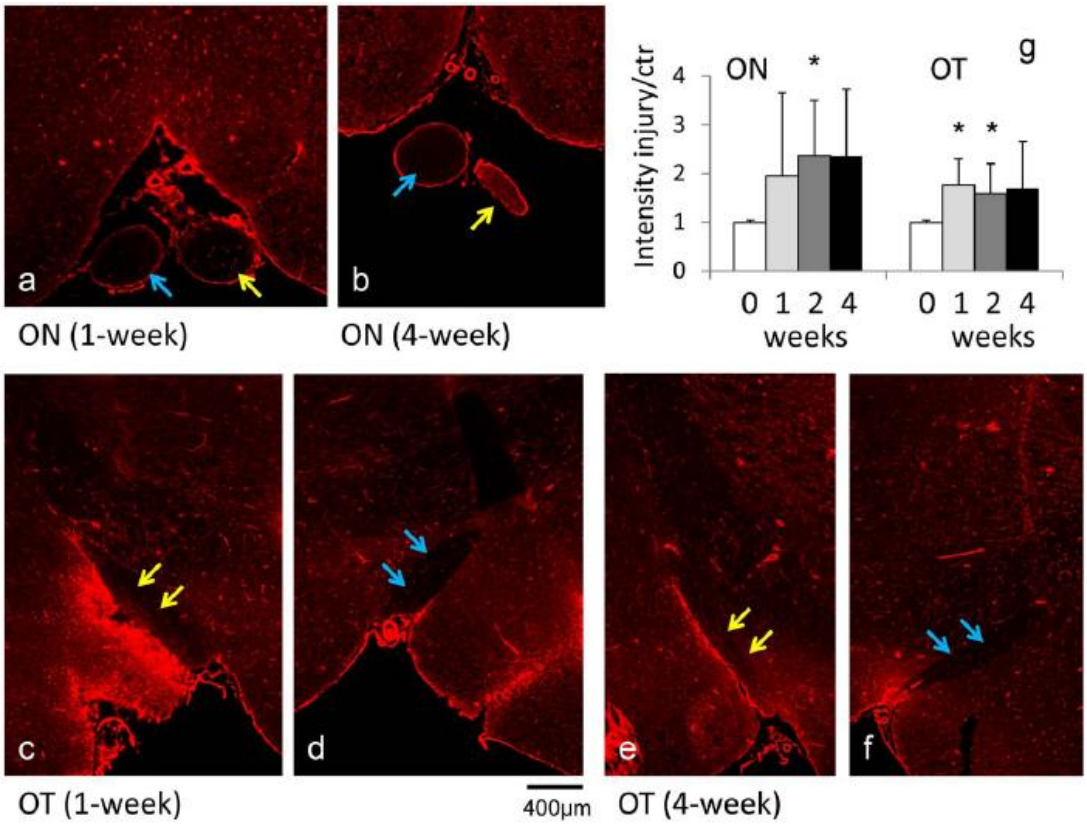

Figure 2.6 Evans blue staining (a - f) of the ON and OT after retinal ischemia Evans blue dye detects the presence of albumin. The injured ON (yellow arrows in a and b) and injured OT (yellow arrows in c and e) showed stronger signal than the contralateral ON (blue arrows in a and b) and OT (blue arrows in d and f), respectively. The signal intensity analysis (g) showed increased signal in the injured ON and OT beginning one week after retinal ischemia. The "*" indicates significant at $p < 0.05$, compared to controls.

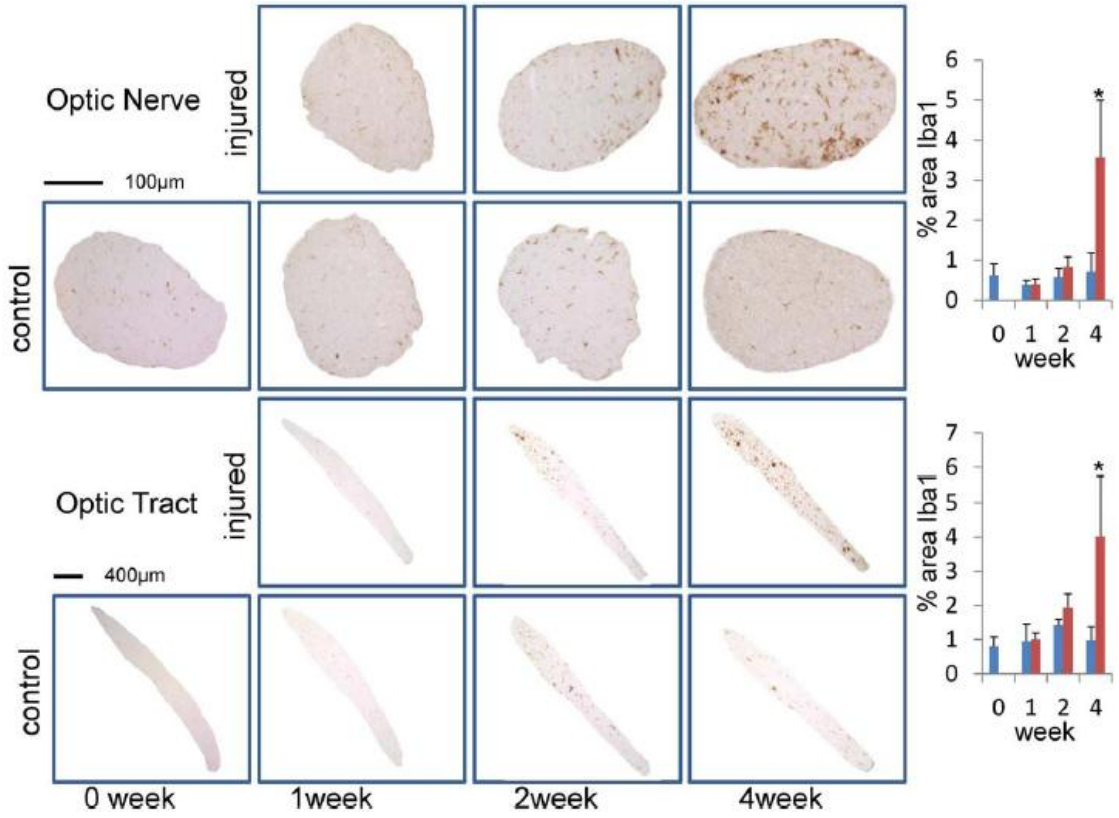

Figure 2.7 Iba1 staining in ON and OT after retinal ischemia The percent area of Iba1 positive microglia is summarized in bar graphs (right). The "*" indicates significant changes at $p < 0.05$. Both ON and OT showed significant increases in Iba1 staining four weeks after retinal ischemia.

Chapter III:

Sequential phases of RGC axonal and somatic injury in EAE mice examined using DTI and OCT

Abstract

Purpose: Clinical imaging modalities including Optical Coherence Tomography (OCT) and Diffusion Tensor Imaging (DTI) are vital in Multiple Sclerosis (MS), but their relationships during the different phases of Retinal ganglion cell (RGC) degeneration are not clear. We hypothesize that initial injury in optic nerve (ON) causes axonal degeneration leading to RGC loss in retina, which can be characterized by combination of DTI and OCT. Our objective was to analyze the correlation between noninvasive and histological data to chronicle the degeneration profile of RGCs in the retina and ON in a mouse model of MS.

Materials and Methods: Experimental Autoimmune Encephalomyelitis (EAE) was induced in 11 C57Bl/6 mice, with 8 mice reserved as controls. Longitudinal OCT and DTI was conducted 2-8 weeks after induction of EAE. The thickness of the retinal ganglion cell complex (GCC) was measured using OCT and compared to DTI indices measured in optic nerves. End-stage histology was used to quantify axon/myelin loss in the optic nerve and retinal thinning / RGC loss in the retina.

Results: Significant changes in ON DTI-derived Axial Diffusivity (AxD, -17.2%) and Trace Diffusivity (TR, -18.3%) began after 2 weeks of EAE. Later significant reductions in Fractional Anisotropy and AxD, with increases in Radial Diffusion (RAD) were apparent after 4 and 8 weeks. OCT-derived measures of GCC thickness were reduced

after 4 weeks, and reached significant reduction after 8 weeks. Among EAE mice, DTI (FA, AxD and RAD measures) and OCT measures were all significantly correlated in a linear fashion after 4 and 8 weeks. Among histology measures, RGC density (-19%), RGC size (-26%), and the number of SMI31+ axons (-54%) were reduced significantly. DTI measures of FA and AxD along with GCC thinning were the best independent predictors of axon loss.

Conclusions: DTI and OCT measures are tightly correlated during the chronic phase of axonal degeneration (4-8 weeks) in EAE mice. After 8 weeks of EAE, both OCT and DTI measures are strong predictors of axon loss in the Optic Nerve.

Introduction

Multiple Sclerosis (MS) is a chronic inflammatory disease characterized by demyelination, axonal damage and neurodegeneration throughout the central nervous system (CNS). Permanent clinical disability of MS is thought to result primarily from cumulative axonal and neuronal losses [198]. Magnetic Resonance Imaging (MRI) is the gold standard technique for the diagnosis of MS, but conventional (T1 and T2) imaging methods are not specifically sensitive to axonal and neuronal losses. The inflammatory lesions visible by MRI have variable outcomes in terms of long-lasting axonal damage. A discord between imaging findings and clinical manifestation has been recognized and new imaging tools are needed to better detect the underlying neurodegeneration in MS [199].

Among CNS white matter tracts, the Optic Nerve (ON) is a frequently affected site in MS. Over 90% of MS patients present identifiable lesions in ON [200, 201]. Diffusion tensor imaging (DTI) is an imaging technique sensitive to white matter microstructure, allowing greater sensitivity to underlying neurodegeneration at the tissue level. Metrics derived from the DTI model have shown sensitivity to different neurodegenerative events in white matter; increased radial diffusivity (RAD, diffusion across fibers) has been shown to correspond to demyelination, while axonal damage leads to changes in axial diffusion (AxD, diffusion along fibers) [26, 145, 202] . Axial diffusivity has been shown sensitivity to degrees of axonal loss in animal models of MS [203, 204] and to predict visual outcomes in human MS [205].

Optical Coherence Tomography (OCT) is another relatively new technique that has quickly gained acceptance in the field of MS [206-211]. Detectable retinal thinning occurs during MS and is concentrated within the most superficial layers, containing RGC axons (Retinal Nerve Fiber Layer, RNFL), cell bodies (Ganglion Cell Layer, GCL) and dendrites (Inner Plexiform Layer, IPL) [212]. Measurements of these changes in the eye have been proposed as diagnostic markers for the rate of nerve injury and cell loss during the disease [210]. Several clinical studies, including a long-term 4 year longitudinal study, have linked changes in OCT-measured thinning to MRI-measured brain atrophy [206-208] and patient disability [209-211], suggesting that OCT may be a useful surrogate to measure and track underlying neurodegeneration during the course of MS.

Presumably, different imaging modalities have distinct sets of advantages (and disadvantages) during different stages of axonal degeneration in MS. However, it is presently unclear how these data relate to each other during the progressive neurodegeneration that manifest during disease. A combination of DTI and OCT data may provide complementary information to characterize the progression of RGC degeneration. In the present study, we utilized the Experimental Autoimmune Encephalomyelitis (EAE) model to characterize changes in the afferent visual system using DTI and OCT in a longitudinal manner. The underlying changes using these modalities was compared during the disease course and evaluated in relation to ground truth tissue histology. These results provide better understanding of DTI and OCT data in monitoring optic nerve degeneration, which provide new insights for improved clinical management of MS.

Materials and Methods

Animal Preparation

This study was conducted in accordance with National Institutes of Health guidelines and Statement for the Use of Animals in Ophthalmic and Visual Research, and was approved by the Institutional Animal Care and Use Committee at Loma Linda University.

Experimental Autoimmune Encephalomyelitis (EAE) was induced in 11 female, twelve week old C57Bl/6 mice using 100μg Myelin oligodendrocyte glycoprotein (MOG), emulsified in incomplete Freund's adjuvant (IFA). Pertussis toxin (200ng, Sigma) was

injected IP on the day of immunization and three days post-immunization. Eight female mice were reserved from treatment in the control group. Mice were graded every three days to track disease activity on a clinical scale between 1-5 (Figure 3.1). Values ranged from 0 (no symptoms), 1 (weak tail), 2 (hind limb weakness), 3 (unilateral hind limb paralysis), 4 (bilateral hind limb paralysis) to 5 (death). OCT scans were acquired at baseline, before immunization and then again after 2, 4 and 8 weeks after immunization in the EAE and after 8 weeks in the control group. DTI scans from EAE mice were acquired after 2 weeks (N=4, 8 ONs total), 4 (N=7, 14 ONs total) and 8 weeks (N=7, 14 ONs total). Control mice were scanned after 8 weeks (N=8, 16 ONs total).

MRI acquisition, processing and Analysis

MRI acquisitions were collected using a Bruker 11.7T BioSpec small animal MRI instrument with slice thickness 0.5mm, FOV of 1.5 x 1.5cm and matrix 128 x 128 (zero filling to 256 x 256), TR 2.5s, TE 29ms, Δ20ms, δ 3ms and a 21-direction diffusion scheme with b=0.85ms/um^2, and two non-diffusion weighted scans. Raw diffusion-weighted images were processed using FSL (http://fsl.fmrib.ox.ac.uk/fsl/fslwiki/FDT), including steps for skull stripping and eddy current/motion correction using BET and Eddy modules, respectively. Corrected image sets were then loaded into 3D Slicer, where eigenvalues derived from the diffusion tensor were used to calculate AD, TR, RAD and FA, defined by the following equations:

$$AxD = \lambda_1 \quad (1)$$

$$TR = \lambda_1 + \lambda_2 + \lambda_3 \quad (2)$$

$$RAD = (\lambda_2 + \lambda_3) * (1/2) \quad (3)$$

$$ADC = TR / 3 \quad (4)$$

$$FA = \sqrt{\frac{3}{2}} \frac{\sqrt{(\lambda_1 - ADC)^2 + (\lambda_2 - ADC)^2 + (\lambda_3 - ADC)^2}}{\sqrt{\lambda_1^2 + \lambda_2^2 + \lambda_3^2}}$$

Analysis of the optic nerve was carried out in coronal sections using procedures previously described [213]. In brief, optic nerves were selected based upon FA/RAD maps, in which high FA and low RAD excluded the possibility of selecting neighboring CSF. The central 3x3 portion of voxels through four sequential slices (N=36 voxels per ON) were manually selected in each optic nerve by a blinded observer.

Optical Coherence Tomography acquisition and analysis

OCT imaging was performed using a BioOptigen Envisu C-Class. Our imaging protocol collected data from a 1.6 x 1.6 mm region centered on the optic disc. The protocol used 1000A scans/B Scan, 100 B scans total. B scans 320um and 240um superior and inferior to the optic disc (N=4 per eye) were selected for analysis. These regions were selected for their consistent layer thickness characteristics. Images were processed and analyzed using software created in Matlab (Natick, MA). The procedures are illustrated in Figure 3.2 Specifically, individual B scans were pre-processed by manually cropping retinal edges and removing segments containing blood vessels along the RNFL surface (3.2a). A fitted quadratic curve was then used to adjust individual A-scan positions to flatten the retina (3.2b). With each straightened B scan, all A scan values were averaged, and the profile of

intensity variation across of retina was plotted (3.2d, 3.2e). All scans were manually reviewed by a blinded observer to assure the straightness of each B scan after processing. As shown in Figure 3.2e, the measurement of Ganglion cell complex (GCC) thickness (composed of axons, soma and dendrites of RGCs) was made based upon the intensity differences between retinal layers. Thickness was defined as the distance between retinal nerve fiber layer (RNFL) peak intensity and the intermediate border between the inner plexiform layer (IPL) maxima and the underlying Inner nuclear layer (INL) minima. The reliability of our method was tested using three control mice (N=6 eyes), scanned every week from 12-19 weeks of age (Figure 3.2f). These measurements revealed 1.17% average thickness variation between each week.

Histology

All mice were sacrificed after 8 weeks of EAE. A subset were processed for use in histology (N=7 EAE [14 ONs/Eyes], N=5 Control [10 ONs/Eyes]). Mice were anesthetized and perfused with PBS and Hartman's fixative. After perfusion, tissues were put into decalcification buffer for one week. Tissues were then sliced into 3mm-thick sections and processed for paraffin embedding. Resulting paraffin blocks were then sectioned at 5μm for sections of optic nerve and retina.

Sections of optic nerve were immunostained for markers of healthy axons (phosphorylated neurofilament, SMI-31) and myelin sheaths (Myelin basic protein, MBP). Briefly, sections were deparaffinized, permeabilized in 0.3% Triton X-100,

blocked in 3% NGS then incubated overnight in 1˚ antibodies. Sections were then incubated in 2˚ antibodies for 1hr and mounted for imaging. Slides were imaged using a Keyence fluorescence microscope using identical acquisition settings. In the ON, axon numbers were measured using coronal sections through each nerve. Stained ONs were imaged using a 40x objective, then analyzed using the threshold and analyze particles segmentation functions in ImageJ.

Three central sections from each retina were selected for H&E staining. Stained sections were analyzed using images acquired at 40x using ImageJ. Retinal sublayers were measured at three locations within each retina, within 500um of the central portion of the retina. RGC cell bodies were selected for morphological assessment of cross sectional area (CSA). RGCs were selected for measurement every tenth cell body across the tissue section.

Statistical Analysis

All statistical calculations were carried out in Prism 6.0. Comparisons of MRI and OCT data between control, baseline, 2, 4 and 8 week EAE groups was performed using a one-way ANOVA followed by post-hoc Tukey's test. Analysis of histology data comparing control to EAE groups was done using an unpaired t-test. Correlation between MRI/OCT, MRI/histology and OCT/histology datasets was performed using a Pearson's correlation coefficient. All *p* values below $p<0.05$ were considered statistically significant.

Results

EAE Mice

A record of clinical symptoms in the mice is shown in Figure 3.1 Mice began to show clinical symptoms 10-12 days after immunization. These symptoms were present in all mice after three weeks. The disease activity was chronic, with slowly increasing average severity over eight weeks.

OCT Findings

Analysis of OCT scans from control and baseline EAE mice show an average GCC thickness of 58.1±2.2μm. The mean thickness in the EAE group transiently increased after 2 weeks of EAE, rising to 61.1±2.1μm. Assessment after four weeks showed average thickness was reduced to 55±4.2μm (not significant). After eight weeks, average thickness significantly decreased relative to baseline measurements, falling to 53±2.6μm ($p<0.01$) (Figure 3.3).

OCT vs. retinal histology

Analysis of the retinal histology by H&E confirmed our OCT findings (Figure 3.4). The RNFL/GCL layer thickness was reduced by 29% ($p<0.0001$), while the IPL was reduced by 13.8%. Alterations to the ganglion cell layer were apparent in the EAE group, relative to controls. Both RGC density (-19%, $p<0.01$) and RGC cross sectional area (-26%, $p<0.001$) were both reduced significantly. Measurements from our 8 week OCT data were significantly correlated with histology-derived findings (Figure 3.4). Total OCT-

measured GCC thickness was significantly correlated with both histology measured RNFL/GCL thickness ($r = 0.46$, $p = 0.027$), IPL thickness ($r = 0.54$, $p = 0.007$), RGC density ($r = 0.57$, $p = 0.004$) and cross sectional area ($r = 0.65$, $p = 0.0007$).

Optic Nerve DTI Findings

As shown in Figure 3.5, after two weeks of EAE we found highly significant reductions in ON TR (-18.3%, $p<0.0001$) and AxD (-17.2%, $p<0.01$), along with nonsignificant reduction in RAD (-18.1%). After 4 weeks we found significant reductions in FA (-28.6%, $p<0.0001$), AxD (-25.9%, $p<0.0001$) and increases in RAD (48.8%, $p<0.001$) while TR showed no difference from controls. Similar changes were seen after 8 weeks, with reductions in FA (-24.5%, $p<0.0001$), AxD (-16.0%, $p<0.001$) and increases in RAD (54.3%, $p<0.0001$).

OCT-DTI Correlations

Contemporary DTI and OCT measures were compared at each timepoint; correlation coefficients are shown in Figure 3.6. These associations were not significant in control mice or EAE mice after two weeks of EAE. All significant correlations between OCT and FA, AxD and RAD appeared after 4 or 8 weeks of EAE (Figure 3.6). Among all mice, FA ($r = 0.829$), AxD ($r = 0.467$), TR ($r= -0.4449$) and RAD ($r = -0.830$) were significantly correlated with OCT GCC thickness measures. In all cases, the relationship between DTI and OCT measures were more highly correlated after 8wks than after 4wks.

Optic Nerve Histology

Histology data confirmed our imaging findings, showing significant reductions in the numbers of healthy axons (SMI-31+) and variable demyelination, shown by reductions in MBP signal (Figure 3.7). Quantification of the staining data showed that EAE ONs had an average 54% reduction ($p<0.0001$) in the number of SMI31+ axons at the time of sacrifice, 8 weeks after induction of disease. The percent area occupied by MBP signal within the ON fell by 18.2% ($p<0.05$) in the EAE mice cohort.

Comparisons of OCT and DTI to axonal histology

Comparisons between DTI, OCT and histology datasets were performed to understand how each noninvasive measurement correlated with different degrees of axon loss measured after 8 weeks of EAE (Figure 3.8). To make these comparisons, we used DTI ON values measured at 4 and 8 weeks, OCT-measured GCC thicknesses (μm) and GCC thinning from each eye (OCT baseline – thickness). Correlational analysis reveals that DTI and OCT measures from before sacrifice at 8 weeks are superior to predicting axon numbers than earlier timepoints at 4 weeks. DTI measures of ON FA, AxD and RAD were all significantly associated with axon counts. FA ($r = 0.737$, $p = 0.0027$) and AxD ($r = 0.834$, $p = 0.0002$) were the most highly correlated DTI metrics. Measures of GCC thickness were non-significantly associated after 4 weeks and significantly associated at 8 weeks ($r = 0.728$, $p = 0.0031$). This correlation was improved if percent thinning from baseline was incorporated ($r = 0.744$, $p = 0.0023$ at 4 weeks, $r = 0.879$, $p<0.0001$ at 8 weeks).

Measurements from our 8 week OCT data were significantly correlated with histology-derived findings (Figure 3.4). Total OCT-measured GCC thickness was significantly correlated with both histology measured RNFL/GCL thickness ($r = 0.46$, $p = 0.027$), IPL thickness ($r = 0.54$, $p = 0.007$), RGC density ($r = 0.57$, $p = 0.004$) and cross sectional area ($r = 0.65$, $p = 0.0007$).

Discussion

This study has made the first direct comparisons between co-evaluated OCT and DTI metrics and histology-measures of axon loss and RGC damage in a longitudinal EAE model. Four important findings are highlighted: 1) Early changes to DTI properties in ON are detectable before OCT-detectable alterations to retinal thicknesses. 2) Gradual reductions in GCC thickness detectable by OCT begin after four weeks, and are associated with co-evaluated DTI-detected white matter integrity changes (FA, AxD and RAD) in the ON. 3) Alterations in OCT-GCC thickness after EAE can be predominantly accounted for by shrinkage within the RNFL/GCL sublayers. These changes include both loss and shrinkage of RGC cell bodies. 4) After 8 weeks of EAE, both DTI and OCT measures are highly predictive of the degree of axonal losses in the ON and RGC losses in the retina by histology.

Collectively, OCT and DTI findings are highly correlated during the chronic phases of disease, and both showed significant accuracy in detecting the degree of axonal

degeneration in EAE. Our data support the use of these *in vivo* biomarkers for longitudinal assessments during MS clinical management.

However, as our datasets are from mice, they need to be interpreted carefully. Compared with human retinas, the superficial layers in mice (disproportionally affected during EAE) are ~5x thinner, making accurate analysis challenging [214, 215]. Commercially available tools which utilize layer segmentation algorithms are known to be sensitive to noise and signal dropout [216]. These approaches frequently need to be reviewed manually to correct segmentation errors [217]. To overcome these challenges, we created a novel way to analyze murine OCT data. We first generated an intensity profile from each B scan, from which thickness of the GCC can be easily extracted, based upon differing signal intensities (peaks and valleys) of each layer. Additionally, this method is tolerant to white noise. The conversion process is equivalent to data averaging 100 times which increases the signal-to-noise ratio of the original data ~ 10 times. As demonstrated in WT mice, this measurement showed high consistency between weekly, repeated measurements.

Data from OCT findings reveal a sequence of events similar to what occurs in humans after episodes of optic neuritis [218, 219]. The acute increases in GCC retinal thickness was found after 2 weeks of EAE, coincident with the onset of motor symptoms. This finding is similar to data from clinical studies showing baseline swelling in 80% of eyes during acute optic neuritis [218]. This increase gave way to significant reductions in GCC retinal thickness, which is typically detectable in humans after ~3 months, once swelling has

resolved [219]. A recent study reported similar trends in GCC thickness among EAE mice, which showed significant GCC swelling 11 days post-immunization, and significant retinal thinning after 4 weeks [220]. While the finding of acute swelling has been inconsistently observed, reductions in GCC thickness has been documented in several previous EAE studies at timepoints >30 days, reminiscent of the long-term retinal thinning in MS patients [220-223]. We interpret these findings to suggest that the EAE model has the same key events as human optic neuritis, albeit at a more rapid pace.

From the ON, DTI measures paralleled findings from human MS in several respects. The findings of increased RAD with concomitant decreases in FA after 4 and 8 weeks are consistent with long-term findings from MS patients, which show similar DTI changes in ON even years after symptoms have resolved [205, 224]. These changes in FA and RAD have also been shown to correspond with visual acuity [225], and discriminate between visual recovery groups after optic neuritis [225]. These results suggest that the degree of alterations in FA and RAD are reliable translational biomarkers of axon loss and may provide useful correlates to functional change.

In contrast, acute reductions of AxD and TR are not universally reported in DTI findings from EAE studies and MS patients. In our study, a significant initial reduction of AxD and TR with a non-significant reduction in RAD were found starting 2 weeks after disease induction. After four weeks this pattern diverged, with continual reduction in AxD, with increases in TR and RAD. Although the biophysical basis behind these

diffusion changes are not clear, reductions in AxD and increases in RAD are thought to be caused by axonal and myelin deficits, respectively [145, 226]. The acute diffusional response within the ON is one of restriction (in AxD, RAD and TR), which may be explained by axonal swelling. Axonal swelling is additionally suggested by the increases in GCC thickness at this timepoint. Later increases in RAD and normalization of TR is likely caused by demyelination [26, 145]. In our previous study using cuprizone-fed mice (a selective oligodendrocye toxin), an early transient reduction of diffusion (in particular prominent reduction of AxD) was also found, which occurred before increases of RAD [143]. In two human studies, an initial reduction of AxD has also been observed as a transient phenomena immediately after the onset of optic neuritis [227, 228] Within acute demyelinating MS lesions, swollen axons with accumulations of APP are often found, thought to be reflection of impaired axonal transport and a biomarker of injury [229 230]. During the earliest stages of inflammation in EAE, axonal homeostasis is likely impaired, leading to accumulations of axonal cargos, swelling, and potentially reductions in AxD detectable by DTI. Indeed, evidence from manganese-enhanced MRI suggests axonal transport is impaired at the onset of optic neuritis in EAE mice [116].

Highly significant, linear relationships were observed between OCT and DTI (FA, AxD and RAD) datasets four and eight weeks after EAE induction. These timepoints correspond to chronic periods of inflammation, during active periods of axon and myelin loss [128]. The relationships between these two biomarkers have been assessed in MS patients, though there is currently a lack of longitudinal data in the literature. Cross-

sectional studies in remote optic neuritis have revealed significant relationships between OCT-derived RNFL thickness and ON FA, AxD and RAD; though the strength of these correlations vary considerably between studies [224, 231, 232]. A recent EAE study found significant relations between ON AxD/RAD changes and GCC thinning, though these alterations were only significant among all mice (EAE + control) after 4 weeks. No significant correlations were observed specifically in the EAE group, though this may be explained by the limited number of mice examined. Our results compliment these data, and illustrate the evolving, linear strength of OCT-DTI correlations during chronic ON degeneration.

Our histological findings bolster results derived from OCT and DTI. In addition to the well characterized axon and myelin loss in the ON [127, 128, 233], we found noticeable structural changes in the EAE mouse retina. This included the reductions in RNFL/GCL layer thickness, which mirrored our OCT results. We did not find significant reductions in IPL thickness, where the RGC dendrites and bipolar cell axon terminals synapse, suggesting that this layer may be more resistant to atrophy. We also measured significant RGC loss, which has been noted in several previous studies [234, 235] and RGC cell body shrinkage, which has been noted in MS patients [236]. The etiology of this morphological change is not entirely clear, but may be related to the shrinkage seen in RGCs during glaucoma and ON crush models [237-240]. Similar to EAE, both feature initial degeneration of the ON, which precedes cell body atrophy. This atrophy is associated with changes in

ion homeostasis and are an early step in the apoptosis cascade, preceding activation of *Bax*[238, 241, 242].

As the soma and axons were simultaneously examined in this study, it provided a unique opportunity to estimate and compare the compartmental variations in neurons affected by EAE. Collectively, both OCT and DTI showed signs of damage as early as 2 weeks after EAE induction (initial thickening of GCC on OCT and initial reduction of AxD on DTI), which was coincident with the beginning of motor deficits in animals. Thus, the somas and axons of RGCs may react during the earliest stages of demyelination. In contrast, at later time points we found a significant discrepancy between the degree of axon loss vs RGC loss. After 8 weeks of EAE, there was an average of >50% of axons lost in the ON, while only ~20% loss of RGCs, suggesting a substantial delay may occur between the loss of axons and subsequent loss of cell bodies [243].

The correlations between *in vivo* biomarkers and neurodegeneration measures derived from axon counts revealed close correlations between both DTI and OCT indices. Our results suggest that among DTI measures, AxD (r = 0.83) and FA (r = 0.74) were the most accurate surrogates, and perform similarly to total GCC thickness (r = 0.72). Our data further suggest that OCT-axon loss correlations can be improved when a pre-established baseline measurement can be utilized (r =0.88).

When extrapolating these finding to clinical studies, there are several important differences to keep in mind between human and mouse eyes. While OCT imaging protocols in humans focus on regions around the fovea, mouse eyes to not contain a fovea. Therefore, OCT alterations in human eyes may present with a larger magnitude of thickness changes relative to axon loss, a topic remaining to be explored [244].

Conclusions

Our findings reveal the correlations between DTI and OCT measures between each other and to the extent of axonal losses in the most commonly used animal model of MS. Comparisons between OCT and DTI datasets reveal significant correlations between OCT-derived thinning and DTI-derived AxD, RAD and FA after 4 and 8 weeks of EAE. Measures derived from OCT and DTI both show high degrees of accuracy in detecting the extent of axon losses in the ON after 8 weeks of EAE.

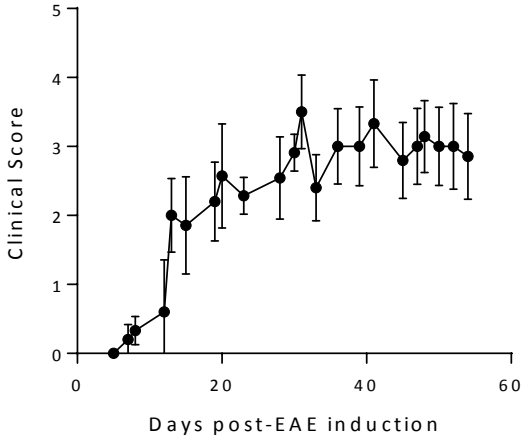

Figure 3.1 EAE mice clinical scores EAE mice began to show symptoms 10-12 days after disease induction. The means and s.e.m. are shown from all EAE mice (n=11)

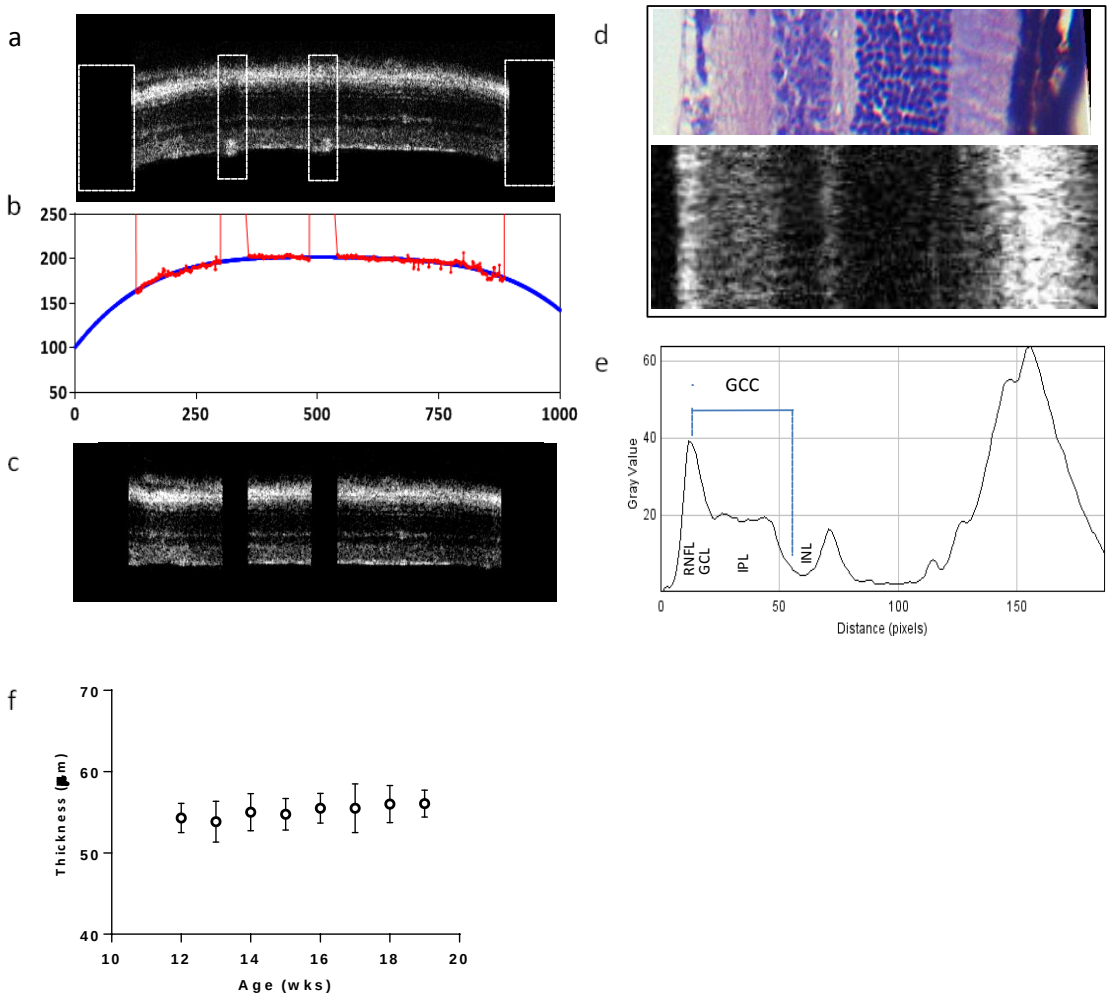

Figure 3.2 OCT Processing and Analysis a. Selected B scans were preprocessed by manually removing segments containing vessels along the RNFL surface and trimming edges (white boxes) to aid subsequent processing steps. **b.** Processed B scans were analyzed using MATLAB which fit the surface of the RNFL/vitrius border (red) with a quadratic curve (blue). This curve was used to flatten the retina by shifting individual A scans to a common reference level (**c**). **d.** Portion of an H&E stained retina along with a section of flattened retina (rotated 90˚) showing the correspondence between individual layers. **e.** Profile plot showing the average grey values of individual layers in the retina. The measurement of the GCC is shown in blue, extending from the peak RNFL value to the middle boundary between IPL and underlying INL. **f.** GCC thickness measures (mean ± SD) from 3 untreated, WT mice between 12-19 weeks of age.

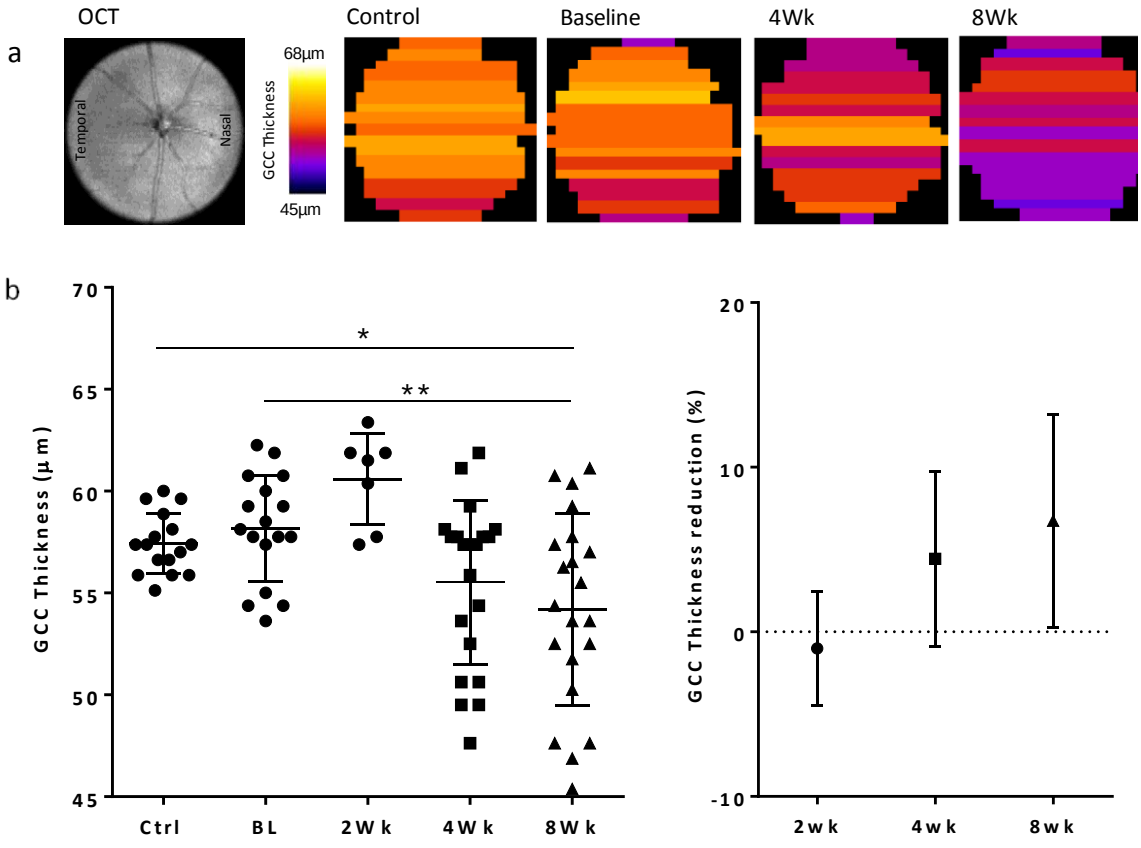

Figure 3.3 GCC thickness measurements in EAE mice a. En face OCT image and corresponding data maps (N=17-18 B-scans/retina) showing the GCC thickness across the retina in a control and EAE mouse. These maps illustrate the reductions in GCC thickness for a single mouse eye during EAE after 4 and 8 weeks. **b.** Total retinal thickness from GCC layers in control, baseline and EAE mice. Retinal thicknesses were significantly reduced after 8 weeks of EAE. Right, individual data plotted as percent reduction relative to baseline measurements. *, $p<0.05$; **, $p<0.01$

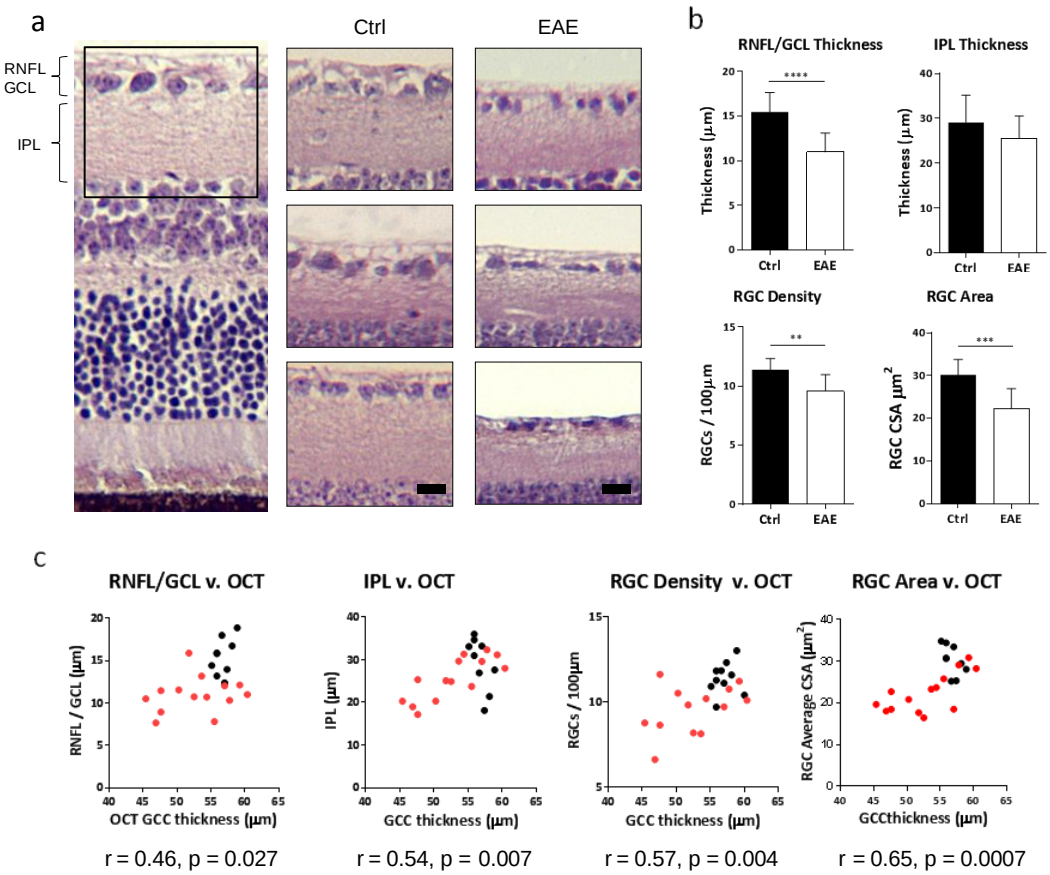

Figure 3.4 Retinal histology from EAE mice a. H&E processed retinal section showing all layers. Right, zoomed sections from control and EAE retinas showing the RNFL, GCL and IPL layers (GCC). Black scale bars show 10µm. **b.** Quantification of Retinal histology reveals significant reductions in both RNFL/GCL but not IPL thicknesses. RGC density and cross sectional area (CSA) is also reduced in EAE retinas. Bottom, correlation between OCT-measured retinal GCC thickness and histology measured thicknesses of individual layers, RGC density and CSA. **, p<0.01; ***, p<0.001; ****, p<0.0001

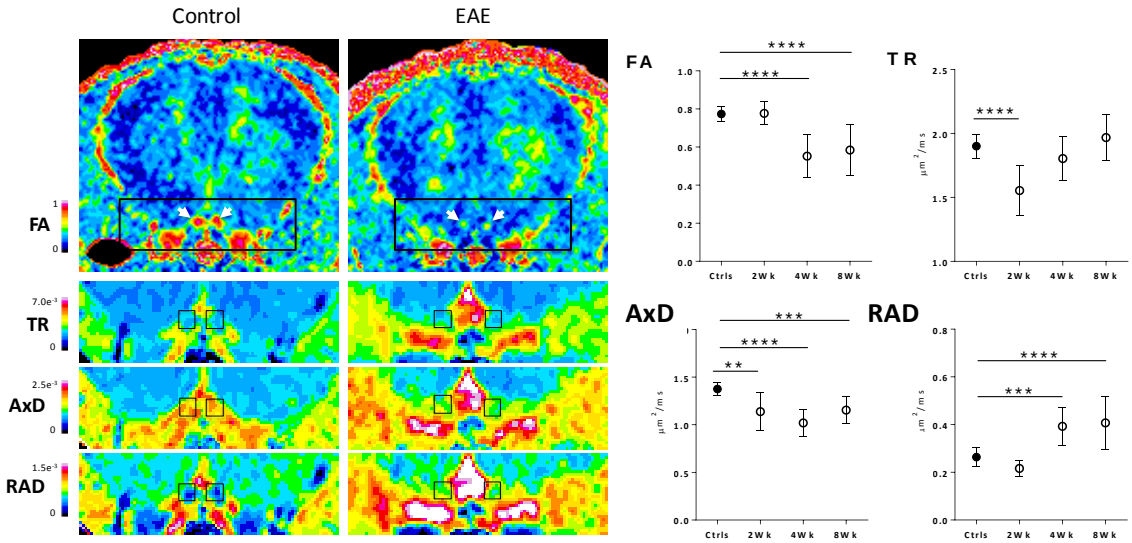

Figure 3.5 Optic Nerve DTI measurements Left, pseudocolored representative images showing the diffusion changes in 8 week EAE mice relative to controls. Left and Right optic nerves are shown in coronal section and indicated by white arrows in FA maps. Diffusion maps for TR, AxD and RAD are shown in enlarged views below; ON ROIs are shown in black boxes. Right, quantified ON diffusion changes across the time-course. **, p<0.01, ***, p<0.001, ****, p<0.0001

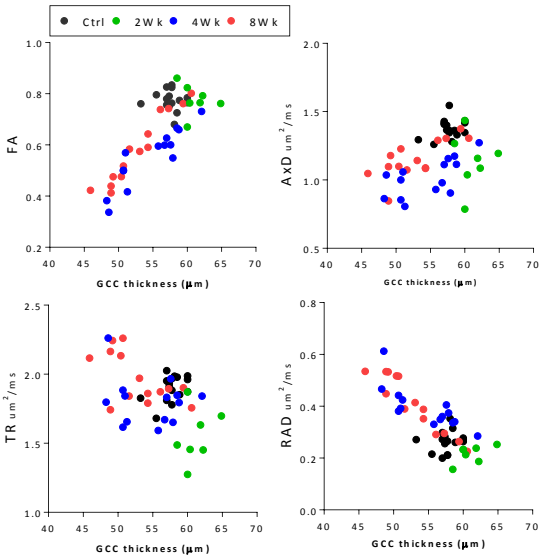

	FA		AxD	
	Pearson r	*p* value	Pearson r	*p* value
All Mice	**0.8293**	**<0.0001**	**0.4669**	**0.0006**
Ctrl	-0.09596	0.7237	0.3267	0.2169
2Wk	-0.258	0.5764	-0.01246	0.9789
4Wk	**0.9032**	**<0.0001**	**0.6526**	**0.0114**
8Wk	**0.9686**	**<0.0001**	**0.7364**	**0.0027**

	TR		RAD	
	Pearson r	*p* value	Pearson r	*p* value
All Mice	**-0.4449**	**0.0011**	**-0.8303**	**<0.0001**
Ctrl	0.4409	0.0874	0.1926	0.4749
2Wk	0.2811	0.5414	0.5766	0.1754
4Wk	-0.2025	0.4875	**-0.7821**	**0.0009**
8Wk	**-0.584**	**0.0283**	**-0.9423**	**<0.0001**

Figure 3.6 Relationship between ON DTI measures and OCT-derived GCC measurements Left, scatter plots show the relationships between ON measurements and individual DTI metrics. Right, Pearson r correlations are shown for groups at individual timepoints. Significant relationships ($p<0.05$) shown in bold.

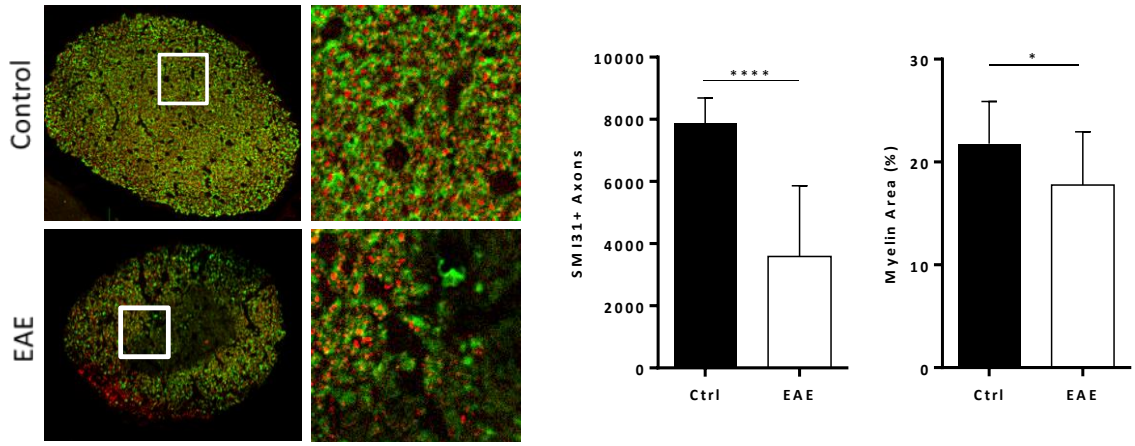

Figure 3.7 Axon and myelin loss during EAE Left, axons and myelin labeled using SMI-31 (red) and MBP (green). EAE optic nerves show widespread demyelination and axonal loss, relative to controls. Right, quantification of axon and myelin loss. *, $p<0.05$; ****, $p<0.0001$

	FA		AxD		TR	
	r	*p* value	r	*p* value	r	*p* value
4Wk	0.6758	0.008	0.5881	0.027	-0.04963	0.8662
8Wk	0.7365	0.0027	0.8343	0.0002	-0.08213	0.7801

	RAD		GCC thickness		GCC thinning	
	r	*p* value	r	*p* value	r	*p* value
4Wk	-0.5657	0.035	0.5163	0.0587	0.7437	0.0023
8Wk	-0.595	0.0248	0.7283	0.0031	0.8793	<0.0001

Figure 3.8 Axon numbers correlated to noninvasive imaging biomarkers. DTI measures (FA, AxD, TR, RAD) and OCT derived-measures (GCC thickness and GCC thinning) and their correlation to histology-measured axon counts. Measures from 4 and 8 weeks after induction of EAE.

Chapter IV:

Axonal transport impairment and its relationship with Diffusion Tensor Imaging metrics: A Manganese Enhanced MRI (MEMRI) study in p301L tau mice

Abstract

Several prominent neurodegenerative disorders, including Alzheimer's disease, display deficits in axonal transport, suggesting that axonal transport may play an important role in disease pathophysiology. Identifying biomarkers of axonal transport disruption may be crucial to study disease onset and progress. However, there are currently no clinically available methods to assess axonal transport rate noninvasively. In this study, we tested whether axonal transport, assessed using manganese-enhanced MRI (MEMRI), could be related to alterations in diffusion tensor (DTI) metrics in the visual system aged p301L tau mice. Derived from MEMRI, the manganese optic nerve accumulation rate (ONAR) and superior colliculus accumulation rate (SCAR) were quantified and correlated with DTI indices in optic nerves and tracts. Immunohistochemical labeling of axons (SMI-31), myelin (MBP), and phospho-tau (AT8) were examined in tissues after imaging. ONAR revealed significant ($p<0.05$) linear correlation with optic nerve trace diffusion (TR) $r = 0.786$ and radial diffusion (RAD) $r = 0.711$. Histology of the optic nerve revealed that impaired axonal transport was associated with reductions in myelin content but not axonal / tubulin density or phospho-tau pathology within the retina or optic nerve. Myelin content also correlated strongly with DTI metrics TR and RAD. These results suggest that diffusion tensor metrics may be sensitive to underlying structural alterations within white matter that can signal differing rates of axonal transport.

Introduction

Deficits in axonal transport are hypothesized to occur in a diverse set of neurodegenerative diseases, including Alzheimer's Disease (AD) [85]. These impairments may begin very early in the disease process; data from AD mouse models have shown evidence of transport impairments and axonal swellings that precede overt brain pathology [245-247]. This has led to the suggestion that dysregulation of transport may be integral to disease pathophysiology[99].

Several techniques can be used to study axonal transport, including live imaging cell culture [95] and drosophila models [248], injection/tracing of radiolabeled amino acids [249] and Manganese-enhanced MRI (MEMRI) [91-93]. Of these, MEMRI has the unique ability to be used in mammalian models, longitudinally *in vivo*. MEMRI takes advantage of the chemical properties of Manganese (Mn^{2+}) as a calcium analogue. Mn^{2+} is taken up through L-type voltage-gated Ca^{2+} channels in neurons, packaged into vesicles and transported down the axon using fast axonal transport[250-252]. As a paramagnetic ion, Mn^{2+} shortens T1 relaxation time and is visible as a hyperintensity in axon tracts using T1 weighted imaging (T1WI). Serially imaging these axon tracts and their targets allows for dynamic measurements of vesicle movement and axonal transport. MEMRI can be applied noninvasively by using the visual system, after Mn^{2+} application to the eye [183], or in the olfactory system after intranasal gavage [253]. MEMRI has been used as a tool in several animal models of AD to detect alterations in axonal transport [91, 92, 254]. These

studies have helped to establish axonal transport impairments as a feature of AD. Transport deficits have been detected in APP-overexpressing models [254], mixed APP/mutant-tau models [93] and pure tauopathy models [91]. Deficits appear to be age-dependent in tau models, appearing at 6 months of age.

During AD, transport deficits have been heavily linked to tau. Indeed, *in vitro* evidence suggests that Aβ-induced axonal transport deficits require WT tau [95, 96]. During basal conditions, tau is predominantly located in the axon, where it acts as a microtubule stabilizing protein. In AD, tau becomes abnormally hyperphosphorylated, detaches from microtubules and aggregates within neurons, primarily within the somatodendritic compartment. Loss of tau function or deleterious gain-of-function may destabilize axonal microtubule networks, which would compromise axonal transport. In support of this, tau models exhibit increased turnover of microtubules, which are typically arrayed in stable networks in WT mice [103]. Studies using microtuble-stabilizing drugs have shown reductions in microtubule turnover [103] as well as increases in axonal transport velocity in tau models [106, 109].

Transport deficits in AD have also been linked to the appearance of swollen axons [247, 255, 256]. These swollen 'dystrophic' axons are frequently found in close association with amyloid plaques [257]. The swellings consist of accumulations of microtubule-associated proteins, organelles and vesicles [247]. Studies have linked transport deficits and axonal

swellings to the neuropathological changes that occur during AD [255, 256] and in AD mouse models [247, 258].

Axonal swellings or disruption to microtubule networks may be detectable using a technique sensitive to microstuctural change, such as Diffusion Tensor Imaging (DTI). Several studies have examined white matter alterations in tauopathy models. A study by Febo et. al.[116] revealed age-related change in several white matter tracts of rTg4510 mice, detectable as reductions in FA and increases in RAD at 8 months. Similar changes were found by Wells et. al. in the corpus callosum of rTg4510 mice at 8.5 months[120]. In both cases, aging and the onset of tau pathology were linked to alterations in DTI measurements within white matter. While DTI studies have examined microstructural changes in tau models, there have been no examinations of the connection between microstructural change and axonal transport function.

In this experiment, we hypothesized that disruption of structural elements within axons in a tauopathy model could affect both axonal transport function and DTI metrics. Our goal was to correlate changes in axonal transport to DTI in order to determine if diffusion signal could be used as a surrogate marker to infer differences in transport from white matter tracts noninvasively.

Materials and Methods

This study was conducted in accordance with National Institutes of Health guidelines and Statement for the Use of Animals in Ophthalmic and Visual Research, and was approved by the Institutional Animal Care and Use Committee at Loma Linda University.

Animal Preparation

Nine, 11-month old homozygous p301L tau mice were used in this experiment. p301L mice express the mutant variation (4R0N) associated with frontotemporal dementia and parkinsonism linked to chromosome 17. Pathological characteristics are strongly age-dependent and tau aggregates begin to appear in the brain at ~ 5 months of age in homozygous mice [61].

DTI Acquisition

Mice were anesthetized by 1.5% isoflurane/oxygen using an isoflurane vaporizer (Vet Equip, Pleasanton, CA). Body temperature was maintained at 37C using a warm water heating pad. Scans were collected using a Bruker 11.7T BioSpec small animal MRI instrument. The acquisition protocol used a slice thickness 0.5 mm, FOV of 1.5 cm x 1.5 cm and matrix 128 x 128 (zero filling to 256 x 256), TR 2.5 s, TE 29 ms, Δ 20 ms, δ 3 ms, and a 21-direction diffusion scheme with b-values of 0 and 0.85 ms/μm^2 [259]. Using FSL, raw DWIs were corrected for eddy current and motion distortions (http://fsl.fmrib.ox.ax.uk/fsl/). Corrected scans were then imported into 3D Slicer, where eigenvalues derived from the diffusion tensor were used to calculate axial diffusion

(AxD), trace of diffusion (TR), radial diffusion (RAD) and Fractional anisotropy (FA), defined by the following equations:

$$AxD = \lambda_1 \quad (1)$$

$$TR = \lambda_1 + \lambda_2 + \lambda_3 \quad (2)$$

$$RAD = (\lambda_2 + \lambda_3) * (1/2) \quad (3)$$

$$FA = \sqrt{\frac{3}{2}} \frac{\sqrt{(\lambda_1 - ADC)^2 + (\lambda_2 - ADC)^2 + (\lambda_3 - ADC)^2}}{\sqrt{\lambda_1^2 + \lambda_2^2 + \lambda_3^2}} \quad (4)$$

DTI measurements were made by manually selecting regions of interest (ROIs). The high anisotropy and low radial diffusion of the ON provided contrast against neighboring CSF and grey matter to accurately define the region, consisting of 25-30 central voxels within each nerve in 3 serial slices (Figure 4.1A).

MEMRI Procedure

Mice were anesthetized by 1.5% isoflurane/oxygen using a isoflurane vaporizer (Vetequip, Pleasanton, CA). 5ul of $MnCl_2$ was administered to the surface of both eyes for each mouse. After 1 hour, remaining solution was carefully removed using Kimwipes. At regular intervals, mice were anesthetized and scanned using T1W protocol (TR = 0.5s ,TE =14.5ms) and T2 Rapid Acquisition with Refocused Echoes (RARE) protocol (TR = 1s, echo train = 4, effective TE 28ms), with identical resolution and spatial orientation of our DTI protocol. During both loading and scanning procedures, body temperature was maintained at 37C.

MEMRI Quantification

ON accumulation rate (ONAR)

Regions of interest (ROIs) were selected on T2WI maps from prechiasmatic optic nerves (Bregma +1.2) and superior colliculus (Bregma-2.9 to -4.5) from both right and left hemispheres. Manually defined ROIs were then transferred to co-registered T1W images for measurement. Signal intensity of Mn^{2+} affected regions was normalized by reference regions (average intensity from striatum), which showed no significant group-level change over the course of the experiment.

For each optic nerve, we fit the Mn^{2+} enhancement curve during 3-14hrs after Mn^{2+} loading with a second order quadratic equation. Based on the derived quadratic equation, a tangent line was fit at the midpoint of the signal growth period at 7 hours (Figure 4.2B). The derived slope is termed the **ON accumulation rate (ONAR).**

SC accumulation rate (SCAR)

We first defined the region of the SC based on anatomical landmarks. The voxels with enhancement larger than mean+2 SD over that of reference regions were counted as Enhanced Voxels. The number of Enhanced Voxels was found to gradually increase over 22 hrs after the Mn^{2+} loading in the eye, which was then fit using a regression line. The slope of this regression line was termed the **SC accumulation rate (SCAR).**

Immunohistochemisty Procedures

All mice from the experiment were sacrificed after the final time-point. Mice were perfused with PBS followed by 4% paraformaldehyde. Coronal sections 3mm thick were obtained from the ON (Bregma +2 to -1) and paraffin embedded. Thin sections (5um) from this block were cut using a microtome. Sections were deparaffinized, rehydrated, permeabilized in 0.3% Triton, boiled in citrate buffer and blocked using 3% normal goat serum. ONs were stained using an anti-phospho neurofilament antibody to label healthy axons (SMI-31, Covance, 1:1000), Myelin, (MBP, Zymed, 1:1000), βIII tubulin (Abcam, 1:1000) and phospho-tau (AT8, ThermoFisher, 1:400). After incubation overnight in primary antibodies, sections were labeled with appropriate secondary antibodies and coverslipped with Prolong Gold. Slides were imaged with a combination fluorescence / brightfield microscope at 40x.

Tissue Analysis

Images captured at 40x were analyzed within ImageJ. Axonal / tubulin density and myelin area in the ON were assessed by a blinded observer. Images were individually thresholded to capture signal within axons or myelin while excluding background signal. Density of SMI-31/tubulin+ axons within each ON were calculated as number per $100um^2$. Myelin was quantified as a percentage of MBP+ signal / $100um^2$.

Statistical Analysis

All statistical calculations were carried out in Prism 6.0. Centered, second order quadratic equations were used to fit the enhancement profiles of individual ONs, while linear regression was performed to fit data from the SC. Correlations between MEMRI/DTI and MEMRI/histology were tested using a Pearson's correlation coefficient. All *p* values below $p<0.05$ were considered statistically significant.

Results

DTI Results

A summary of our DTI results from the ON and OT is shown in Figure 4.1 Our data shows the degree of natural variation across all diffusion metrics (FA, TR, AxD and RAD) within this cohort of p301L mice.

Mn^{2+} accumulation rate in the optic nerve and relationship with ON DTI measures

Two overlapping MEMRI time-courses were run, in order to define the average enhancement curve over a 22 hour period. Six mice (N=12 eyes/ONs) were assessed at baseline, 3, 7, 11 and 14 hours after Mn^{2+} exposure. Three additional mice (N=6 eyes/ONs) were assessed at baseline, 10, 14, 18 and 22 hours. These datasets reveal that enhancement within the ON ROI follows a sinusoidal curve, rising sharply between 3 to 14 hours before leveling off at a steady state at around 14 hours (Figure 4.2). Estimates of ONAR were made from data acquired within the signal growth period (3-14 hours). Each enhancement profile was fit using a second-order quadratic equation (average $r^2= 0.98$).

Comparisons between ONAR and diffusion metrics revealed two significant correlations. The rate varied as a function of total diffusion magnitude (TR, r=0.786, p=0.0025) and RAD (r=0.711, p=0.0096). Interestingly, these correlations were both positively associated. Higher degrees of total and radial diffusion predicted faster rates of Mn^{2+} accumulation (Figure 4.3). No significant relationships were found between FA and accumulation rate, though there was a negative trend between higher FA values and lower rates of accumulation.

Correlations between the extent of normalized intensity within the ON and DTI measures at single time-points were also examined (Table 4.4). At early timepoints (0-3 hours) we found no significant relationships between DTI measures and ON normalized intensity. At 7, 11 and 14 hours, however, intensity was significantly related to TR measurements. Intensity significantly correlated to AxD only at 7 hours, while RAD correlated significantly at both 11 and 14 hours.

Mn^{2+} accumulation rate in the SC and relation to DTI measurements

Group data from our MEMRI time-course between 3-22 hours revealed a linear profile of Mn^{2+} signal enhancement in the SC (Figure 4.5, average r^2= 0.956). This linear profile suggests that regional enhancement builds in the SC as Mn^{2+} accumulates at terminal synapses. Assessment of SCAR was made between 3-14 hours. Averaged ON and contra-lateral OT DTI measurements were compared to contra-lateral SCAR (Figure 4.6). No

significant relationships were found, though we observed trends between SCAR and FA (r=-0.507, p=0.093), TR (r=0.516, p=0.086) and RAD (r=0.541, p=-0.069)

Optic nerve histology

Markers for healthy axons (SMI-31), myelin (MBP), microtubules (β3 tubulin), and phospho-tau (AT8) were examined to investigate underlying structural factors that could explain variability in axonal loading and transport. We found a wide range of phospho-tau staining within the ON and retina, including regions with little to no staining and regions with punctate axonal staining and diffuse cell body labeling (Figure 4.7). However, we found no connection between the extent, density or variety of AT8 staining patterns in the retina or ON and measures of axonal transport. Labeling axons with SMI-31 revealed no significant associations between axonal density and measures of axonal transport. We did observe swollen axons in several optic nerves, though average axon size did not correlate with axonal transport (data not shown). Tubulin staining was varied between ONs, with no significant associations between density and transport properties. However, Myelin content was significantly correlated to ONAR (r = 0.8725, p =0.0002) but not SCAR (r = 0.5412, p = 0.0692). Nerves with slower transport had less total myelin, as well as a more 'disordered' appearance, with fewer sheaths with a characteristic round shape (Figure 4.8B). These differences in myelin between ONs also correlated with our DTI data (Figure 4.8C). We found significant positive correlations between TR / RAD (r = 0.74, p = 0.0052; r = 0.75, p = 0.049) and total myelin content.

Discussion

This study reveals a novel connection between the diffusional properties of nerves and their axonal transport function in a tauopathy model. Variation in ON DTI measures TR and RAD were significantly correlated to both Mn^{2+} accumulation rate in the ON (Figure 4.3). Impairment in transport function was not attributable to axonal numbers or βIII-tubulin loss, but did correspond to reductions in myelin content within ONs. Differences in myelin content were significantly associated with both TR and RAD . Importantly, our results predict that nerves with transport impairment may be identifiable using noninvasive diffusion MRI.

Rates of Mn^{2+} accumulation in axon tracts and terminal regions are thought to reflect the speed and efficiency of the axonal transport system[260-262]. In this study, we measured Mn^{2+} accumulation rates in both the optic nerve and in the superior colliculus over a 14 hour period. While Mn^{2+} accumulation was quantified using normalized intensity in the ON, a voxel-based intensity cutoff was utilized in the SC. This approach minimized the effects of ROI size variability on our measurements. The timepoints were chosen in this experiment to reveal the initial growth phase of Mn^{2+} signal in the ON and OT, which reflect the ongoing process of axonal transport.

Correlations between DTI measures and transport efficiency revealed surprising positive trends between AxD, TR and RAD measures with faster rates of axonal transport. These data indicate that diffusional restriction (low TR / AxD / RAD) is a marker of axonal

transport impairment. Restricted diffusion in white matter has been found in several models during axonal degeneration due to retinal ischemia [27], Experimental Autoimmune Encephalomyelitis [263] or Traumatic Brain Injury (TBI) [264, 265]. Typically, these reductions in TR have been ascribed primarily to diminished AxD. The underlying cause of low AxD during axonal injury is hypothesized to be caused by axonal beading or swelling [266]. Our DTI results differ from published literature on axonal degeneration in several respects, however. In ONs with compromised transport, we found reductions in AxD as well as RAD. The cause of the reduction in RAD is not clear, though our data suggests it may be related to alterations in the myelin sheath and corresponding restriction of extracellular space. In addition, these changes were accompanied by a persistent trend between high FA values and lower rates of transport/accumulation. In most cases of overt neurodegeneration, FA is reduced due to the loss of structural elements (axons, myelin sheaths) that create anisotropic diffusion [25, 267], so higher FA is typically associated with healthy conditions. Our results suggest that elevated FA values may not always reflect healthy white matter. This pattern of diffusional change (elevated FA, reduced TR, AxD and RAD in white matter) has been found in several studies after head trauma [268-270], potentially indicating the presence of axonal transport impairment after these injuries.

In vivo imaging vs histology

Our histology data revealed evidence of a structural correlate to variations in transport efficiency and our DTI data. While we did not find correlations between axonal or β3-tubulin densities in the ON and axonal transport, we did find evidence of myelin

alterations that corresponded to stunted transport (Figure 4.8). This was detected in our tissue as a lower percentage of myelin within the optic nerve with less uniformity of myelin sheath size and shape compared with ONs with faster transport. These data may be explained by work linking myelin integrity and bioenergetic support of axons to the process of fast axonal transport [271, 272]. Loss or dysfunction of myelin may impair metabolic coupling between axons and oligodendrocytes, resulting in shortages of axonal ATP required for fast axonal transport [273]. These differences in myelin content between ONs may help explain the DTI results as well. Previous studies in myelin-loss models, including cuprizone-fed mice [143, 145] and shiverer mice [26] have highlighted the sensitivity of DTI parameters TR and RAD to myelin content. However, in contrast to our results, myelin loss is typically associated with elevated TR and RAD. We speculate that the abnormal 'disordered' morphology of myelin sheaths observed in ONs with slow axonal transport may account for this difference. Loss of structural coherence of the myelin sheath may be hindering diffusion across the plane of the ON, reducing both total and radial diffusion.

Surprisingly, we did not find clear relationships between the presence of hyperphosphorylated tau in the ON or retina and axonal transport properties (Figure 4.7). ONs and retinas with tau aggregates did not show obvious deficits in axonal transport. This findings may be due to several factors, including our analysis method. Using histology to detect pathogenic tau species is insensitive to soluble forms. The underlying species of tau responsible for transport deficits is controversial, and may involve

aggregated, filamentous forms [88] or soluble forms [274]. Further work is required to fully elucidate how various tau species may influence the process of axonal transport.

Myelin disruption

Our data suggests that myelin disruption may play a key role in producing both axonal transport deficiencies and diffusional restriction in the visual system. In the JNPL3 p301L tau mouse, tau expression is driven by the prion promoter [61]. This leads to primarily neuronal expression, but also p301L tau present in oligodendrocytes [275]. A previous study examining this model found widespread evidence of myelin disruption (malformed or uncompacted myelin sheaths) in the stratum lacunosum moleculare [276]. Experimental work using p301L tau expression restricted to oligodendrocytes revealed structural disruption of the myelin sheath as well as impairments in axonal transport [277] . These studies suggest that tau in our model may be directly involved in the observed myelin abnormalities, which may be causing alterations in axonal transport.

Conclusion

In summary, our results demonstrate a novel connection between DTI-detectable microstuctural alterations, axonal transport function and myelin in a tauopathy model. We consider this work to be preliminary evidence that requires further study, in order to determine if these results are applicable to other models or specific conditions after white matter injury.

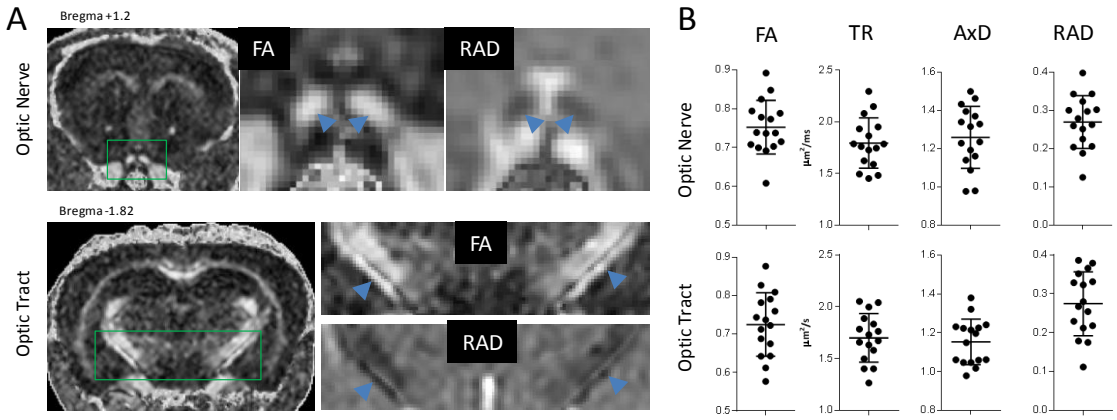

Figure 4.1 DTI properties in ON and OT A. Optic Nerve and Optic Tract ROIs are shown in coronal section (left) and in adjacent magnified FA and RAD maps. ONs and OTs are marked by blue arrows and are easily identifiable by both high FA and low RAD relative to adjacent CSF and brain tissue. B. Analysis of ON and OT DTI reveals the natural variability in microstructural properties between mice in our 11-month p301L cohort.

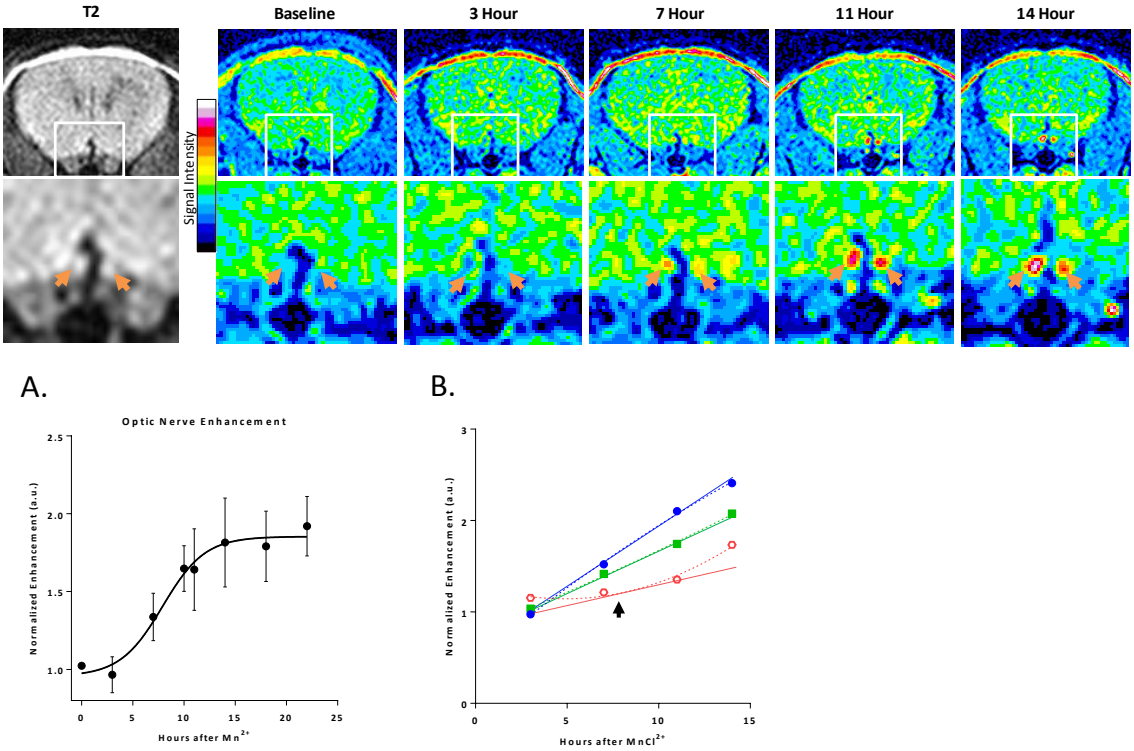

Figure 4.2 Manganese enhancement in ON Top, Mn^{2+} enhancement within the ON between 0-14 hours during MEMRI time-course. T2W images (top left) help identify ON location before visible enhancement. T1W images are pseudocolored to show changes in ON enhancement profile across time. ONs are marked with orange arrows in magnified views. Bottom (A), average enhancement for all ONs is plotted. Enhancement follows a sinusoidal curve, increasing sharply between 3-14 hours before reaching a steady state. B. Graphed profile of three optic nerves with fast (blue) intermediate (green) and slow (red) rates of enhancement. Dotted lines show the nonlinear fit of each profile and the tangent line (solid line) fitted to each curve at 7.9 hours (at arrow) from which slope was derived.

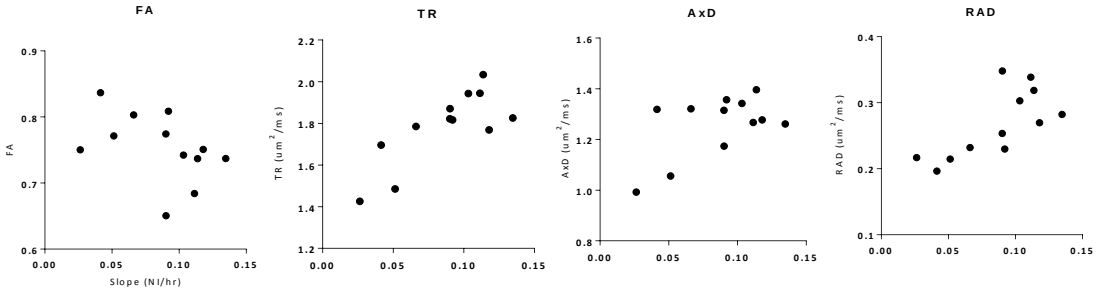

r = -0.444, p = 0.148 **r = 0.786, p = 0.0025** r = 0.568, p = 0.054 **r = 0.711, p = 0.0096**

Figure 4.3 Scatter plots showing the correlation between ONAR (normalized intensity [NI]/hr) and DTI metrics. Accumulation rate correlated significantly with both total diffusion magnitude (TR) and radial diffusion (RAD).

Timepoint		FA	TR	AxD	RAD
0Hr	Pearson's r	0.494	0.087	0.323	-0.292
n=12	p value	0.2444	0.462	0.305	0.357
3Hr	Pearson's r	0.529	-0.135	0.161	-0.463
n=12	p value	0.28	0.676	0.618	0.129
7Hr	Pearson's r	-0.207	**0.835**	**0.754**	0.569
n=12	p value	0.518	**0.0007**	**0.0046**	0.0534
11Hr	Pearson's r	-0.465	**0.667**	0.443	**0.66**
n=12	p value	0.216	**0.0179**	0.149	**0.0194**
14Hr	Pearson's r	-0.368	**0.556**	0.394	**0.522**
n=18	p value	0.133	**0.0167**	0.106	**0.0262**

Table 4.4 Correlations between DTI measures and ON Mn2+ enhancement at individual timepoints. Significant correlations ($p<0.05$) shown in bold.

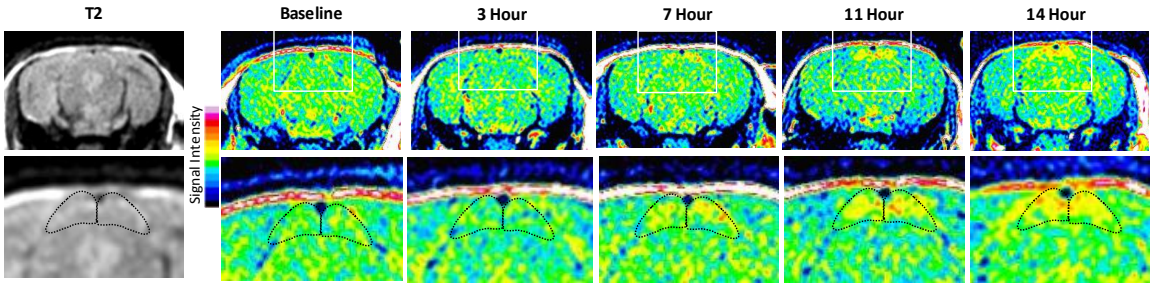

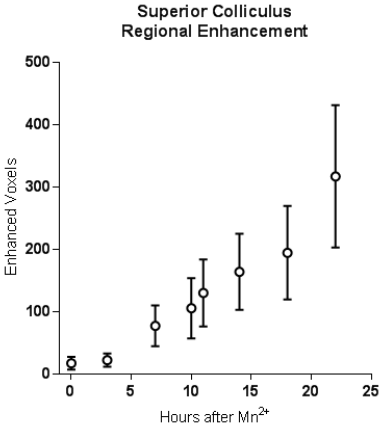

Figure 4.5 Top, Mn^{2+} enhancement within the SC between 0-14 hours during MEMRI time-course. Enhancement above baseline is visible starting at 7 hours. SC ROIs are shown bounded by black dotted lines. Right, number of enhanced voxels within the ROI rises steadily between 3-22 hours. Enhancement across time follows a linear profile.

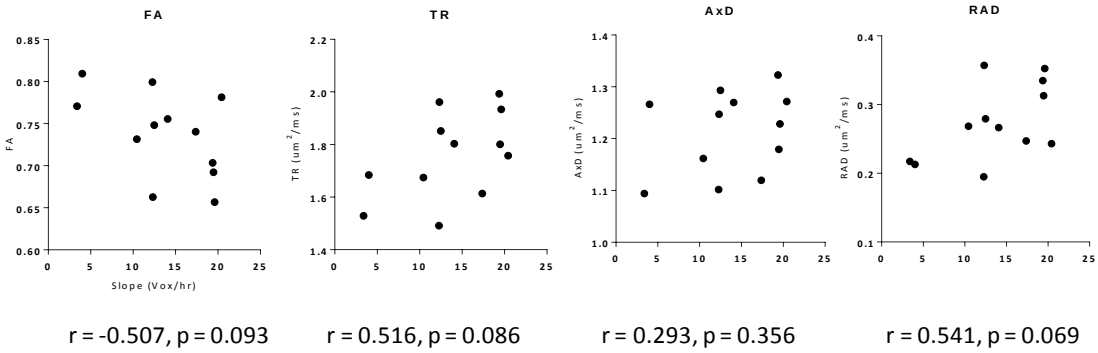

Figure 4.6 Scatter plots showing the correlation between SCAR and averaged ON/OT DTI metrics.

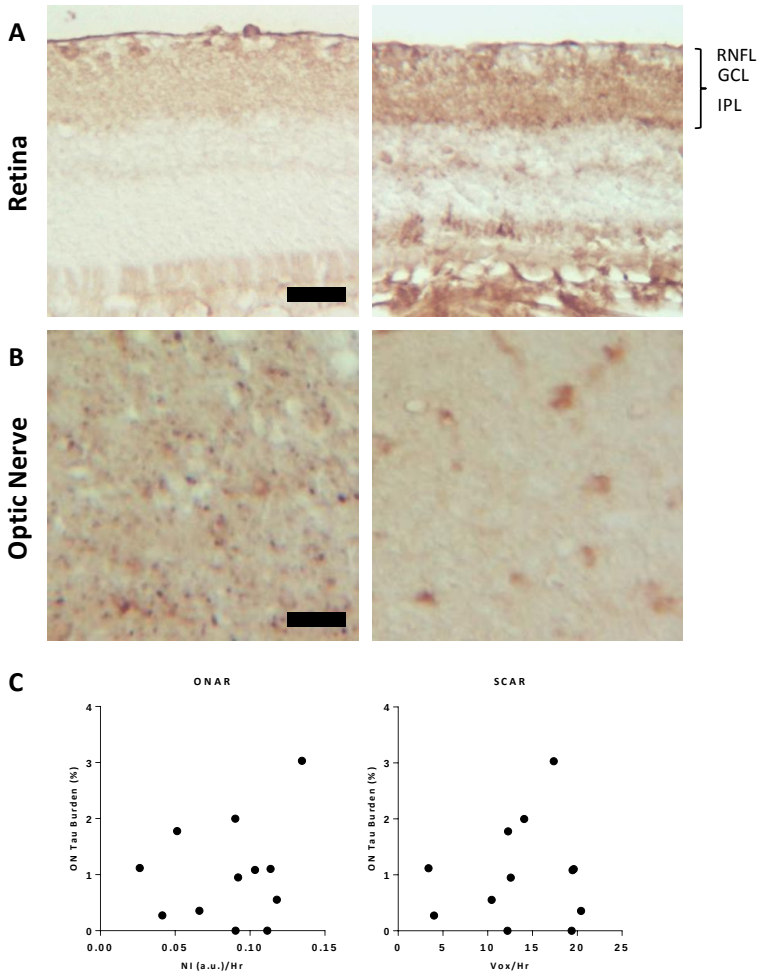

Figure 4.7 Tau pathology in the ON and Retina Phospho-tau staining using the AT8 antibody revealed tau pathology within the Retina (A) and Optic Nerve (B). Pathology within the retina appeared within the Retinal Nerve Fiber Layer (RNFL), Ganglion Cell Layer (GCL) and Inner Plexiform Layer (IPL) layers, containing Ganglion cells. Phospho-tau within the optic nerve (B) occured with either a punctate (left) or diffuse (right) appearance. Degree of tau pathology within the ON did not correlate significantly with measured ONAR/SCAR (C). Scale bars = 20μm

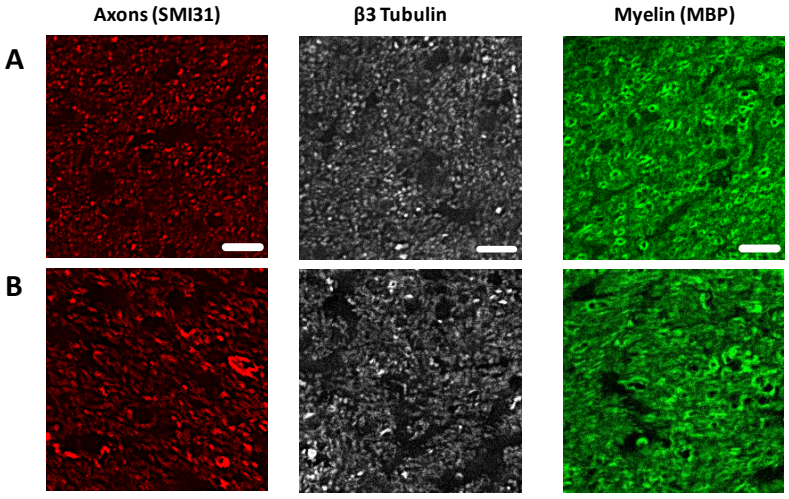

C

Correlation between ON histology measures and Axonal transport / DTI

		Axonal Density	βIII Tubulin Density	Myelin Area
ONAR	Pearson's r	0.3257	0.3472	**0.8725**
	p value	0.3015	0.2688	**0.0002**
SCAR	Pearson's r	0.447	0.3939	0.5412
	p value	0.1451	0.2052	0.0692
FA	Pearson's r	0.3314	0.01897	-0.3759
	p value	0.2926	0.9533	0.2284
TR	Pearson's r	0.2412	0.338	**0.7478**
	p value	0.4501	0.2826	**0.0052**
AxD	Pearson's r	0.374	0.329	0.5039
	p value	0.231	0.295	0.0949
RAD	Pearson's r	-0.058	0.1943	**0.7508**
	p value	0.857	0.545	**0.0049**

Figure 4.8 ON axon, β3 tubulin and Myelin staining. Staining for axons, tubulin and myelin in ONs with faster (A) and slower (B) rates of axonal transport. Correlations between axonal density, tubulin density, myelin area and ONAR/SCAR are shown in (C). Axonal and tubulin staining revealed no significant relationships between density and either transport measures or DTI values. ON myelin content was related to both ONAR as well as TR and RAD. Scale bars = 5um

Chapter V:

Retrograde axonal degeneration induced by Aβ in a mouse model of tauopathy

Abstract

Cognitive decline during Alzheimer's Disease (AD) is coincident with deficits in structural and functional connectivity within vulnerable brain networks. This finding may be explained by evolving white matter tract damage, which has been studied extensively with the use of clinically available Diffusion Tensor Imaging (DTI). Notably, many of the white matter pathways most heavily impacted during disease project into and out of regions, such as the medial temporal lobe (MTL) which harbor significant tau pathology burdens. However, it remains relatively unclear whether this pathology may directly influence white matter integrity. We hypothesized that tau pathology induced by Aβ could initiate an axonal degeneration process, potentially through retrograde mechanisms, leading to altered microstructural properties within vulnerable axon tracts. To test this hypothesis, we utilized the visual system of transgenic p301L tau mice as a model, examining Retinal Ganglion Cell axons, which project from the Retina into the Optic Nerve (ON), Tract (OT) and synapse in the Lateral Geniculate Nucleus (LGN). Microstructural properties of this pathway were examined longitudinally by DTI after injection of Aβ into the LGN. In parallel, we tested whether micotubule-stabilizing compound Epothilone D (EpoD) could ameliorate damage. Our results are suggestive of a retrograde degeneration process, with early DTI changes manifesting in the OT after one month (reductions in axial diffusion, AxD) preceding later alterations in the ON after two months (Reductions in fractional anisotropy, FA and AxD). Histology data revealed

loss of synapses, axons and cell bodies resulting from the injection. EpoD treatment was sufficient to prevent axon and cell loss, as well as reduce total tau pathology burden in the brain (>80% reduction measured in the hippocampus). Our data further suggest that EpoD may mediate its protective effect by blocking acute Aβ-induced tau phosphorylation at the level of the post-synapse in the LGN. This study demonstrates the importance of tau pathology to disruptions in white matter connectivity and may highlight a potential therapeutic avenue to block axon loss during disease.

Introduction

Alzheimer's Disease (AD) is an age-related devastating neurodegenerative disease characterized by progressive declines in learning, memory, and executive function. These cognitive deficits likely arise in part due to dysfunction within brain networks, whose connectivity is enabled by axon rich white matter (WM) tracts. Indeed, WM abnormalities have been observed early in the course of the disease. Loss of WM microstructural integrity, detected by Diffusion Tensor Imaging (DTI), has been reported in patients with mild cognitive impairment (MCI) and AD [278, 279]. Results suggest that several, specific WM tracts have altered patterns of diffusion during disease, relative to cognitively healthy controls [167, 280]. The magnitude of DTI WM alterations correlates with cognitive performance, making WM damage a likely contributor to the symptoms experienced by patients and key to understanding AD pathophysiology [280].

Interestingly, tracts damaged during disease typically include those which contain axons projecting to and from the medial temporal lobe (MTL), such as the parahippocampal cingulum, fornix and uncinate faciculus [28, 280, 281]. This observation is coincident with the early distribution of tau pathology, which typically manifests initially in MTL structures. In support of this hypothesis, recent work has linked antemortem DTI alterations to tau pathology progression [40]. Tau, normally an axonal microtubule-binding protein, becomes abnormally hyperphosphorylated, folded, and prone to aggregation during AD. Hyperphosphorylated tau becomes dissociated from microtubules, leading to impairment of fast axonal transport (FAT) capability and appearance of dystrophic axons [282-285]. A class of dystrophic axons, neuropil threads, are filled with phospho-tau aggregates, which form early in the disease, often before neurofibrillary tangle pathology in cell bodies [286, 287]. Resulting aggregates are associated with local induction of caspase-6, which has been implicated in precipitating axonal degeneration [16, 288, 289]. These findings may implicate tau pathology spreading through axons as a primary event leading to progressive degeneration in AD.

To explore the pathological mechanisms leading to DTI-detectable WM alterations, we used an animal model to test whether distal injections of Aβ could induce tau-associated white matter damage detectable *in vivo* with clinically available DTI. Although the full scope of interactions between Aβ and tau pathology remain a topic of intense research, studies suggest that intracellular tau pathology can be exacerbated by the presence of extracellular Aβ [290-293]. Furthermore, Aβ-induced tau pathology may spread through

axons in a retrograde manner [69, 290, 294]. As shown in a landmark study by Gotz et. al., extracellular accumulations of Aβ can stimulate tau phosphorylation and aggregation in neurons with axons projecting into the injection site in mice expressing the mutant FTDP-17 (p301L) form of human tau, but not wild type mice [69, 292, 293]. P301L tau provides a tool for research to study tauopathy; mice expressing the mutant variant exhibit well characterized age-dependant increases in neuronal tau pathology within cell bodies, dendrites and axons mimicking pathology observed in AD [61]. We focused our investigation on the mouse visual system, which has well characterized neuronal identity and architecture and exhibits tau pathology in several cell types, including retinal ganglion cells (RGCs) [295]. Mouse RGCs, whose cell bodies are in the retina, project axons into the brain through the optic nerve (ON) and optic tract (OT), before terminating in the lateral geniculate nucleus (LGN) [213]. We examined changes in the visual system after Aβ injections into the left LGN using a combination of DTI, Optical Coherence Tomography (OCT) and end-stage histology. As mice have primarily monocular vision, with >95% of RGCs projecting into the contralateral side of the brain, the unaffected side of the visual system can serve as an internal control [296, 297]. Assuming axonal degeneration may be related to microtubule destabilization induced by tau pathology, microtubule-stabilizing drug Epothilone D (EpoD) intervention was tested to rescue the damage. These experiments may yield important information about the process leading to axon loss during AD, link clinical imaging findings to tissue-level histology data and provide potential therapeutic approaches.

Materials and Methods

All experimental procedures were in accordance with National Institutes of Health guidelines for the use of animals in research and were approved by the Institutional Animal Care and Use Committee of Loma Linda University.

Injection Procedure

Human $A\beta_{1-42}$ (A9810, Sigma Aldrich, USA) was prepared using a modified version of a previously described protocol [298]. Briefly, 1,1,1,3,3,3-hexafluoro-2-propanol (HFIP, Sigma) films from synthetic $A\beta_{1-42}$ peptide (Abcam) were dissolved in saline to a final concentration of 10nmol / 3µL. Preparations were then incubated with shaking for 72 hours at 37C. Mice were anesthetized by 1.5% isoflurane/oxygen using an isoflurane vaporizer (VetEquip, Pleasanton, CA). Body temperature was maintained using an electric heating pad during the procedure. Mice were placed in a stereotactic apparatus for injection guidance. Mouse heads were shaved and skin was cleaned with Povidine (Rugby Laboratories). After craniotomy, Aβ was injected slowly into the left LGN (coordinates: -2.46mm posterior from Bregma, lateral 2.2mm, 2.5mm from cortical surface) using a 5-µl Hamilton syringe with an injection speed of 0.3 µl/min. The needle was kept in the injection site for an additional 10 minutes, then withdrawn 0.5 mm every 5 minutes until complete removal from the brain. The incision was then sutured and the animals were left to recover on an electric heating pad.

Longitudinal DTI / OCT examination

Mixed, littermate cohorts (50:50 M:F) of 10 month JNPL3 p301L tau mice were used for this experiment. Mice were injected with either 10nmol Aβ (N=8) or a vehicle saline solution (N=8). Eight untreated mice were reserved as controls. Mice were scanned using MRI after 1 (n = 8 Aβ treated, n = 3 vehicle), 4 (n = 8 Aβ, n = 5 vehicle) and 8 (n = 8 Aβ, n = 7 vehicle, n = 8 control) weeks. OCT scans were collected from all mice in parallel at baseline and again after 4 and 8 weeks. Mice were sacrificed for histology immediately after final OCT and DTI examinations after 8 weeks.

Epothilone D treatment experiment

Seven, 10 month old p301L mice were treated with EpoD for eight weeks following Aβ injection. EpoD was purchased from Abcam (ab143615). EpoD treated mice were given weekly intraperitoneal injections of Epod at 1mg/kg dissolved in DMSO, starting one week prior to initial Aβ injection. Previous PK/PD experiments suggest that EpoD has a residence time in the brain >10 days after a single dose at 3mg/kg [101]. This dose was chosen based upon previous work by Brunden et. al. in which EpoD at 1mg/kg was sufficient to reduce axonal dystrophy in PS19 mice [101]. Mice were examined using OCT 0,1,4 and 8 weeks following treatment. All mice were sacrificed after 8 weeks for histology.

Acute Aβ administration experiment

In order to examine the acute effects of Aβ and EpoD immediately following injection, twelve p301L mice underwent Aβ injection. Six of the mice were pretreated with EpoD one week before injection and again on the day of injection. In each cohort, N=2 were 10 month old, and N=4 were 3 months old. All mice were then sacrificed after 3 days to examine tissue for histology.

DTI Acquisition

MRI acquisitions were collected using a Bruker 11.7T BioSpec small animal MRI instrument with slice thickness 0.5mm, FOV of 1.5 x 1.5cm and matrix 128 x 128 (zero filling to 256 x 256), TR 2.5s, TE 29ms, Δ20ms, δ 3ms and a 21-direction diffusion scheme with b=0.85ms/um^2, and two non-diffusion weighted scans. Raw diffusion-weighted images were processed using FSL (http://fsl.fmrib.ox.ac.uk/fsl/fslwiki/FDT), including steps for skull stripping and eddy current/motion correction using BET and Eddy modules, respectively. Corrected image sets were then loaded into 3D Slicer, and DTI maps including fractional anisotropy (FA), trace of diffusion (TR), axial diffusion (AxD) and radial diffusion (RAD) were created.

DTI Analysis

ROIs were defined manually in the LGN, OT and ON. ON and OT ROIs were manually defined by a blinded observer using the high FA/low RAD which provide contrast against neighboring CSF and grey matter. ON DTI measures were made in two serial sections.

Individual slices contained central regions within each ON with 8-12 voxels. OT regions were selected in two serial sections, comprising 50-60 voxels. LGN regions were defined using a mouse brain atlas as a reference (Franklin and Paxinos, 1997) and were bounded by the hippocampus (superior boundary) and external medually lamina (lateral boundary, high FA). Changes in diffusion metrics were computed by calculating the diffusional asymmetry (injured side [left LGN, OT and right ON] / contralateral side). This allowed each mouse to serve as its own control to reduce the degree of variability between animals.

OCT Acquisition

OCT imaging was performed using a BioOptigen Envisu C-Class. Our imaging protocol collected data from a 1.6 x 1.6 mm region centered on the optic disc. The protocol used 1000A scans/B Scan, 100 B scans total. B scans 320um and 240um superior and inferior to the optic disc (N=4 per eye) were selected for analysis. These regions were selected for their consistent layer thickness characteristics. Images were processed and analyzed using custom software created in Matlab (Natick, MA). Individual B scans were pre-processed by manually removing retinal segments containing blood vessels along the RNFL surface. A fitted quadratic curve was then used to adjust individual A-scan positions to straighten the retina. All scans were manually reviewed to assure the straightness of each B scan. With the resulting straightened B scan, all scans were averaged, and the profile of intensity variation across of retina was plotted. Measurement of GCC layer thickness was made based upon the intensity differences between layers. The Ganglion cell complex

(GCC), which is composed of the soma, dendrites and axons of RGCs was defined as the distance between the retinal nerve fiber layer (RNFL) peak intensity and the intermediate border between the inner plexiform layer (IPL) maxima and the underlying Inner nuclear layer (INL) minima.

Histology

Mice were anesthetized and perfused with 4˚C PBS, then 4% paraformaldehyde. After perfusion, tissues were immersed in decalcification buffer for one week. Tissues were then sliced into 3mm-thick sections and processed for paraffin embedding. Resulting paraffin blocks were then sectioned at 5μm for sections of ON, OT, Retina and LGN.

Tissue sections were immunostained for markers of healthy axons (phosphorylated neurofilament, SMI-31, 1:1000; Covance), myelin sheaths (MBP, 1:1000; Zymed Inc), Aβ (1:100; ThermoFisher), presynaptic terminals (Synapsin-1, 1:2000; Cell Signaling), and Phospho-tau (p-tau, AT8, 1:400; ThermoFisher). Briefly, sections were deparaffinized, permeabilized in 0.3% Triton X-100, boiled in citrate buffer pH6, blocked in 3% NGS then incubated overnight in 1˚ antibodies. Fluorescently labeled sections were then incubated in appropriate 2˚ antibodies for 1hr and mounted for imaging. Brightfield detection of 1˚ antibodies was carried out using the Universal Quick HRP Kit (Vector labs) and counterstained with hematoxylin. Slides were imaged using a Keyence microscope using identical acquisition settings. Stained sections were analyzed using ImageJ.

Immunohistochemistry Analysis

Axon and myelin immunohistochemistry (SMI31/MBP) were quantified in the OT using tissue sections imaged at 10x, from ~Bregma -1.82. Images from the left and right OT were acquired, using identical acquisition settings, below the threshold for image saturation. ROIs were drawn around the entire OT and mean pixel brightness was measured. These measurements were used to compute intensity asymmetry between left and right OTs. In the ON, axon numbers and AT8+ axons were measured using coronal sections through each nerve. Stained ONs were imaged using a 40x objective, then analyzed using the threshold and analyze particles segmentation functions in ImageJ.

Three retinal sections from each eye within 200μM of the optic disc were selected for fluroro-Nissl staining (NeuroTrace, ThermoFisher). After staining, sections were imaged at 20x using ImageJ. Images were acquired within the central 1mm portion of each retina. RGC cell bodies were counted in the most superficial retinal layer and calculated as RGC density per unit μM.

General tau pathology levels in the brain were assessed in p301L mice by AT8 immunohistochemisty in the CA1 region of the hippocampus. An ROI 500μM wide was placed in the most superior region of the CA1b, capturing the stratum oriens, pyramidale and radiatum layers. Percent area measurements were performed to determine the p-tau burden in each hippocampus. Tau pathology induction after acute Aβ injections were measured in the CA3 region of the hippocampus. This region facilitated straightforward

identification of neuronal p-tau in the pyramidal layers, (500μM span) in the most medial region of CA3 adjacent to the Dentate Gyrus.

Statistical Analysis

All results are expressed as mean ± standard deviation (SD). Asymmetry ratios of DTI data, (e.g. injury side /control side FA_i/FA_c from ON) and injury/control staining from histology measures (e.g. $SMI31_i$ / $SMI31_c$) were calculated for analysis. DTI data were analyzed using a linear mixed model approach to test for effects of timepoint (1,4 or 8 weeks post injection) treatment (Aβ or vehicle) and timepoint × treatment interactions. To evaluate treatment effects on DTI parameters between experimental and vehicle control groups, data were compared at each timepoint using Man-Whitney *U* test. Single group data were compared between timepoints using the Friedman test with post-hoc Dunn's test. Histology data was analyzed using a one-way ANOVA with post-hoc Tukey's test. Correlations between DTI metrics and histology measures of axon and myelin were performed using a Pearson's correlation coefficient. All *p* values below $p<0.05$ were considered statistically significant. Analysis were performed in Prism Graphpad (La Jolla, CA) and SPSS (Chicago, IL)

Results

DTI and OCT alterations to the visual pathway after Aβ injection

One week after injections, mice were imaged using DTI to confirm the injection location and determine if there were any early alterations to visual system microstructure. The

injection tract was visible, allowing confirmation of successful LGN targeting. In the Aβ-injected LGN, we found reductions in diffusion magnitude (TR, asymmetry = 0.867), relative to vehicle controls (asymmetry = 0.996) at 1 week (Figure 5.1c,d). This initial reduction in diffusion among Aβ-treated mice was transient and significantly increased relative to 1 week measures after 4 (asymmetry = 1.03) and 8 weeks (asymmetry = 1.07).

Within the OT, linear mixed model analysis revealed an effect of treatment ($F = 8.742$, $p = 0.006$) on FA asymmetry and treatment ($F = 7.344$, $p = 0.012$) as well as treatment × timepoint ($F = 4.289$, $p = 0.025$) on AxD asymmetry. After four weeks, we observed statistically significant ($p<0.05$) differences to DTI asymmetry in the OT between treatment groups; Aβ-treated mice showed significant reductions in AxD asymmetry (0.92) vs. vehicle controls (1.06), (Figure 5.3). No significant changes between groups were observed after 8 weeks. Within the ON, mixed models revealed a significant effect of treatment ($F = 6.641$, $p = 0.015$) and treatment × timepoint ($F = 5.274$, $p = 0.014$) on AxD asymmetry measurements. Nonsignificant trends were also observed for treatment × timepoint on FA asymmetry ($F = 3.381$, $p = 0.052$). Eight weeks after injection, we found significant reductions in FA and AxD asymmetry among Aβ-treated mice (FA, 0.85; AxD, 0.82) vs. vehicle controls (FA, 1.06; AxD, 1.01). Collectively, these results show the pattern of diffusion alterations that result from Aβ-injection into the LGN. Changes appeared first in the LGN and OT, then subsequently in the ON.

Measurement of GCC thickness asymmetry revealed no significant differences between groups either at baseline or after 8 weeks (Figure 5.4). We also found no absolute changes in thickness relative to baseline measures in any group (data not shown).

Histological Examinations of Aβ and Vehicle treated mice

Eight weeks after Aβ injection, obvious reductions in Synapsin-1 (syn-1, a marker of presynaptic terminals labeling) were apparent in the left LGN, relative to the contra-lateral side (Figure 5.5). This reduction appeared to coincide with loss of tissue integrity in the LGN as well as the overlying CA3 / Dentate Gyrus regions of the hippocampus to varying degrees among the Aβ-injected mice (Supplemental figure 5.9).

The ON and OT were examined using immunohistochemistry for markers of healthy axons (SMI31) and myelin (MBP). Measurements of SMI31 intensity asymmetry (L/R) revealed significant reductions in axon labeling among Aβ-injected mice (0.82), relative to vehicle controls (0.98, Figure 5.6a). Measures of myelin intensity revealed no significant differences in staining asymmetry between groups. Within the ON, the coronal sections permitted quantitative measures of axon numbers. We found significant reductions in axon number asymmetry in Aβ-treated mice (asymmetry = 0.70) , compared with vehicle-treated mice (1.09) (Figure 5.6b).

FluoroNissl-stained retinal sections were used for quantification of RGC cell bodies within the GCL sublayer (Figure 5.6d). Density of cell bodies across the GCL was

measured for each eye. Comparison of density asymmetry between groups revealed a significant reduction in cell bodies in the Aβ injected group (asymmetry = 0.83), compared to vehicle controls (1.04, $p<0.01$).

Comparisons between DTI and histology datasets revealed significant correlations between ON FA ($r = 0.739$, $p = 0.0025$), AxD ($r = 0.562$, $p = 0.0364$) and RAD ($r = -0.557$, $p = 0.0387$) asymmetry measures and axon counts (Figure 5.6c). No significant relationships were found between myelin staining and DTI measures.

Histological examination of tau pathology

Immunolabeling of tau phosphorylation (p-tau) was examined using the AT8 antibody (Figure 5.7). We found a high degree of variability in the number and density of p-tau bearing axons between animals. This variability generally correlated with the degree of AT8+ staining observed within the GCC layers of the retina (Figure 5.7b). However, we found no significant differences in p-tau axon density between left / right ONs or between different treatment groups (Figure 5.7d). Additionally, we found no significant correlations between axon losses and density of AT8+ axons (Figure 5.7e).

Severity of p-tau pathology was also quantified in the CA1 region of the hippocampus, as a general index of p-tau within the brain. The observed staining was concentrated within pyramidal neurons and their dendrites (Figure 5.7c). As in the ON, we also observed large degrees of variance between different animals in the Aβ and vehicle-injected

cohorts. We found a trend toward higher levels of tau pathology in the Aβ-treated cohort vs. vehicle cohort, though no significant change was apparent.

Histological examination of Aβ / EpoD treated mice

Examination of Aβ injected mice treated with EpoD revealed several surprising findings. In the LGN, EpoD treatment appeared to preserve Syn-1 labeling that was lost in Aβ-injected cohorts. (Figure 5.5). Similarly, we found EpoD treatment normalized SMI31 labeling asymmetry in the OT (Figure 5.6a) and the ON (Figure 5.6b). Additionally, EpoD-treated mice showed no significant RGC density asymmetry in the retina (Figure 5.6d). We found no differences in AT8+ axon numbers in the ON among these mice vs. controls (Figure 5.7d). However, significant (>80%, $p<0.01$) reductions in p-tau were apparent in the hippocampus, as compared with the Aβ-treated cohort (Figure 5.7c,f).

Acute effects of Aβ and EpoD on tau pathology

To probe the acute effects of Aβ and EpoD in this experiment, we sacrificed four, 10 month old p301L mice 3 days after treatment (2 Aβ-injected, 2 Aβ/EpoD). In and around the injection site, we could see Aβ in the LGN and CA3 region of the Hippocampus (Figure 5.8a). Surrounding the injection site, p-tau bearing neurons were evident. These increases were immediately apparent by comparisons to the contra-lateral Hippocampus/LGN (Figure 5.8b). However, these increases in p-tau were not seen in mice pretreated with both Aβ/EpoD. Additionally, no asymmetry in p-tau axon numbers was observed in ON sections. To confirm this result and rule out the contribution of pre-

existing pathology in aged mice, we repeated the experiment using eight, 3-month p301L mice (4 Aβ-injected, 4 Aβ/EpoD) with minimal pre-existing tau pathology. In this cohort, we found no existing p-tau pathology in ON axons from either cohort, but did find obvious p-tau pathology in Aβ-treated mice in both the hippocampus and LGN (Figure 5.8c) exclusively on the injected side. Similar to earlier findings, mice pre-treated with EpoD showed significantly reduced increases in p-tau pathology, relative to mice Aβ-treated alone (Figure 5.8d).

Discussion

In the present study, we tested whether retrograde axonal damage results from Aβ-induced tau pathology at sites distal from the cell body. Measuring visual system microstructural properties by DTI allowed us to connect noninvasive surrogate measures to discrete pathology, and link our data to clinical findings. Our data reveal that LGN Aβ injections lead to selective loss of WM integrity by DTI, which appears to correlate with axon loss. Longitudinal data suggest that alterations within the visual pathway manifest first in the LGN, OT and later in the ON, suggestive of a retrograde degeneration process. Additionally, our data suggest that the microtubule-stabilizing compound EpoD can prevent Aβ-induced tau phosphorylation and preempt downstream neurodegeneration.

Axonal damage and WM abnormalities in AD have been documented in numerous neuropathological studies [299-303]. The advent of DTI has facilitated the *in vivo* study of white matter microstructure alterations during the course of AD [304]. These alterations

likely reflect the loss of connectivity within neural circuits, directly contributing to cognitive decline during AD. As such, research has been pursued to link DTI-detectable WM damage with specific AD pathologies. However, DTI studies examining AD-model mice have shown variable and at times contradictory results. APP-overexpressing models have shown age-dependant reductions in white matter FA/RAD in two studies [2, 71], and increases in these metrics in another [114]. Tauopathy models have shown reductions in FA/RAD white matter in a pair of studies [116, 117], while the triple transgenic model (with combined APP/tau expression) does not reveal changes relative to controls [118]. The lack of a consensus model system to explore how development of AD pathology impacts WM and vulnerable neurocircuitry has impeded the development and testing of therapeutics to correct these deficiencies.

Our lab has conducted several studies to investigate the effects of Aβ on WM integrity [144, 187]. A high-dose injection of Aβ in the LGN weakened amplitude of the visual evoked potential (VEP), possibly by impairing synaptic function, but did not cause DTI alterations in either the ON and OT of WT C57Bl/6 mice. Following from the work by Gotz et. al., who demonstrated the ability of Aβ to induce p-tau accumulation through axonal connectivity in p301L tau but not WT mice, we reran our previous study using p301L tau mice [69]. We demonstrate that Aβ injections in p301L mice precipitate changes in DTI metrics as well as measureable axon loss. Collectively, our work demonstrates the critical role of pathological tau to enable Aβ-induced axonal damage and the

temporospatial profile of axonal degeneration, which may propagate from the injection site toward cell bodies.

In our experiment, we found that DTI alterations are correlated with axon loss. This finding is consistent with DTI-axon correlations that have been made in other models and human tissue [159, 213, 267, 305, 306]. Similar to our findings, in human studies, reductions in FA and increases in RAD in abnormal WM in both MCI and AD patients were found to correlate with axon loss [159, 213, 267, 305, 306]. DTI findings from this study do differ from human AD data with respect to changes in AxD. In damaged white matter during AD, AxD measures increase relative to controls, while we found reductions in measures of AxD [304]. This difference may be explained by microenvironment differences after acute vs. chronic axonal degeneration. In mouse models, reductions in AxD are often seen during acute axonal degeneration [26, 213]. AxD is thought to represent the diffusion along the lengths of fibers, whose reduction could be caused by cytoskeletal breakdown or focal 'beading' along axons [202]. Reductions in AxD is observed in human WM during acute injury settings, as in optic neuritis (inflammation/neurodegeneration of the ON) [227]. This reduction is transient, though and eventually increases relative to control subjects [224, 227]. Our measurement of AxD may follow this pattern in the OT, which shows early (4 week) reduction, then later normalization by 8 weeks.

The DTI and histology data from this study is suggestive of a 'dying-back' degeneration pattern, in which axons die-back from the synapse, leading to neuronal loss. In our

experiment, loss of presynaptic terminals, axons and cell bodies follow from Aβ-injection into the LGN. These observations raise the prospect that degeneration could be initiated through axonal or synaptic mechanisms, independent of apoptosis, a mechanism which has been widely studied in other model systems, such as spinal cord injury and Multiple Sclerosis [9, 13, 307]. Notably, suppression of this pathway by overexpression of nicotinamide mononucleotide adenylyl transferase 1 & 2 (NMNAT), are neuroprotective in tauopathy models [308 309]. These findings suggest that axonal damage and dysfunction may be a key initial step in tau-mediated neurodegeneration. This idea is bolstered by evidence from AD tissue, suggestive of early axonal dysfunction preceding overt cell loss. This includes the presence of dystrophic axons, dsyfunctional axonal transport and cytoskeletal abnormalities early in the disease process [99, 310]. Our findings support the possibility of 'dying-back' degeneration in AD and imply that tau pathology induced by Aβ may be central to this process.

In contrast to the significant reductions in RGC density observed in the retinas of Aβ-treated mice, we did not find significant reductions of retinal thickness examined *in vivo* by OCT. The reason for the resistance to retinal thinning in our model is not clear, possibly explained by tissue swelling to compensate for cell loss. Nevertheless, visual deficits are common in patients with AD. We previously demonstrated that abnormal DTI metrics are present in the visual pathway of patients with MCI and AD [167]. Additionally, reductions of RGCs and RNFL thickness by OCT have also been widely reported in AD and MCI patients [155, 311, 312]. Our findings provide new insight into the possible

mechanisms behind visual deficits in AD. Early intervention may interrupt this process and protect the visual system.

Our data suggest that microtubule stabilizers such as EpoD may have a therapeutic effect sufficient to reduce tau pathology as well as synapse, axon and cell losses induced by Aβ. These results are congruent with previous studies that have demonstrated the blood-brain-barrier permeability of the drug and its neuroprotective qualities in pure tauopathy models [101, 109]. Data from previous studies have found evidence that EpoD can promote axonal health by reducing axonal dystrophy, increasing ON microtubule density and normalizing fast axonal transport [101, 109]. Additionally, previous studies utilizing EpoD as well as microtubule-stabilizing peptide NAP have both shown ability to reduce p-tau pathology in AD model mice over several months of treatment [109, 313, 314]. Our data recapitulates these findings, showing much lower levels of tau pathology among EpoD treated mice. Furthermore, our data suggests that EpoD treatment can prevent acute tau phosphorylation induced by Aβ, and may prevent downstream axonal and cell losses.

In summary, our data demonstrates that Aβ injection can induce retrograde axonal damage in P301L mice. This axonal damage can be detected by DTI, and the findings mirror several aspects of clinical data obtained from patients with AD. Our *in vivo* imaging approach paired with histology enabled us to detect the temporospatial profile of degeneration. Epothilone D administration is sufficient to prevent this damage, limiting

the induction of p-tau pathology and preventing downstream degeneration in the OT, ON and RGCs.

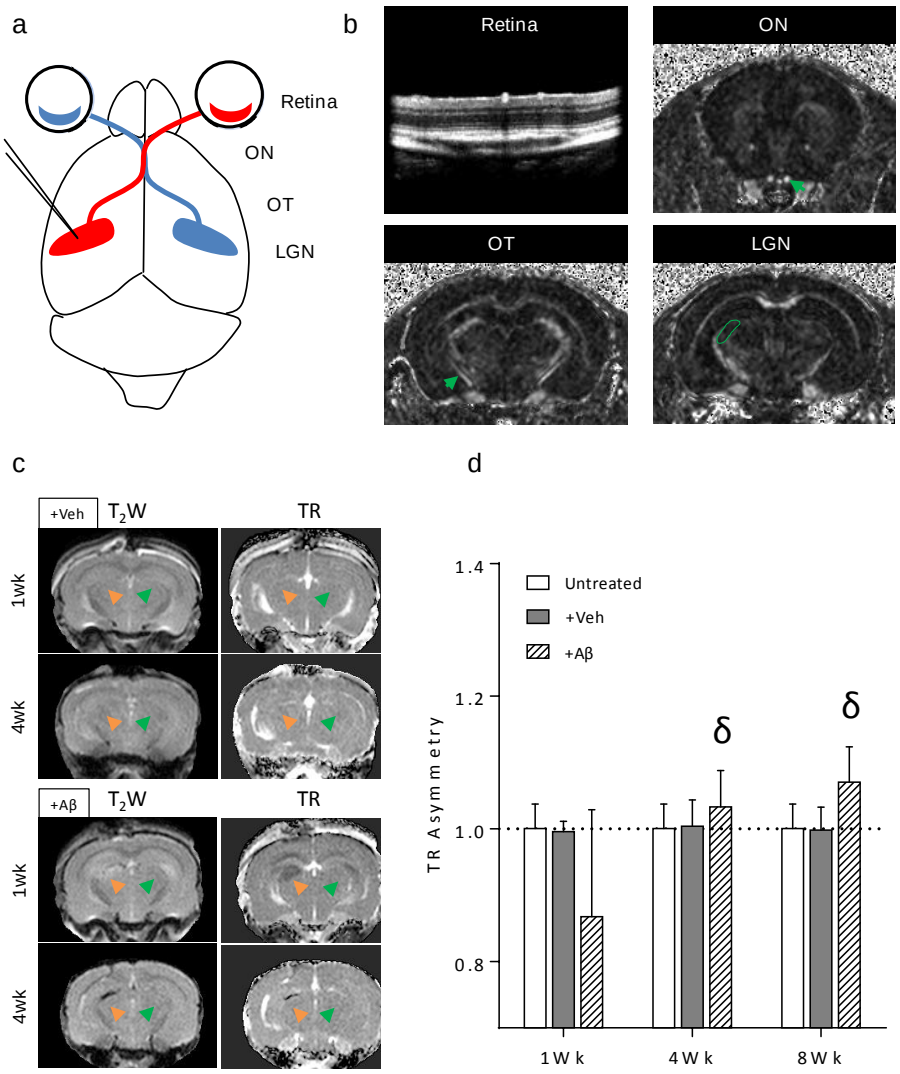

Figure 5.1 (a) Diagram showing the mouse visual pathway and injected region. The pathway affected by the Aβ injection is shown in red. (b) *In vivo* images from OCT and DTI showing the examined structures including the retina, ON, OT and LGN. (c) T2-weighted and TR images from either Aβ or vehicle injected LGN-sections. Injected LGN is indicated by the orange arrow, with green indicating the untreated side. A transient reduction in LGN TR in the Aβ-injected side is visible at 1 wk. (d) Graph of TR asymmetry across the timecourse. "δ" Indicates data significant difference from group-matched 1 week data.

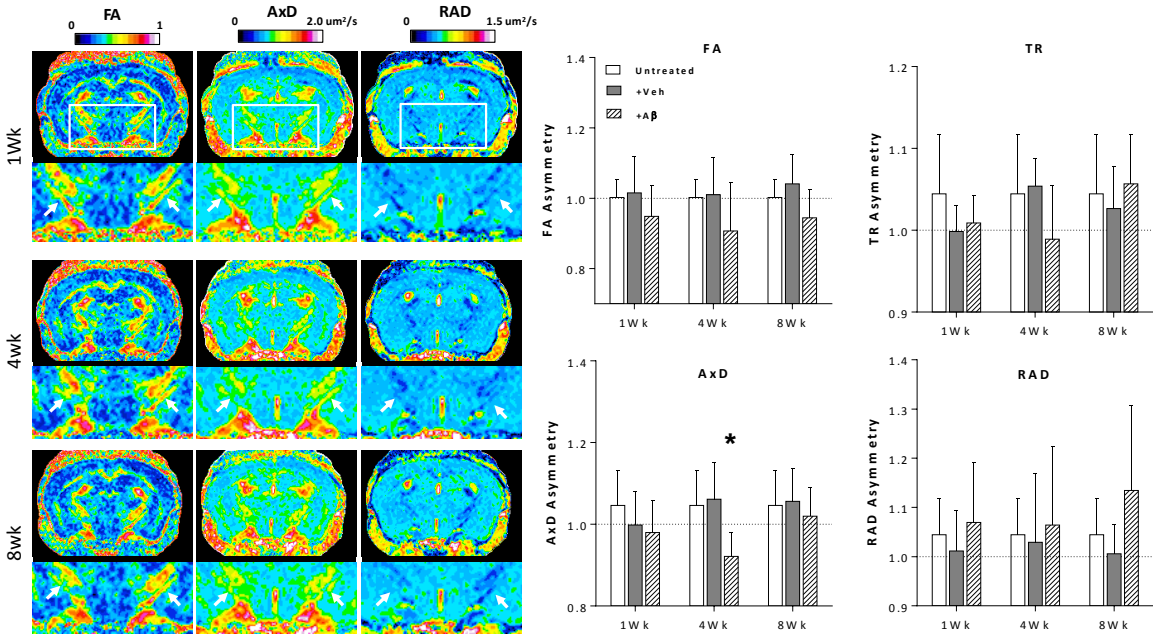

Figure 5.2 DTI alterations within the OT. Left, pseudocolored DTI images from a single animal showing the changes in FA, AxD and RAD across the time-course after Aβ injection. Right, quantification of DTI metric asymmetry in the OT. Significant reductions in AxD relative to vehicle controls are observed after 1 month. "*****" Indicates significant difference from timepoint-matched vehicle controls.

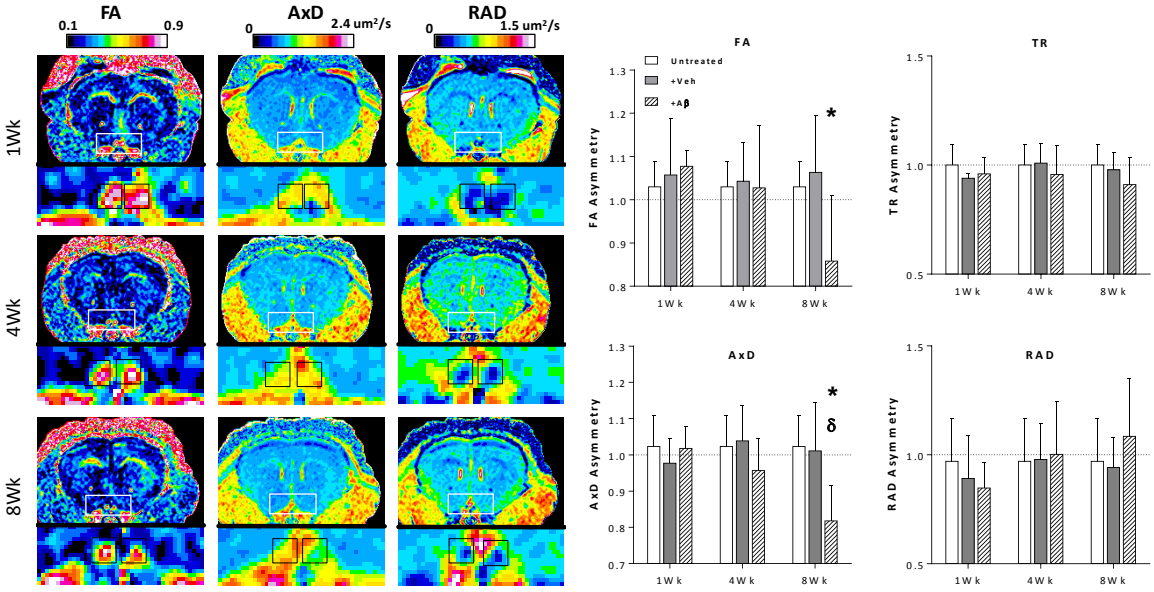

Figure 5.3 DTI alterations within the ON Left, pseudocolored DTI images showing the selective changes in right ON 8 weeks after Aβ injection. ONs shown by black boxes. Reductions in FA and AxD were seen in the right ON compared with the contralateral nerve. Right, quantification showing the changes in all DTI asymmetry metrics after 1, 4 and 8 weeks. "*" Indicates significantly difference from timepoint-matched vehicle controls, "δ" indicates significant difference from group-matched 1 week data.

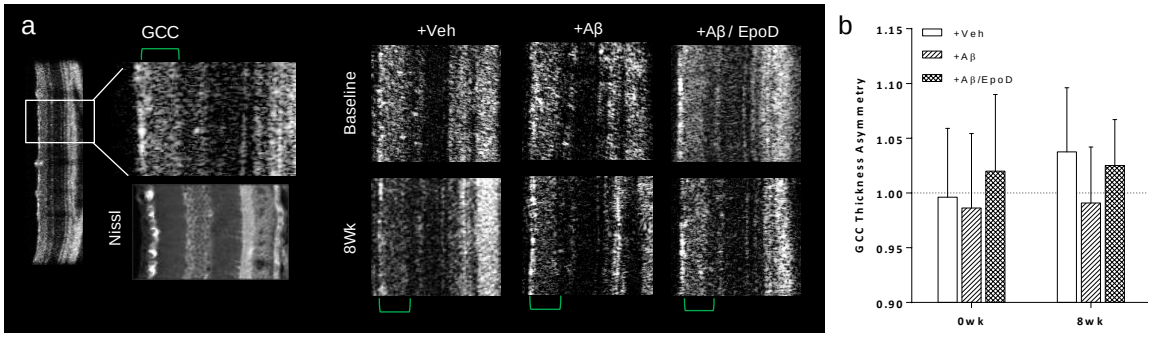

Figure 5.4 OCT measurements of GCC layer thickness (a) OCT B-scan and magnified region showing layer detail in comparison with Nissl-stained section. GCC layer (shown in green brackets) encompasses RNFL, GCL and IPL sublayers. Right, OCT B scans from the right retina among the three experimental groups at baseline and after 8 weeks. (b) Graph showing GCC thickness asymmetry (between right and left retinas) at baseline and after 8 weeks.

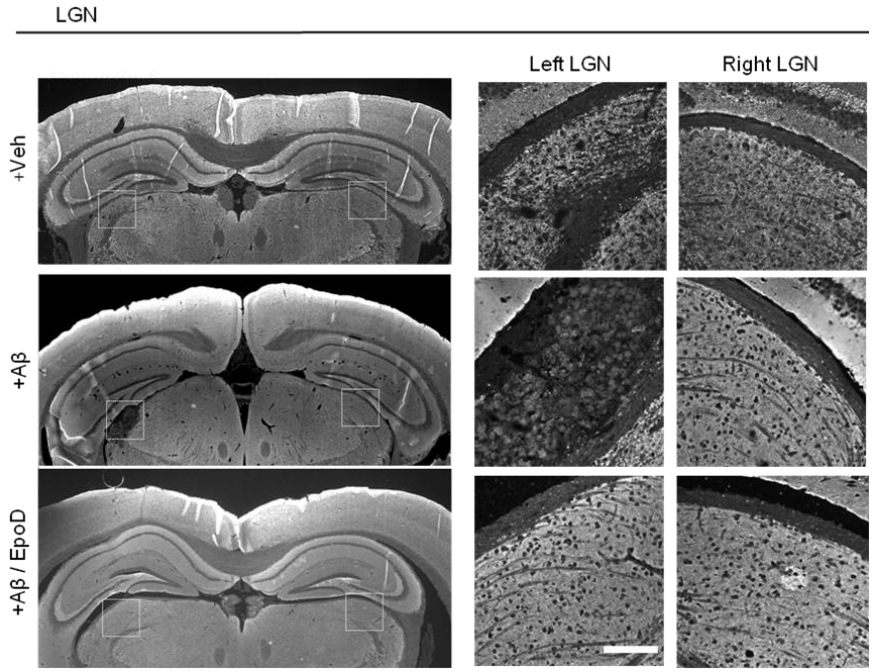

Figure 5.5 Presyanptic terminal labeling in the LGN. Synapsin-1 immunohistochemistry of presynaptic terminal density across the brain. Selective loss of presynaptic terminals and tissue integrity were seen in the left LGN of Aβ-injected mice. Obvious terminal or tissue loss were not apparent in vehicle or EpoD-treated mice. Scale bar = 50μm

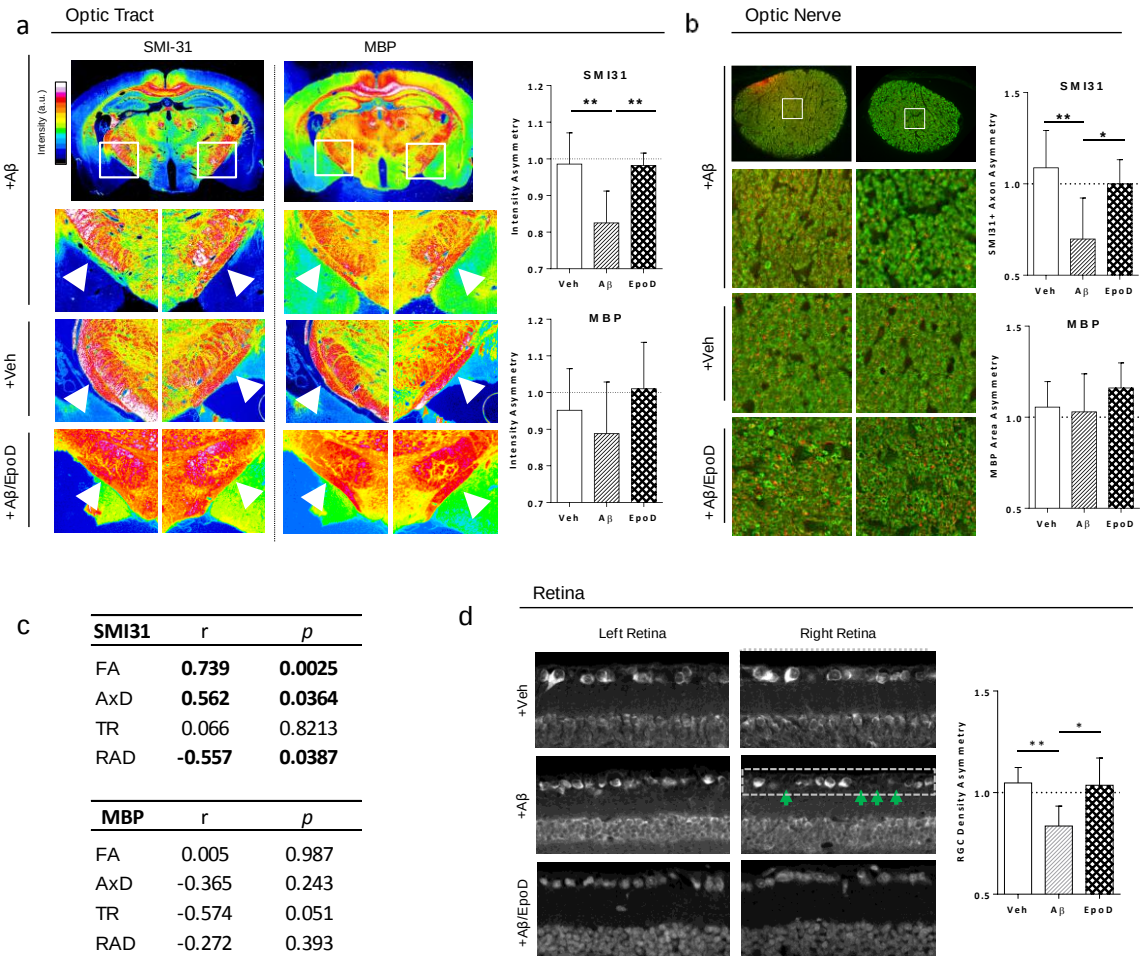

SMI31	r	*p*
FA	**0.739**	**0.0025**
AxD	**0.562**	**0.0364**
TR	0.066	0.8213
RAD	**-0.557**	**0.0387**

MBP	r	*p*
FA	0.005	0.987
AxD	-0.365	0.243
TR	-0.574	0.051
RAD	-0.272	0.393

Figure 5.6 Immunohistochemistry findings from the OT, ON and retina. (a) Staining for axons (SMI-31) and myelin (MBP) in the OT. Images are pseudocolored to show the differences in labeling intensity between left and right. Zoomed images show selective reductions in SMI-31 intensity in the left OT, relative to the right OT in Aβ-injected mice. These changes are not as apparent in MBP labeling. Right, quantification of SMI-31 and MBP OT intensity asymmetry. (b) Axon (red) and myelin (green) staining in the ON. Right, quantification of axon and myelin asymmetry in the ON. Selective reduction of axons but not myelin were seen in Aβ-treated mice. (c) Comparisons between DTI-measured ON asymmetry and IHC-measured axon/myelin asymmetry; significant correlations are shown in bold. (d) Left, representative images showing the GCC of retinas from the three treatment groups. Right, quantification of retina-measured RGC density asymmetry. *, $p<0.05$; **, $p<0.01$

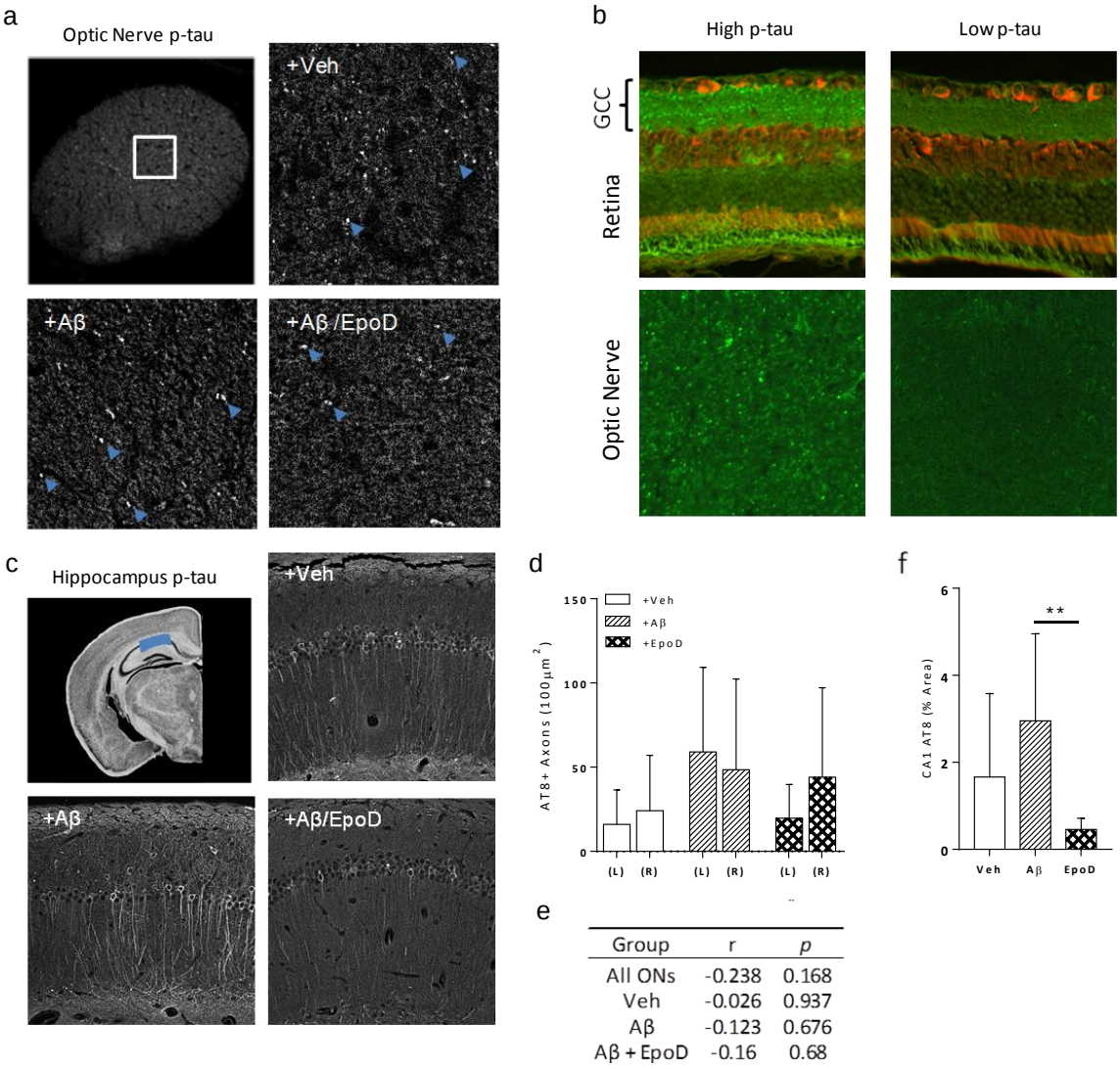

Group	r	p
All ONs	-0.238	0.168
Veh	-0.026	0.937
Aβ	-0.123	0.676
Aβ + EpoD	-0.16	0.68

Figure 5.7 Phospho-tau staining in the ON and Hippocampus. (a) Phospho-tau (AT8) staining in the ON shows punctate axonal staining in the ON among all groups. (b) Retinal sections labeled with p-tau (green) and colabeled with Fluoronissl (red). Representative sections showing high (left) and low (right) levels of p-tau labeling in retina, concentrated with the GCC. Lower sections show each retinas' respective ON section, labeled with AT8. (c) Top left image shows the ROI (blue) from the CA1 region of the hippocampus, where AT8+ staining was quantified, other images show representative levels of p-tau staining. (d) Quantification of AT8+ axon density in left and right ONs among all groups (e) Correlations between ON axon density and AT8+ axon density. (f) AT8 staining revealed a significant reduction of phospho-tau staining in the hippocampus among Aβ/EpoD treated mice compared with Aβ treatment alone .**, $p<0.01$

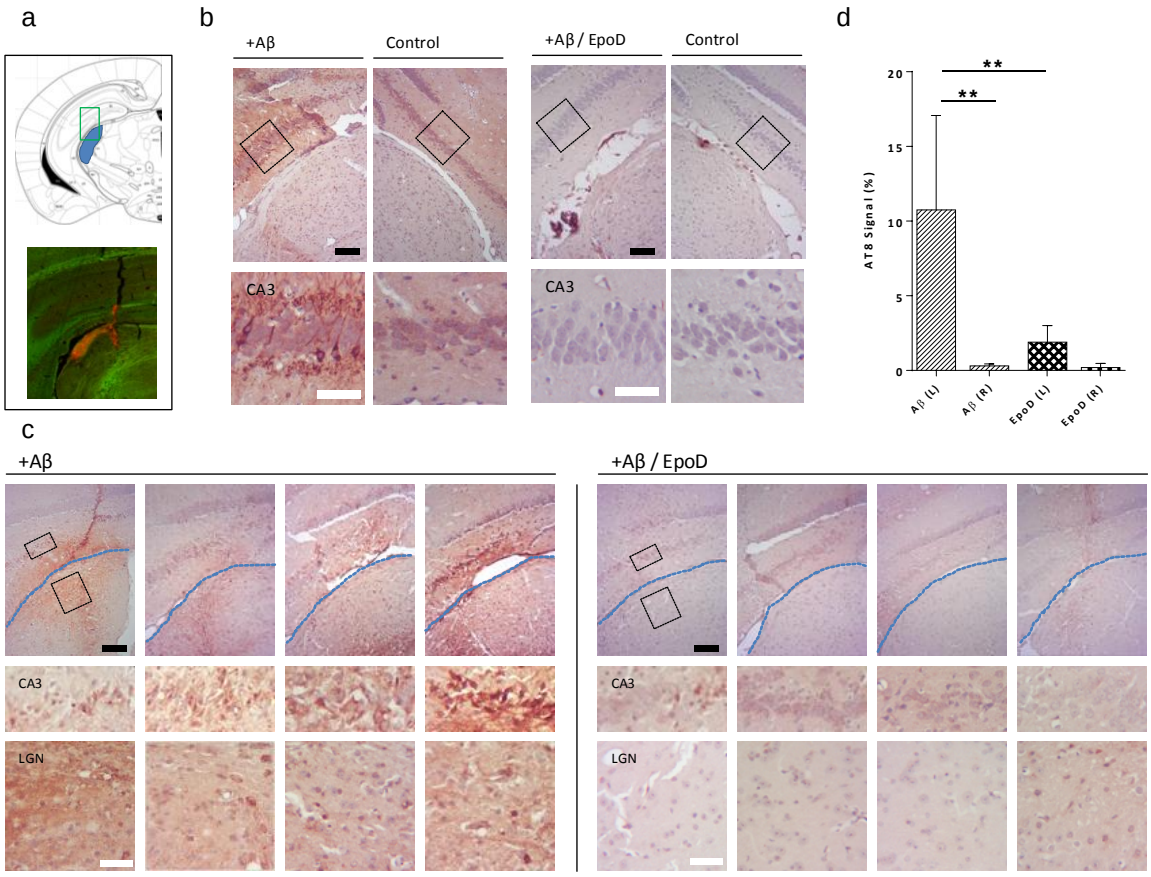

Figure 5.8 Phospho-tau induction in the LGN and Hippocampus after acute Aβ injection. (a) Top, coronal atlas section shows the injection location. Bottom, zoomed-in region showing Aβ (red) within LGN and hippocampus 3 days after injection. (b) AT8+ p-tau staining in10-month old p301L mice 3-days after injection. Abundant tau pathology is apparent in the injection region, but absent in the contralateral LGN/hippocampus and in mice pre-treated with EpoD. (c) Left, young, 3 month old p301L mice show AT8+ p-tau pathology 3 days after Aβ injection in both the hippocampus and LGN. Blue line denotes the border between LGN and hippocampus. Right, mice pre-treated with EpoD show greatly reduced tau pathology in hippocampus/LGN. Black scale bars show 100µm, white bars show 50µm. (d) Quantification of p-tau staining in the CA3 layer. **, $p<0.01$

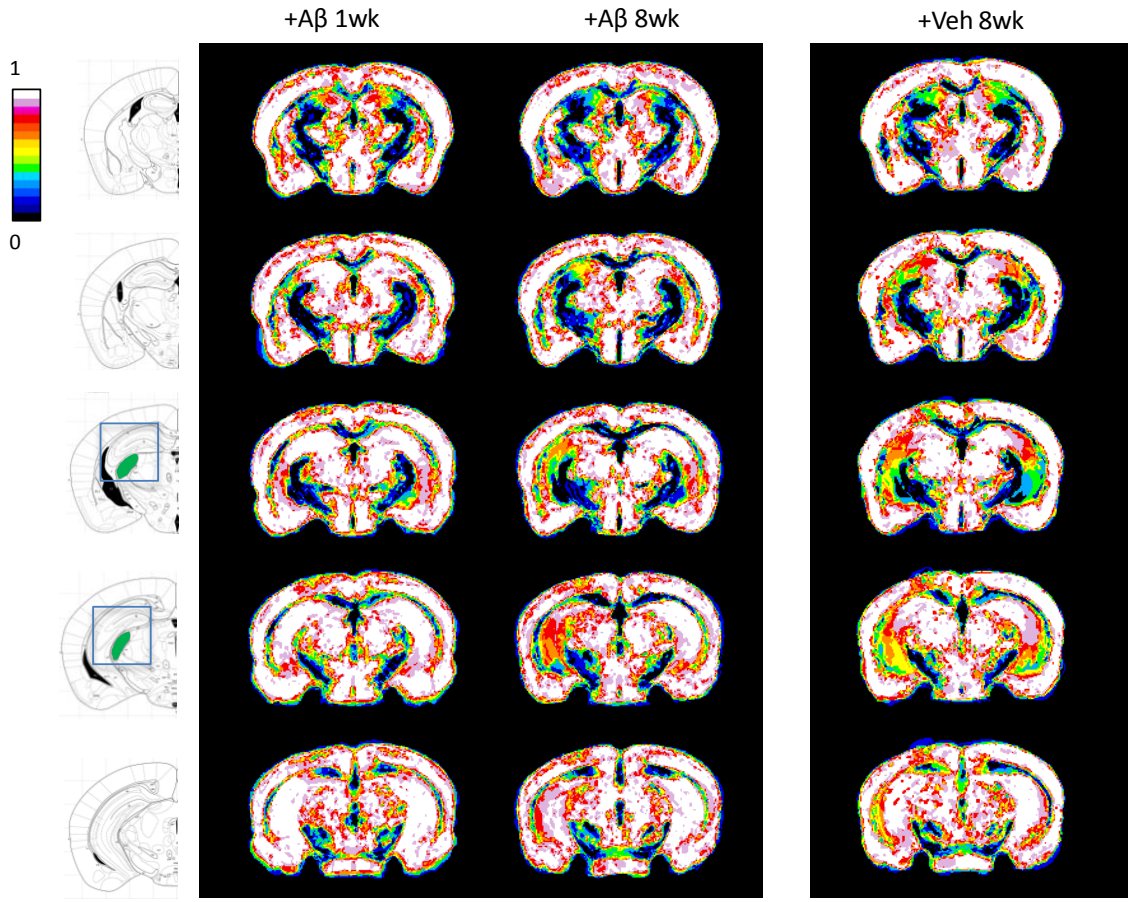

Supplemental Figure 5.9 Grey matter probability map. Sequence of sections from rostral (top) to caudal (bottom). Maps illustrate the probability of finding grey matter at a voxel level (0-1). Left, atlas maps showing the location of the LGN (green). Aβ-injected mice after 1 week (left) and vehicle injected mice after 8 weeks (right) show similar grey matter density in the LGN and hippocampus between right/left. In contrast Aβ-injected brains show atrophy of the left hippocampus and LGN surrounding the injection site, compared with the contralateral side.

Methods: Six scanned control p301L FA images were brought into common stereotaxic space and registered to a common template image using an affline transformation. These six images were averaged to create a master p301L brain template, to which all other scans were subsequently registered. After registration to the template, images from each mouse were segmented into three tissue classes based upon DTI metrics: white matter (FA > 0.3), CSF (TR > 3.5 um^2/ms) and grey matter (FA<0.3, TR < 3.5 um^2/ms). Tissue class maps for grey matter were averaged to show probability of finding grey matter at a voxel level.

Conclusion

Despite the presence of axonal loss in a variety of neurodegenerative conditions including Alzheimer's Disease (AD), relationships between pathological triggers, neurodegnerative patterns and optimal clinically-relevant biomarkers remain relatively unclear. In these studies, we explored connections between patterns of axon loss, non-invasive biomarkers and the role of AD pathology across a span of different models using the visual system. Data from these studies shed light on the relevance of AD pathology to white matter disruption by DTI, and clarify the ability of noninvasive methods to detect axon dysfunction and degeneration patterns during disease conditions.

Here we show for the first time that the Optic Nerves (ON) of AD patients have significantly lower anisotropy and higher radial diffusion (FA and RAD), compared with similarly aged healthy controls. This suite of alterations is similar to the well-established changes that occur in the posterior cingulum, which are typically interpreted to signal axon loss [315]. Our findings in the ON are complimentary to OCT data from AD patients showing retinal RNFL thinning, suggestive of Retinal Ganglion Cell axon loss [126]. In sum, these findings imply that the visual pathway is vulnerable during disease and may be a relevant system to examine the underlying factors contributing to DTI alterations in white matter [126].

In order to establish the temporospatial connection between axon loss and neurodegenerative biomarkers in the visual system, we induced axonal degeneration in WldS mice using a retinal ischemia (RI) model. The model simulates slow-moving Wallerian Degeneration, a mode of axonal degeneration which is speculated to contribute

to DTI changes in AD [316, 317]. Our data reveal the novel ability to spatially and temporally identify axonal degeneration as it propagates through the visual system white matter in an anterograde manner. Early axon loss in the ON was identified by sharp reductions in trace diffusion, axial diffusion and anisotropy (TR, AxD and RA), without simultaneous changes in the OT. Two weeks after DTI-identifiable changes in ON, similar diffusional alterations manifest in the OT, along with explicit loss of axons by histology. These data show that patterns of axonal degeneration can be discerned in the visual system on the basis of temporospatial diffusional characteristics. In addition to examining diffusion biomarkers of axon loss, our study explored whether subtle Blood-Brain-Barrier dysfunction occurs as a result of ongoing axon loss and/or inflammation using Gadolinium-Enhanced MRI. The noninvasive data suggested that the BBB remains intact, even during periods of extensive neurodegeneration and ongoing gliosis. Several recent studies have highlighted the leaky nature of the BBB during AD; however, our data suggests that BBB-leakage during disease is likely not directly attributable to the process of axon loss, or secondary gliosis [318, 319].

To examine the relationship between retrograde axonal degeneration and biomarkers of cell loss and shrinkage in the retina by OCT, we utilized the EAE model, in which the ON is a frequent, early target of inflammation and axon damage. Our results revealed an initial sharp reduction in ON TR and AxD, two weeks after EAE induction. These DTI changes are identical to the early alterations in the ON observed during Wallerian degeneration in our RI model, suggesting that despite differences in the mode of degeneration, microstuctural changes are similar. Early diffusion changes in ON after

two weeks manifest before measurable alterations in retinal thickness, suggesting that axonal degeneration and cell body loss may be distinguishable events using these parallel noninvasive measures. However, after four and eight weeks of EAE, degrees of GCC retinal layer thickness were highly correlated with diffusion measures (especially FA and RAD) in the ON, suggesting that after several weeks of chronic neurodegeneration, OCT and DTI can provide complimentary information about the extent of axon loss and corresponding cell loss *in vivo*. In EAE mice, this study is the first to compare noninvasive data derived from DTI and OCT with ground-truth histology measures of axon and cell loss. The data establish that both diffusional measures in the ON (especially AxD) and degrees of retinal thinning (relative to baseline) had strong, linear relationships to degrees of axon loss after 8 weeks. These data imply that longitudinal tracking of retinal thinning during neurodegenerative disease are likely accurate, fairly linear proxy measures for gauging rates of axon loss in the visual system.

Next, in a pilot project, we investigated axonal transport function in the ON using in a tauopathy model, and its relationship to diffusional characteristics. As a key feature of AD tauopathy mouse models, deficits in axonal transport are widely speculated to occur during AD and contribute to axon dysfunction and loss [99, 310]. We discovered a novel connection between low baseline ON TR and low rates of axonal transport. These changes were not associated with axonal tau pathology, but did appear to correlate with abnormal myelination patterns. While lowered TR is generally not a feature of white matter changes during AD, the relevance of an association between TR and axonal transport may be applicable to mild traumatic brain injury or Optic Neuritis, in which

acute reductions in TR are seen in white matter pathways, as well as indications of impaired axonal transport [205, 260, 268, 320]. Further research is required to understand whether this association is translatable to other disease or injury conditions.

Finally, with the biomarker findings from our previous studies, we tested whether retrograde axonal degeneration results from Aβ-induced tau pathology. Our non-invasive DTI data suggests a retrograde degeneration process follows Aβ-injection into the LGN, with early changes in the LGN and OT preceding later alterations in the ON. Histology data revealed loss of synaptic density in the injection site, as well as axon loss which correlated with DTI measures of FA and RAD in the ON, mimicking diffusional changes observed during AD [32]. Reductions in RGC density were also noted, implying that the retrograde axonal degeneration process results in later cell loss. Surprisingly, axon loss in the ON did not correlate with axonal tau pathology. This lack of association may be due to loss of affected axons or potentially to the effect of soluble tau invisible by histology. Alternatively, axon loss may be caused by a tau species which is not phosphorylated at the AT8 epitope; thus we cannot completely exclude the possible role of tau within axons to precipitate axon loss during this study.

The microtubule stabilizing compound EpoD appeared to play a neuroprotective function after Aβ injection- preventing synapse and tissue loss in the LGN as well as axon and cell loss among RGCs. In addition, this compound lowered levels of tau pathology visible in the hippocampus, similar to previous findings described by Zhang et. al.[109] Our acute Aβ injection experiments revealed that within three days of injection, visible tau pathology manifests around the injection site in the hippocampus and LGN,

preceding overt synapse and tissue loss. EpoD administration appeared to interfere with this induction of tau pathology, which may explain its downstream neuroprotective effects. These data raise the prospect that EpoD may block acute Aβ toxicity through prevention of local tau phosphorylation. It remains unclear whether the ability to prevent tau phosphoryation is related to its microtubule-stabilizing capability, though two other microtubule-stabilizing drugs (NAP and dictyostatin) also reduce tau pathology *in vivo*, suggesting a common mechanistic pathway [313, 314, 321]. The neuroprotective effects of EpoD are likely explained by this action; indeed, numerous studies have identified phospho-tau as a necessary effector downstream of Aβ to mediate neurotoxicity [59, 112, 322].

This pattern of observations hint at a sequence of events (amyloid accumulation > local tau phosphorylation > synapse loss > retrograde axonal degeneration > remote cell loss) that explain how the cardinal pathological features of AD are related to axon loss and white matter disruption visible by DTI . Integrating these observations into a model yields several testable, translational hypothesis regarding the appearance of localized amyloid/tau pathology and resulting changes in DTI metrics among connected axon tracts. This framework could be useful to interpret the effects of putative therapeutic approaches, such as those that reduce tau pathology in the brain, with changes in brain white matter microstructure. Understanding the underlying mechanisms behind axon loss and their connection to AD biomarkers will aid in developing new therapeutics and models to counteract network dysfunction and degeneration in the AD brain.

References

1. Karlawish J, Jack CR, Jr., Rocca WA, Snyder HM and Carrillo MC. Alzheimer's disease: The next frontier-Special Report 2017. *Alzheimers Dement*. 2017; 13: 374-80.

2. Sun SW, Song SK, Harms MP, et al. Detection of age-dependent brain injury in a mouse model of brain amyloidosis associated with Alzheimer's disease using magnetic resonance diffusion tensor imaging. *Exp Neurol*. 2005; 191: 77-85.

3. Zhu DC, Majumdar S, Korolev IO, Berger KL and Bozoki AC. Alzheimer's disease and amnestic mild cognitive impairment weaken connections within the default-mode network: a multi-modal imaging study. *J Alzheimers Dis*. 2013; 34: 969-84.

4. Garces P, Angel Pineda-Pardo J, Canuet L, et al. The Default Mode Network is functionally and structurally disrupted in amnestic mild cognitive impairment - a bimodal MEG-DTI study. *Neuroimage Clin*. 2014; 6: 214-21.

5. Raff MC, Whitmore AV and Finn JT. Axonal self-destruction and neurodegeneration. *Science*. 2002; 296: 868-71.

6. Schlamp CL, Li Y, Dietz JA, Janssen KT and Nickells RW. Progressive ganglion cell loss and optic nerve degeneration in DBA/2J mice is variable and asymmetric. *BMC Neurosci*. 2006; 7: 66.

7. Libby RT, Li Y, Savinova OV, et al. Susceptibility to neurodegeneration in a glaucoma is modified by Bax gene dosage. *PLoS Genet*. 2005; 1: 17-26.

8. Perry VH, Brown MC and Lunn ER. Very Slow Retrograde and Wallerian Degeneration in the CNS of C57BL/Ola Mice. *Eur J Neurosci*. 1991; 3: 102-5.

9. Coleman MP and Freeman MR. Wallerian degeneration, wld(s), and nmnat. *Annu Rev Neurosci*. 2010; 33: 245-67.

10. Deckwerth TL and Johnson EM, Jr. Neurites can remain viable after destruction of the neuronal soma by programmed cell death (apoptosis). *Dev Biol*. 1994; 165: 63-72.

11. Adalbert R, Nogradi A, Szabo A and Coleman MP. The slow Wallerian degeneration gene in vivo protects motor axons but not their cell bodies after avulsion and neonatal axotomy. *Eur J Neurosci*. 2006; 24: 2163-8.

12. Babetto E, Beirowski B, Janeckova L, et al. Targeting NMNAT1 to axons and synapses transforms its neuroprotective potency in vivo. *J Neurosci*. 2010; 30: 13291-304.

13. Conforti L, Gilley J and Coleman MP. Wallerian degeneration: an emerging axon death pathway linking injury and disease. *Nat Rev Neurosci*. 2014; 15: 394-409.

14. Osterloh JM, Yang J, Rooney TM, et al. dSarm/Sarm1 is required for activation of an injury-induced axon death pathway. *Science*. 2012; 337: 481-4.

15. Babetto E, Beirowski B, Russler EV, Milbrandt J and DiAntonio A. The Phr1 ubiquitin ligase promotes injury-induced axon self-destruction. *Cell Rep*. 2013; 3: 1422-9.

16. Nikolaev A, McLaughlin T, O'Leary DD and Tessier-Lavigne M. APP binds DR6 to trigger axon pruning and neuron death via distinct caspases. *Nature*. 2009; 457: 981-9.

17. Wang J, Zhai Q, Chen Y, et al. A local mechanism mediates NAD-dependent protection of axon degeneration. *J Cell Biol*. 2005; 170: 349-55.

18. Morfini GA, Burns M, Binder LI, et al. Axonal transport defects in neurodegenerative diseases. *J Neurosci*. 2009; 29: 12776-86.

19. Teipel SJ, Hampel H, Alexander GE, et al. Dissociation between corpus callosum atrophy and white matter pathology in Alzheimer's disease. *Neurology*. 1998; 51: 1381-5.

20. Salat DH, Kaye JA and Janowsky JS. Prefrontal gray and white matter volumes in healthy aging and Alzheimer disease. *Arch Neurol*. 1999; 56: 338-44.

21. Basser PJ, Mattiello J and LeBihan D. MR diffusion tensor spectroscopy and imaging. *Biophys J*. 1994; 66: 259-67.

22. Xie S, Xiao JX, Gong GL, et al. Voxel-based detection of white matter abnormalities in mild Alzheimer disease. *Neurology*. 2006; 66: 1845-9.

23. Albert MS, DeKosky ST, Dickson D, et al. The diagnosis of mild cognitive impairment due to Alzheimer's disease: recommendations from the National Institute on Aging-Alzheimer's Association workgroups on diagnostic guidelines for Alzheimer's disease. *Alzheimers Dement*. 2011; 7: 270-9.

24. Canu E, McLaren DG, Fitzgerald ME, et al. Microstructural diffusion changes are independent of macrostructural volume loss in moderate to severe Alzheimer's disease. *J Alzheimers Dis*. 2010; 19: 963-76.

25. Sun SW, Liang HF, Cross AH and Song SK. Evolving Wallerian degeneration after transient retinal ischemia in mice characterized by diffusion tensor imaging. *Neuroimage*. 2008; 40: 1-10.

26. Song SK, Sun SW, Ramsbottom MJ, Chang C, Russell J and Cross AH. Dysmyelination revealed through MRI as increased radial (but unchanged axial) diffusion of water. *Neuroimage*. 2002; 17: 1429-36.

27. Song SK, Sun SW, Ju WK, Lin SJ, Cross AH and Neufeld AH. Diffusion tensor imaging detects and differentiates axon and myelin degeneration in mouse optic nerve after retinal ischemia. *Neuroimage*. 2003; 20: 1714-22.

28. Sexton CE, Kalu UG, Filippini N, Mackay CE and Ebmeier KP. A meta-analysis of diffusion tensor imaging in mild cognitive impairment and Alzheimer's disease. *Neurobiol Aging*. 2011; 32: 2322 e5-18.

29. Smith SM, Jenkinson M, Johansen-Berg H, et al. Tract-based spatial statistics: voxelwise analysis of multi-subject diffusion data. *Neuroimage*. 2006; 31: 1487-505.

30. Bennett IJ, Madden DJ, Vaidya CJ, Howard DV and Howard JH, Jr. Age-related differences in multiple measures of white matter integrity: A diffusion tensor imaging study of healthy aging. *Hum Brain Mapp*. 2010; 31: 378-90.

31. Clerx L, Visser PJ, Verhey F and Aalten P. New MRI markers for Alzheimer's disease: a meta-analysis of diffusion tensor imaging and a comparison with medial temporal lobe measurements. *J Alzheimers Dis*. 2012; 29: 405-29.

32. Nir TM, Jahanshad N, Villalon-Reina JE, et al. Effectiveness of regional DTI measures in distinguishing Alzheimer's disease, MCI, and normal aging. *Neuroimage Clin*. 2013; 3: 180-95.

33. Oishi K, Akhter K, Mielke M, et al. Multi-modal MRI analysis with disease-specific spatial filtering: initial testing to predict mild cognitive impairment patients who convert to Alzheimer's disease. *Front Neurol*. 2011; 2: 54.

34. Fletcher E, Raman M, Huebner P, et al. Loss of fornix white matter volume as a predictor of cognitive impairment in cognitively normal elderly individuals. *JAMA Neurol*. 2013; 70: 1389-95.

35. Defrancesco M, Egger K, Marksteiner J, et al. Changes in white matter integrity before conversion from mild cognitive impairment to Alzheimer's disease. *PLoS One*. 2014; 9: e106062.

36. Stenset V, Bjornerud A, Fjell AM, et al. Cingulum fiber diffusivity and CSF T-tau in patients with subjective and mild cognitive impairment. *Neurobiol Aging*. 2011; 32: 581-9.

37. Almdahl IS, Lauridsen C, Selnes P, et al. Cerebrospinal Fluid Levels of Amyloid Beta 1-43 Mirror 1-42 in Relation to Imaging Biomarkers of Alzheimer's Disease. *Front Aging Neurosci*. 2017; 9: 9.

38. Bendlin BB, Carlsson CM, Johnson SC, et al. CSF T-Tau/Abeta42 predicts white matter microstructure in healthy adults at risk for Alzheimer's disease. *PLoS One*. 2012; 7: e37720.

39. Kantarci K, Schwarz CG, Reid RI, et al. White matter integrity determined with diffusion tensor imaging in older adults without dementia: influence of amyloid load and neurodegeneration. *JAMA Neurol*. 2014; 71: 1547-54.

40. Kantarci K, Murray ME, Schwarz CG, et al. White-matter integrity on DTI and the pathologic staging of Alzheimer's disease. *Neurobiol Aging*. 2017; 56: 172-9.

41. Shepherd C, McCann H and Halliday GM. Variations in the neuropathology of familial Alzheimer's disease. *Acta Neuropathol*. 2009; 118: 37-52.

42. Johnson KA, Sperling RA, Gidicsin CM, et al. Florbetapir (F18-AV-45) PET to assess amyloid burden in Alzheimer's disease dementia, mild cognitive impairment, and normal aging. *Alzheimers Dement*. 2013; 9: S72-83.

43. Doraiswamy PM, Sperling RA, Johnson K, et al. Florbetapir F 18 amyloid PET and 36-month cognitive decline: a prospective multicenter study. *Mol Psychiatry*. 2014; 19: 1044-51.

44. Lim YY, Maruff P, Pietrzak RH, et al. Effect of amyloid on memory and non-memory decline from preclinical to clinical Alzheimer's disease. *Brain*. 2014; 137: 221-31.

45. Giannakopoulos P, Herrmann FR, Bussiere T, et al. Tangle and neuron numbers, but not amyloid load, predict cognitive status in Alzheimer's disease. *Neurology*. 2003; 60: 1495-500.

46. Terry RD, Masliah E, Salmon DP, et al. Physical basis of cognitive alterations in Alzheimer's disease: synapse loss is the major correlate of cognitive impairment. *Ann Neurol*. 1991; 30: 572-80.

47. Guillozet AL, Weintraub S, Mash DC and Mesulam MM. Neurofibrillary tangles, amyloid, and memory in aging and mild cognitive impairment. *Arch Neurol*. 2003; 60: 729-36.

48. Karran E and De Strooper B. The amyloid cascade hypothesis: are we poised for success or failure? *J Neurochem*. 2016; 139 Suppl 2: 237-52.

49. Nelson PT, Alafuzoff I, Bigio EH, et al. Correlation of Alzheimer disease neuropathologic changes with cognitive status: a review of the literature. *J Neuropathol Exp Neurol*. 2012; 71: 362-81.

50. Gomez-Isla T, Hollister R, West H, et al. Neuronal loss correlates with but exceeds neurofibrillary tangles in Alzheimer's disease. *Ann Neurol*. 1997; 41: 17-24.

51. Trojanowski JQ, Schuck T, Schmidt ML and Lee VM. Distribution of tau proteins in the normal human central and peripheral nervous system. *J Histochem Cytochem*. 1989; 37: 209-15.

52. Goedert M, Spillantini MG, Jakes R, Rutherford D and Crowther RA. Multiple isoforms of human microtubule-associated protein tau: sequences and localization in neurofibrillary tangles of Alzheimer's disease. *Neuron*. 1989; 3: 519-26.

53. Mandelkow EM, Schweers O, Drewes G, et al. Structure, microtubule interactions, and phosphorylation of tau protein. *Ann N Y Acad Sci*. 1996; 777: 96-106.

54. Wang JZ, Xia YY, Grundke-Iqbal I and Iqbal K. Abnormal hyperphosphorylation of tau: sites, regulation, and molecular mechanism of neurofibrillary degeneration. *J Alzheimers Dis*. 2013; 33 Suppl 1: S123-39.

55. Kopke E, Tung YC, Shaikh S, Alonso AC, Iqbal K and Grundke-Iqbal I. Microtubule-associated protein tau. Abnormal phosphorylation of a non-paired helical filament pool in Alzheimer disease. *J Biol Chem*. 1993; 268: 24374-84.

56. Takemura R, Okabe S, Umeyama T, Kanai Y, Cowan NJ and Hirokawa N. Increased microtubule stability and alpha tubulin acetylation in cells transfected with microtubule-associated proteins MAP1B, MAP2 or tau. *J Cell Sci*. 1992; 103 (Pt 4): 953-64.

57. Esmaeli-Azad B, McCarty JH and Feinstein SC. Sense and antisense transfection analysis of tau function: tau influences net microtubule assembly, neurite outgrowth and neuritic stability. *J Cell Sci*. 1994; 107 (Pt 4): 869-79.

58. Kadavath H, Hofele RV, Biernat J, et al. Tau stabilizes microtubules by binding at the interface between tubulin heterodimers. *Proc Natl Acad Sci U S A*. 2015; 112: 7501-6.

59. Morris M, Maeda S, Vossel K and Mucke L. The many faces of tau. *Neuron*. 2011; 70: 410-26.

60. Hutton M, Lendon CL, Rizzu P, et al. Association of missense and 5'-splice-site mutations in tau with the inherited dementia FTDP-17. *Nature*. 1998; 393: 702-5.

61. Lewis J, McGowan E, Rockwood J, et al. Neurofibrillary tangles, amyotrophy and progressive motor disturbance in mice expressing mutant (P301L) tau protein. *Nat Genet*. 2000; 25: 402-5.

62. Duff K, Knight H, Refolo LM, et al. Characterization of pathology in transgenic mice over-expressing human genomic and cDNA tau transgenes. *Neurobiol Dis*. 2000; 7: 87-98.

63. Lovestone S, Hartley CL, Pearce J and Anderton BH. Phosphorylation of tau by glycogen synthase kinase-3 beta in intact mammalian cells: the effects on the organization and stability of microtubules. *Neuroscience*. 1996; 73: 1145-57.

64. Lucas JJ, Hernandez F, Gomez-Ramos P, Moran MA, Hen R and Avila J. Decreased nuclear beta-catenin, tau hyperphosphorylation and neurodegeneration in GSK-3beta conditional transgenic mice. *EMBO J*. 2001; 20: 27-39.

65. Iqbal K, Alonso Adel C, Chen S, et al. Tau pathology in Alzheimer disease and other tauopathies. *Biochim Biophys Acta*. 2005; 1739: 198-210.

66. Noble W, Olm V, Takata K, et al. Cdk5 is a key factor in tau aggregation and tangle formation in vivo. *Neuron*. 2003; 38: 555-65.

67. Scott CW, Spreen RC, Herman JL, et al. Phosphorylation of recombinant tau by cAMP-dependent protein kinase. Identification of phosphorylation sites and effect on microtubule assembly. *J Biol Chem*. 1993; 268: 1166-73.

68. Lewis J, Dickson DW, Lin WL, et al. Enhanced neurofibrillary degeneration in transgenic mice expressing mutant tau and APP. *Science*. 2001; 293: 1487-91.

69. Gotz J, Chen F, van Dorpe J and Nitsch RM. Formation of neurofibrillary tangles in P301l tau transgenic mice induced by Abeta 42 fibrils. *Science*. 2001; 293: 1491-5.

70. Domise M, Didier S, Marinangeli C, et al. AMP-activated protein kinase modulates tau phosphorylation and tau pathology in vivo. *Sci Rep*. 2016; 6: 26758.

71. Song SK, Kim JH, Lin SJ, Brendza RP and Holtzman DM. Diffusion tensor imaging detects age-dependent white matter changes in a transgenic mouse model with amyloid deposition. *Neurobiol Dis*. 2004; 15: 640-7.

72. Keller JN, Hanni KB and Markesbery WR. Impaired proteasome function in Alzheimer's disease. *J Neurochem*. 2000; 75: 436-9.

73. Keck S, Nitsch R, Grune T and Ullrich O. Proteasome inhibition by paired helical filament-tau in brains of patients with Alzheimer's disease. *J Neurochem*. 2003; 85: 115-22.

74. Kovacech B, Skrabana R and Novak M. Transition of tau protein from disordered to misordered in Alzheimer's disease. *Neurodegener Dis*. 2010; 7: 24-7.

75. DeVos SL, Corjuc BT, Oakley DH, et al. Synaptic Tau Seeding Precedes Tau Pathology in Human Alzheimer's Disease Brain. *Front Neurosci*. 2018; 12: 267.

76. Braak H, Thal DR, Ghebremedhin E and Del Tredici K. Stages of the pathologic process in Alzheimer disease: age categories from 1 to 100 years. *J Neuropathol Exp Neurol*. 2011; 70: 960-9.

77. Hyman BT, Phelps CH, Beach TG, et al. National Institute on Aging-Alzheimer's Association guidelines for the neuropathologic assessment of Alzheimer's disease. *Alzheimers Dement*. 2012; 8: 1-13.

78. Sanders DW, Kaufman SK, DeVos SL, et al. Distinct tau prion strains propagate in cells and mice and define different tauopathies. *Neuron*. 2014; 82: 1271-88.

79. Stancu IC, Vasconcelos B, Terwel D and Dewachter I. Models of beta-amyloid induced Tau-pathology: the long and "folded" road to understand the mechanism. *Mol Neurodegener*. 2014; 9: 51.

80. de Calignon A, Polydoro M, Suarez-Calvet M, et al. Propagation of tau pathology in a model of early Alzheimer's disease. *Neuron*. 2012; 73: 685-97.

81. Pickett EK, Henstridge CM, Allison E, et al. Spread of tau down neural circuits precedes synapse and neuronal loss in the rTgTauEC mouse model of early Alzheimer's disease. *Synapse*. 2017; 71.

82. Yanamandra K, Kfoury N, Jiang H, et al. Anti-tau antibodies that block tau aggregate seeding in vitro markedly decrease pathology and improve cognition in vivo. *Neuron*. 2013; 80: 402-14.

83. Ahnaou A, Moechars D, Raeymaekers L, et al. Emergence of early alterations in network oscillations and functional connectivity in a tau seeding mouse model of Alzheimer's disease pathology. *Sci Rep*. 2017; 7: 14189.

84. Gilley J and Coleman MP. Endogenous Nmnat2 is an essential survival factor for maintenance of healthy axons. *PLoS Biol*. 2010; 8: e1000300.

85. Millecamps S and Julien JP. Axonal transport deficits and neurodegenerative diseases. *Nat Rev Neurosci*. 2013; 14: 161-76.

86. Hafezparast M, Klocke R, Ruhrberg C, et al. Mutations in dynein link motor neuron degeneration to defects in retrograde transport. *Science*. 2003; 300: 808-12.

87. Reid E, Kloos M, Ashley-Koch A, et al. A kinesin heavy chain (KIF5A) mutation in hereditary spastic paraplegia (SPG10). *Am J Hum Genet*. 2002; 71: 1189-94.

88. Kanaan NM, Morfini GA, LaPointe NE, et al. Pathogenic forms of tau inhibit kinesin-dependent axonal transport through a mechanism involving activation of axonal phosphotransferases. *J Neurosci*. 2011; 31: 9858-68.

89. Cras P, Kawai M, Lowery D, Gonzalez-DeWhitt P, Greenberg B and Perry G. Senile plaque neurites in Alzheimer disease accumulate amyloid precursor protein. *Proc Natl Acad Sci U S A*. 1991; 88: 7552-6.

90. Burke WJ, Park DH, Chung HD, Marshall GL, Haring JH and Joh TH. Evidence for decreased transport of tryptophan hydroxylase in Alzheimer's disease. *Brain Res*. 1990; 537: 83-7.

91. Bertrand A, Khan U, Hoang DM, et al. Non-invasive, in vivo monitoring of neuronal transport impairment in a mouse model of tauopathy using MEMRI. *Neuroimage*. 2013; 64: 693-702.

92. Smith KD, Paylor R and Pautler RG. R-flurbiprofen improves axonal transport in the Tg2576 mouse model of Alzheimer's disease as determined by MEMRI. *Magn Reson Med*. 2011; 65: 1423-9.

93. Kim J, Choi IY, Michaelis ML and Lee P. Quantitative in vivo measurement of early axonal transport deficits in a triple transgenic mouse model of Alzheimer's disease using manganese-enhanced MRI. *Neuroimage*. 2011; 56: 1286-92.

94. Majid T, Ali YO, Venkitaramani DV, Jang MK, Lu HC and Pautler RG. In vivo axonal transport deficits in a mouse model of fronto-temporal dementia. *Neuroimage Clin*. 2014; 4: 711-7.

95. Vossel KA, Zhang K, Brodbeck J, et al. Tau reduction prevents Abeta-induced defects in axonal transport. *Science*. 2010; 330: 198.

96. Vossel KA, Xu JC, Fomenko V, et al. Tau reduction prevents Abeta-induced axonal transport deficits by blocking activation of GSK3beta. *J Cell Biol*. 2015; 209: 419-33.

97. Ittner LM, Ke YD and Gotz J. Phosphorylated Tau interacts with c-Jun N-terminal kinase-interacting protein 1 (JIP1) in Alzheimer disease. *J Biol Chem*. 2009; 284: 20909-16.

98. Morfini G, Szebenyi G, Brown H, et al. A novel CDK5-dependent pathway for regulating GSK3 activity and kinesin-driven motility in neurons. *EMBO J*. 2004; 23: 2235-45.

99. Kanaan NM, Pigino GF, Brady ST, Lazarov O, Binder LI and Morfini GA. Axonal degeneration in Alzheimer's disease: when signaling abnormalities meet the axonal transport system. *Exp Neurol*. 2013; 246: 44-53.

100. Ishihara T, Zhang B, Higuchi M, Yoshiyama Y, Trojanowski JQ and Lee VM. Age-dependent induction of congophilic neurofibrillary tau inclusions in tau transgenic mice. *Am J Pathol*. 2001; 158: 555-62.

101. Brunden KR, Zhang B, Carroll J, et al. Epothilone D improves microtubule density, axonal integrity, and cognition in a transgenic mouse model of tauopathy. *J Neurosci*. 2010; 30: 13861-6.

102. Cash AD, Aliev G, Siedlak SL, et al. Microtubule reduction in Alzheimer's disease and aging is independent of tau filament formation. *Am J Pathol*. 2003; 162: 1623-7.

103. Barten DM, Fanara P, Andorfer C, et al. Hyperdynamic microtubules, cognitive deficits, and pathology are improved in tau transgenic mice with low doses of the microtubule-stabilizing agent BMS-241027. *J Neurosci*. 2012; 32: 7137-45.

104. Harada A, Oguchi K, Okabe S, et al. Altered microtubule organization in small-calibre axons of mice lacking tau protein. *Nature*. 1994; 369: 488-91.

105. Dawson HN, Ferreira A, Eyster MV, Ghoshal N, Binder LI and Vitek MP. Inhibition of neuronal maturation in primary hippocampal neurons from tau deficient mice. *J Cell Sci*. 2001; 114: 1179-87.

106. Zhang B, Maiti A, Shively S, et al. Microtubule-binding drugs offset tau sequestration by stabilizing microtubules and reversing fast axonal transport deficits in a tauopathy model. *Proc Natl Acad Sci U S A*. 2005; 102: 227-31.

107. Brunden KR, Yao Y, Potuzak JS, et al. The characterization of microtubule-stabilizing drugs as possible therapeutic agents for Alzheimer's disease and related tauopathies. *Pharmacol Res*. 2011; 63: 341-51.

108. Penazzi L, Tackenberg C, Ghori A, et al. Abeta-mediated spine changes in the hippocampus are microtubule-dependent and can be reversed by a subnanomolar concentration of the microtubule-stabilizing agent epothilone D. *Neuropharmacology*. 2016; 105: 84-95.

109. Zhang B, Carroll J, Trojanowski JQ, et al. The microtubule-stabilizing agent, epothilone D, reduces axonal dysfunction, neurotoxicity, cognitive deficits, and Alzheimer-like pathology in an interventional study with aged tau transgenic mice. *J Neurosci*. 2012; 32: 3601-11.

110. Fein JA, Sokolow S, Miller CA, et al. Co-localization of amyloid beta and tau pathology in Alzheimer's disease synaptosomes. *Am J Pathol*. 2008; 172: 1683-92.

111. Zempel H, Thies E, Mandelkow E and Mandelkow EM. Abeta oligomers cause localized Ca(2+) elevation, missorting of endogenous Tau into dendrites, Tau phosphorylation, and destruction of microtubules and spines. *J Neurosci*. 2010; 30: 11938-50.

112. Ittner LM, Ke YD, Delerue F, et al. Dendritic function of tau mediates amyloid-beta toxicity in Alzheimer's disease mouse models. *Cell*. 2010; 142: 387-97.

113. Riccomagno MM and Kolodkin AL. Sculpting neural circuits by axon and dendrite pruning. *Annu Rev Cell Dev Biol*. 2015; 31: 779-805.

114. Shu X, Qin YY, Zhang S, et al. Voxel-based diffusion tensor imaging of an APP/PS1 mouse model of Alzheimer's disease. *Mol Neurobiol*. 2013; 48: 78-83.

115. Wiesmann M, Zerbi V, Jansen D, et al. Hypertension, cerebrovascular impairment, and cognitive decline in aged AbetaPP/PS1 mice. *Theranostics*. 2017; 7: 1277-89.

116. Sahara N, Perez PD, Lin WL, et al. Age-related decline in white matter integrity in a mouse model of tauopathy: an in vivo diffusion tensor magnetic resonance imaging study. *Neurobiol Aging*. 2014; 35: 1364-74.

117. Wells JA, O'Callaghan JM, Holmes HE, et al. In vivo imaging of tau pathology using multi-parametric quantitative MRI. *Neuroimage*. 2015; 111: 369-78.

118. Kastyak-Ibrahim MZ, Di Curzio DL, Buist R, et al. Neurofibrillary tangles and plaques are not accompanied by white matter pathology in aged triple transgenic-Alzheimer disease mice. *Magn Reson Imaging*. 2013; 31: 1515-21.

119. Badea A, Kane L, Anderson RJ, et al. The fornix provides multiple biomarkers to characterize circuit disruption in a mouse model of Alzheimer's disease. *Neuroimage*. 2016; 142: 498-511.

120. Colgan N, Siow B, O'Callaghan JM, et al. Application of neurite orientation dispersion and density imaging (NODDI) to a tau pathology model of Alzheimer's disease. *Neuroimage*. 2016; 125: 739-44.

121. Fischer MD, Huber G, Beck SC, et al. Noninvasive, in vivo assessment of mouse retinal structure using optical coherence tomography. *PLoS One*. 2009; 4: e7507.

122. Petzold A, de Boer JF, Schippling S, et al. Optical coherence tomography in multiple sclerosis: a systematic review and meta-analysis. *Lancet Neurol*. 2010; 9: 921-32.

123. Guedes V, Schuman JS, Hertzmark E, et al. Optical coherence tomography measurement of macular and nerve fiber layer thickness in normal and glaucomatous human eyes. *Ophthalmology*. 2003; 110: 177-89.

124. Kesler A, Vakhapova V, Korczyn AD, Naftaliev E and Neudorfer M. Retinal thickness in patients with mild cognitive impairment and Alzheimer's disease. *Clin Neurol Neurosurg*. 2011; 113: 523-6.

125. Kromer R, Serbecic N, Hausner L, Froelich L, Aboul-Enein F and Beutelspacher SC. Detection of Retinal Nerve Fiber Layer Defects in Alzheimer's Disease Using SD-OCT. *Front Psychiatry*. 2014; 5: 22.

126. Paquet C, Boissonnot M, Roger F, Dighiero P, Gil R and Hugon J. Abnormal retinal thickness in patients with mild cognitive impairment and Alzheimer's disease. *Neurosci Lett*. 2007; 420: 97-9.

127. Sun SW, Liang HF, Schmidt RE, Cross AH and Song SK. Selective vulnerability of cerebral white matter in a murine model of multiple sclerosis detected using diffusion tensor imaging. *Neurobiol Dis*. 2007; 28: 30-8.

128. Wu Q, Butzkueven H, Gresle M, et al. MR diffusion changes correlate with ultra-structurally defined axonal degeneration in murine optic nerve. *Neuroimage*. 2007; 37: 1138-47.

129. Yankner BA and Mesulam MM. Seminars in medicine of the Beth Israel Hospital, Boston. beta-Amyloid and the pathogenesis of Alzheimer's disease. *N Engl J Med*. 1991; 325: 1849-57.

130. Risacher SL and Saykin AJ. Neuroimaging and other biomarkers for Alzheimer's disease: the changing landscape of early detection. *Annu Rev Clin Psychol*. 2013; 9: 621-48.

131. Douaud G, Jbabdi S, Behrens TE, et al. DTI measures in crossing-fibre areas: increased diffusion anisotropy reveals early white matter alteration in MCI and mild Alzheimer's disease. *Neuroimage*. 2011; 55: 880-90.

132. Rowley J, Fonov V, Wu O, et al. White matter abnormalities and structural hippocampal disconnections in amnestic mild cognitive impairment and Alzheimer's disease. *PLoS One*. 2013; 8: e74776.

133. Agosta F, Pievani M, Sala S, et al. White matter damage in Alzheimer disease and its relationship to gray matter atrophy. *Radiology*. 2011; 258: 853-63.

134. Bozzali M, Falini A, Franceschi M, et al. White matter damage in Alzheimer's disease assessed in vivo using diffusion tensor magnetic resonance imaging. *J Neurol Neurosurg Psychiatry*. 2002; 72: 742-6.

135. Medina D, DeToledo-Morrell L, Urresta F, et al. White matter changes in mild cognitive impairment and AD: A diffusion tensor imaging study. *Neurobiol Aging*. 2006; 27: 663-72.

136. Streilein JW. Ocular immune privilege: therapeutic opportunities from an experiment of nature. *Nat Rev Immunol*. 2003; 3: 879-89.

137. Mendez MF, Mendez MA, Martin R, Smyth KA and Whitehouse PJ. Complex visual disturbances in Alzheimer's disease. *Neurology*. 1990; 40: 439-43.

138. Cronin-Golomb A, Corkin S, Rizzo JF, Cohen J, Growdon JH and Banks KS. Visual dysfunction in Alzheimer's disease: relation to normal aging. *Ann Neurol*. 1991; 29: 41-52.

139. Frisoni GB, Fox NC, Jack CR, Jr., Scheltens P and Thompson PM. The clinical use of structural MRI in Alzheimer disease. *Nat Rev Neurol*. 2010; 6: 67-77.

140. Frisoni GB, Pievani M, Testa C, et al. The topography of grey matter involvement in early and late onset Alzheimer's disease. *Brain*. 2007; 130: 720-30.

141. Pearson RC, Esiri MM, Hiorns RW, Wilcock GK and Powell TP. Anatomical correlates of the distribution of the pathological changes in the neocortex in Alzheimer disease. *Proc Natl Acad Sci U S A*. 1985; 82: 4531-4.

142. Pierpaoli C, Jezzard P, Basser PJ, Barnett A and Di Chiro G. Diffusion tensor MR imaging of the human brain. *Radiology*. 1996; 201: 637-48.

143. Sun SW, Liang HF, Trinkaus K, Cross AH, Armstrong RC and Song SK. Noninvasive detection of cuprizone induced axonal damage and demyelination in the mouse corpus callosum. *Magn Reson Med*. 2006; 55: 302-8.

144. Sun SW, Liang HF, Mei J, Xu D and Shi WX. In vivo diffusion tensor imaging of amyloid-beta-induced white matter damage in mice. *J Alzheimers Dis*. 2014; 38: 93-101.

145. Song SK, Yoshino J, Le TQ, et al. Demyelination increases radial diffusivity in corpus callosum of mouse brain. *Neuroimage*. 2005; 26: 132-40.

146. Zhuang L, Sachdev PS, Trollor JN, et al. Microstructural white matter changes, not hippocampal atrophy, detect early amnestic mild cognitive impairment. *PLoS One*. 2013; 8: e58887.

147. Cho H, Yang DW, Shon YM, et al. Abnormal integrity of corticocortical tracts in mild cognitive impairment: a diffusion tensor imaging study. *J Korean Med Sci*. 2008; 23: 477-83.

148. Oguz I, Farzinfar M, Matsui J, et al. DTIPrep: quality control of diffusion-weighted images. *Frontiers in neuroinformatics*. 2014; 8: 4.

149. Trick GL, Trick LR, Morris P and Wolf M. Visual field loss in senile dementia of the Alzheimer's type. *Neurology*. 1995; 45: 68-74.

150. Fotiou DF, Brozou CG, Haidich AB, et al. Pupil reaction to light in Alzheimer's disease: evaluation of pupil size changes and mobility. *Aging Clin Exp Res*. 2007; 19: 364-71.

151. Mendola JD, Cronin-Golomb A, Corkin S and Growdon JH. Prevalence of visual deficits in Alzheimer's disease. *Optom Vis Sci*. 1995; 72: 155-67.

152. Crutch SJ, Lehmann M, Schott JM, Rabinovici GD, Rossor MN and Fox NC. Posterior cortical atrophy. *Lancet Neurol*. 2012; 11: 170-8.

153. Minoshima S, Giordani B, Berent S, Frey KA, Foster NL and Kuhl DE. Metabolic reduction in the posterior cingulate cortex in very early Alzheimer's disease. *Ann Neurol*. 1997; 42: 85-94.

154. Blanks JC, Torigoe Y, Hinton DR and Blanks RH. Retinal pathology in Alzheimer's disease. I. Ganglion cell loss in foveal/parafoveal retina. *Neurobiol Aging*. 1996; 17: 377-84.

155. Hinton DR, Sadun AA, Blanks JC and Miller CA. Optic-nerve degeneration in Alzheimer's disease. *N Engl J Med*. 1986; 315: 485-7.

156. Fujimoto JG, Pitris C, Boppart SA and Brezinski ME. Optical coherence tomography: an emerging technology for biomedical imaging and optical biopsy. *Neoplasia*. 2000; 2: 9-25.

157. Parisi V, Restuccia R, Fattapposta F, Mina C, Bucci MG and Pierelli F. Morphological and functional retinal impairment in Alzheimer's disease patients. *Clin Neurophysiol*. 2001; 112: 1860-7.

158. Hui ES, Fu QL, So KF and Wu EX. Diffusion tensor MR study of optic nerve degeneration in glaucoma. *Conf Proc IEEE Eng Med Biol Soc*. 2007; 2007: 4312-5.

159. Schmierer K, Wheeler-Kingshott CA, Boulby PA, et al. Diffusion tensor imaging of post mortem multiple sclerosis brain. *Neuroimage*. 2007; 35: 467-77.

160. Diniz BS, Pinto Junior JA and Forlenza OV. Do CSF total tau, phosphorylated tau, and beta-amyloid 42 help to predict progression of mild cognitive impairment to Alzheimer's disease? A systematic review and meta-analysis of the literature. *World J Biol Psychiatry*. 2008; 9: 172-82.

161. Shu N, Liang Y, Li H, et al. Disrupted topological organization in white matter structural networks in amnestic mild cognitive impairment: relationship to subtype. *Radiology*. 2012; 265: 518-27.

162. Coleman MP and Perry VH. Axon pathology in neurological disease: a neglected therapeutic target. *Trends Neurosci*. 2002; 25: 532-7.

163. Coleman M. Axon degeneration mechanisms: commonality amid diversity. *Nat Rev Neurosci*. 2005; 6: 889-98.

164. Ozturk G, Cengiz N, Erdogan E, et al. Two distinct types of dying back axonal degeneration in vitro. *Neuropathol Appl Neurobiol*. 2013; 39: 362-76.

165. George R and Griffin JW. Delayed macrophage responses and myelin clearance during Wallerian degeneration in the central nervous system: the dorsal radiculotomy model. *Exp Neurol*. 1994; 129: 225-36.

166. Vargas ME and Barres BA. Why is Wallerian degeneration in the CNS so slow? *Annu Rev Neurosci*. 2007; 30: 153-79.

167. Nishioka C, Poh C and Sun SW. Diffusion tensor imaging reveals visual pathway damage in patients with mild cognitive impairment and Alzheimer's disease. *J Alzheimers Dis*. 2015; 45: 97-107.

168. Thomalla G, Glauche V, Koch MA, Beaulieu C, Weiller C and Rother J. Diffusion tensor imaging detects early Wallerian degeneration of the pyramidal tract after ischemic stroke. *Neuroimage*. 2004; 22: 1767-74.

169. Thomalla G, Glauche V, Weiller C and Rother J. Time course of wallerian degeneration after ischaemic stroke revealed by diffusion tensor imaging. *J Neurol Neurosurg Psychiatry*. 2005; 76: 266-8.

170. Pierpaoli C, Barnett A, Pajevic S, et al. Water diffusion changes in Wallerian degeneration and their dependence on white matter architecture. *Neuroimage*. 2001; 13: 1174-85.

171. Werring DJ, Toosy AT, Clark CA, et al. Diffusion tensor imaging can detect and quantify corticospinal tract degeneration after stroke. *J Neurol Neurosurg Psychiatry*. 2000; 69: 269-72.

172. Bjartmar C, Kidd G, Mork S, Rudick R and Trapp BD. Neurological disability correlates with spinal cord axonal loss and reduced N-acetyl aspartate in chronic multiple sclerosis patients. *Ann Neurol*. 2000; 48: 893-901.

173. Gonzalez-Scarano F, Grossman RI, Galetta S, Atlas SW and Silberberg DH. Multiple sclerosis disease activity correlates with gadolinium-enhanced magnetic resonance imaging. *Ann Neurol*. 1987; 21: 300-6.

174. McDonald WI, Compston A, Edan G, et al. Recommended diagnostic criteria for multiple sclerosis: guidelines from the International Panel on the diagnosis of multiple sclerosis. *Ann Neurol*. 2001; 50: 121-7.

175. Polman CH, Reingold SC, Banwell B, et al. Diagnostic criteria for multiple sclerosis: 2010 revisions to the McDonald criteria. *Ann Neurol*. 2011; 69: 292-302.

176. Trapp BD, Peterson J, Ransohoff RM, Rudick R, Mork S and Bo L. Axonal transection in the lesions of multiple sclerosis. *N Engl J Med*. 1998; 338: 278-85.

177. Kornek B, Storch MK, Weissert R, et al. Multiple sclerosis and chronic autoimmune encephalomyelitis: a comparative quantitative study of axonal injury in active, inactive, and remyelinated lesions. *Am J Pathol*. 2000; 157: 267-76.

178. Roosendaal SD, Geurts JJ, Vrenken H, et al. Regional DTI differences in multiple sclerosis patients. *Neuroimage*. 2009; 44: 1397-403.

179. Be'eri H, Reichert F, Saada A and Rotshenker S. The cytokine network of wallerian degeneration: IL-10 and GM-CSF. *Eur J Neurosci*. 1998; 10: 2707-13.

180. Shamash S, Reichert F and Rotshenker S. The cytokine network of Wallerian degeneration: tumor necrosis factor-alpha, interleukin-1alpha, and interleukin-1beta. *J Neurosci*. 2002; 22: 3052-60.

181. Ciccarelli O, Werring DJ, Barker GJ, et al. A study of the mechanisms of normal-appearing white matter damage in multiple sclerosis using diffusion tensor imaging--evidence of Wallerian degeneration. *J Neurol*. 2003; 250: 287-92.

182. Avellino AM, Hart D, Dailey AT, MacKinnon M, Ellegala D and Kliot M. Differential macrophage responses in the peripheral and central nervous system during wallerian degeneration of axons. *Exp Neurol*. 1995; 136: 183-98.

183. Xie M, Wang Q, Wu TH, Song SK and Sun SW. Delayed axonal degeneration in slow Wallerian degeneration mutant mice detected using diffusion tensor imaging. *Neuroscience*. 2011; 197: 339-47.

184. Sun SW, Liang HF, Le TQ, Armstrong RC, Cross AH and Song SK. Differential sensitivity of in vivo and ex vivo diffusion tensor imaging to evolving optic nerve injury in mice with retinal ischemia. *Neuroimage*. 2006; 32: 1195-204.

185. Sun SW, Mei J and Tuel K. Comparison of mouse brain DTI maps using K-space average, image-space average, or no average approach. *Magn Reson Imaging*. 2013; 31: 1532-6.

186. Mulkern RV, Wong ST, Winalski C and Jolesz FA. Contrast manipulation and artifact assessment of 2D and 3D RARE sequences. *Magn Reson Imaging*. 1990; 8: 557-66.

187. Sun SW, Nishioka C, Labib W and Liang HF. Axonal Terminals Exposed to Amyloid-beta May Not Lead to Pre-Synaptic Axonal Damage. *J Alzheimers Dis*. 2015; 45: 1139-48.

188. Sun SW, Liang HF, Xie M, Oyoyo U and Lee A. Fixation, not death, reduces sensitivity of DTI in detecting optic nerve damage. *Neuroimage*. 2009; 44: 611-9.

189. Kuhn MJ, Mikulis DJ, Ayoub DM, Kosofsky BE, Davis KR and Taveras JM. Wallerian degeneration after cerebral infarction: evaluation with sequential MR imaging. *Radiology*. 1989; 172: 179-82.

190. Karlsborg M, Rosenbaum S, Wiegell M, et al. Corticospinal tract degeneration and possible pathogenesis in ALS evaluated by MR diffusion tensor imaging. *Amyotroph Lateral Scler Other Motor Neuron Disord*. 2004; 5: 136-40.

191. Moll NM, Rietsch AM, Thomas S, et al. Multiple sclerosis normal-appearing white matter: pathology-imaging correlations. *Ann Neurol*. 2011; 70: 764-73.

192. De Groot CJ, Bergers E, Kamphorst W, et al. Post-mortem MRI-guided sampling of multiple sclerosis brain lesions: increased yield of active demyelinating and (p)reactive lesions. *Brain*. 2001; 124: 1635-45.

193. Gabay C and Kushner I. Acute-phase proteins and other systemic responses to inflammation. *N Engl J Med*. 1999; 340: 448-54.

194. Kobayashi N, Nagai H, Yasuda Y and Kanazawa K. The early influence of albumin administration on protein metabolism and wound healing in burned rats. *Wound Repair Regen*. 2004; 12: 109-14.

195. Lazar DA, Ellegala DB, Avellino AM, Dailey AT, Andrus K and Kliot M. Modulation of macrophage and microglial responses to axonal injury in the peripheral and central nervous systems. *Neurosurgery*. 1999; 45: 593-600.

196. Beirowski B, Adalbert R, Wagner D, et al. The progressive nature of Wallerian degeneration in wild-type and slow Wallerian degeneration (WldS) nerves. *BMC Neurosci*. 2005; 6: 6.

197. Sun SW, Song SK, Hong CY, Chu WC and Chang C. Directional correlation characterization and classification of white matter tracts. *Magn Reson Med*. 2003; 49: 271-5.

198. Friese MA, Schattling B and Fugger L. Mechanisms of neurodegeneration and axonal dysfunction in multiple sclerosis. *Nat Rev Neurol*. 2014; 10: 225-38.

199. Barkhof F. The clinico-radiological paradox in multiple sclerosis revisited. *Curr Opin Neurol*. 2002; 15: 239-45.

200. Ikuta F and Zimmerman HM. Distribution of plaques in seventy autopsy cases of multiple sclerosis in the United States. *Neurology*. 1976; 26: 26-8.

201. Toussaint D, Perier O, Verstappen A and Bervoets S. Clinicopathological study of the visual pathways, eyes, and cerebral hemispheres in 32 cases of disseminated sclerosis. *J Clin Neuroophthalmol*. 1983; 3: 211-20.

202. Budde MD and Frank JA. Neurite beading is sufficient to decrease the apparent diffusion coefficient after ischemic stroke. *Proc Natl Acad Sci U S A*. 2010; 107: 14472-7.

203. DeBoy CA, Zhang J, Dike S, et al. High resolution diffusion tensor imaging of axonal damage in focal inflammatory and demyelinating lesions in rat spinal cord. *Brain*. 2007; 130: 2199-210.

204. Budde MD, Kim JH, Liang HF, Russell JH, Cross AH and Song SK. Axonal injury detected by in vivo diffusion tensor imaging correlates with neurological disability in a mouse model of multiple sclerosis. *NMR Biomed*. 2008; 21: 589-97.

205. Kolbe S, Chapman C, Nguyen T, et al. Optic nerve diffusion changes and atrophy jointly predict visual dysfunction after optic neuritis. *Neuroimage*. 2009; 45: 679-86.

206. Saidha S, Al-Louzi O, Ratchford JN, et al. Optical coherence tomography reflects brain atrophy in multiple sclerosis: A four-year study. *Ann Neurol*. 2015; 78: 801-13.

207. Saidha S, Sotirchos ES, Oh J, et al. Relationships between retinal axonal and neuronal measures and global central nervous system pathology in multiple sclerosis. *JAMA Neurol*. 2013; 70: 34-43.

208. Gordon-Lipkin E, Chodkowski B, Reich DS, et al. Retinal nerve fiber layer is associated with brain atrophy in multiple sclerosis. *Neurology*. 2007; 69: 1603-9.

209. Abalo-Lojo JM, Limeres CC, Gomez MA, et al. Retinal nerve fiber layer thickness, brain atrophy, and disability in multiple sclerosis patients. *J Neuroophthalmol*. 2014; 34: 23-8.

210. Albrecht P, Frohlich R, Hartung HP, Kieseier BC and Methner A. Optical coherence tomography measures axonal loss in multiple sclerosis independently of optic neuritis. *J Neurol*. 2007; 254: 1595-6.

211. Siepman TA, Bettink-Remeijer MW and Hintzen RQ. Retinal nerve fiber layer thickness in subgroups of multiple sclerosis, measured by optical coherence tomography and scanning laser polarimetry. *J Neurol*. 2010; 257: 1654-60.

212. Saidha S, Syc SB, Ibrahim MA, et al. Primary retinal pathology in multiple sclerosis as detected by optical coherence tomography. *Brain*. 2011; 134: 518-33.

213. Sun SW, Nishioka C, Chung CF, Park J and Liang HF. Anterograde-propagation of axonal degeneration in the visual system of wlds mice characterized by diffusion tensor imaging. *J Magn Reson Imaging*. 2017; 45: 482-91.

214. Dysli C, Enzmann V, Sznitman R and Zinkernagel MS. Quantitative Analysis of Mouse Retinal Layers Using Automated Segmentation of Spectral Domain Optical Coherence Tomography Images. *Transl Vis Sci Technol*. 2015; 4: 9.

215. Budenz DL, Anderson DR, Varma R, et al. Determinants of normal retinal nerve fiber layer thickness measured by Stratus OCT. *Ophthalmology*. 2007; 114: 1046-52.

216. Seigo MA, Sotirchos ES, Newsome S, et al. In vivo assessment of retinal neuronal layers in multiple sclerosis with manual and automated optical coherence tomography segmentation techniques. *J Neurol*. 2012; 259: 2119-30.

217. Schutze C, Ahlers C, Sacu S, et al. Performance of OCT segmentation procedures to assess morphology and extension in geographic atrophy. *Acta Ophthalmol*. 2011; 89: 235-40.

218. Kupersmith MJ, Mandel G, Anderson S, Meltzer DE and Kardon R. Baseline, one and three month changes in the peripapillary retinal nerve fiber layer in acute optic neuritis: relation to baseline vision and MRI. *J Neurol Sci*. 2011; 308: 117-23.

219. Costello F, Coupland S, Hodge W, et al. Quantifying axonal loss after optic neuritis with optical coherence tomography. *Ann Neurol*. 2006; 59: 963-9.

220. Manogaran P, Walker-Egger C, Samardzija M, et al. Exploring experimental autoimmune optic neuritis using multimodal imaging. *Neuroimage*. 2018; 175: 327-39.

221. Knier B, Rothhammer V, Heink S, et al. Neutralizing IL-17 protects the optic nerve from autoimmune pathology and prevents retinal nerve fiber layer atrophy during experimental autoimmune encephalomyelitis. *J Autoimmun*. 2015; 56: 34-44.

222. Zhang HK, Ye Y, Zhao ZN, et al. Neuroprotective effects of gypenosides in experimental autoimmune optic neuritis. *Int J Ophthalmol*. 2017; 10: 541-9.

223. Hein K, Gadjanski I, Kretzschmar B, et al. An optical coherence tomography study on degeneration of retinal nerve fiber layer in rats with autoimmune optic neuritis. *Invest Ophthalmol Vis Sci*. 2012; 53: 157-63.

224. Naismith RT, Xu J, Tutlam NT, et al. Disability in optic neuritis correlates with diffusion tensor-derived directional diffusivities. *Neurology*. 2009; 72: 589-94.

225. Naismith RT, Xu J, Tutlam NT, Trinkaus K, Cross AH and Song SK. Radial diffusivity in remote optic neuritis discriminates visual outcomes. *Neurology*. 2010; 74: 1702-10.

226. Klawiter EC, Schmidt RE, Trinkaus K, et al. Radial diffusivity predicts demyelination in ex vivo multiple sclerosis spinal cords. *Neuroimage*. 2011; 55: 1454-60.

227. van der Walt A, Kolbe SC, Wang YE, et al. Optic nerve diffusion tensor imaging after acute optic neuritis predicts axonal and visual outcomes. *PLoS One*. 2013; 8: e83825.

228. Naismith RT, Xu J, Tutlam NT, et al. Diffusion tensor imaging in acute optic neuropathies: predictor of clinical outcomes. *Arch Neurol*. 2012; 69: 65-71.

229. Ferguson B, Matyszak MK, Esiri MM and Perry VH. Axonal damage in acute multiple sclerosis lesions. *Brain*. 1997; 120 (Pt 3): 393-9.

230. Pfeifenbring S, Bunyan RF, Metz I, et al. Extensive acute axonal damage in pediatric multiple sclerosis lesions. *Ann Neurol*. 2015; 77: 655-67.

231. Smith SA, Williams ZR, Ratchford JN, et al. Diffusion tensor imaging of the optic nerve in multiple sclerosis: association with retinal damage and visual disability. *AJNR Am J Neuroradiol*. 2011; 32: 1662-8.

232. Frohman EM, Dwyer MG, Frohman T, et al. Relationship of optic nerve and brain conventional and non-conventional MRI measures and retinal nerve fiber layer thickness, as assessed by OCT and GDx: a pilot study. *J Neurol Sci*. 2009; 282: 96-105.

233. Shao H, Huang Z, Sun SL, Kaplan HJ and Sun D. Myelin/oligodendrocyte glycoprotein-specific T-cells induce severe optic neuritis in the C57BL/6 mouse. *Invest Ophthalmol Vis Sci*. 2004; 45: 4060-5.

234. Quinn TA, Dutt M and Shindler KS. Optic neuritis and retinal ganglion cell loss in a chronic murine model of multiple sclerosis. *Front Neurol*. 2011; 2: 50.

235. Horstmann L, Schmid H, Heinen AP, Kurschus FC, Dick HB and Joachim SC. Inflammatory demyelination induces glia alterations and ganglion cell loss in the retina of an experimental autoimmune encephalomyelitis model. *J Neuroinflammation*. 2013; 10: 120.

236. Green AJ, McQuaid S, Hauser SL, Allen IV and Lyness R. Ocular pathology in multiple sclerosis: retinal atrophy and inflammation irrespective of disease duration. *Brain*. 2010; 133: 1591-601.

237. Nickells RW. The cell and molecular biology of glaucoma: mechanisms of retinal ganglion cell death. *Invest Ophthalmol Vis Sci*. 2012; 53: 2476-81.

238. Janssen KT, Mac Nair CE, Dietz JA, Schlamp CL and Nickells RW. Nuclear atrophy of retinal ganglion cells precedes the bax-dependent stage of apoptosis. *Invest Ophthalmol Vis Sci*. 2013; 54: 1805-15.

239. Weber AJ, Kaufman PL and Hubbard WC. Morphology of single ganglion cells in the glaucomatous primate retina. *Invest Ophthalmol Vis Sci*. 1998; 39: 2304-20.

240. Weber AJ, Harman CD and Viswanathan S. Effects of optic nerve injury, glaucoma, and neuroprotection on the survival, structure, and function of ganglion cells in the mammalian retina. *J Physiol*. 2008; 586: 4393-400.

241. Hernandez-Enriquez B, Arellano RO and Moran J. Role for ionic fluxes on cell death and apoptotic volume decrease in cultured cerebellar granule neurons. *Neuroscience*. 2010; 167: 298-311.

242. Bortner CD and Cidlowski JA. Cell shrinkage and monovalent cation fluxes: role in apoptosis. *Arch Biochem Biophys*. 2007; 462: 176-88.

243. Salapa HE, Lee S, Shin Y and Levin MC. Contribution of the Degeneration of the Neuro-Axonal Unit to the Pathogenesis of Multiple Sclerosis. *Brain Sci*. 2017; 7.

244. Huberman AD and Niell CM. What can mice tell us about how vision works? *Trends Neurosci*. 2011; 34: 464-73.

245. Ishihara T, Hong M, Zhang B, et al. Age-dependent emergence and progression of a tauopathy in transgenic mice overexpressing the shortest human tau isoform. *Neuron*. 1999; 24: 751-62.

246. Zhang B, Higuchi M, Yoshiyama Y, et al. Retarded axonal transport of R406W mutant tau in transgenic mice with a neurodegenerative tauopathy. *J Neurosci*. 2004; 24: 4657-67.

247. Stokin GB, Lillo C, Falzone TL, et al. Axonopathy and transport deficits early in the pathogenesis of Alzheimer's disease. *Science*. 2005; 307: 1282-8.

248. Guo X, Macleod GT, Wellington A, et al. The GTPase dMiro is required for axonal transport of mitochondria to Drosophila synapses. *Neuron*. 2005; 47: 379-93.

249. Lasek RJ, Garner JA and Brady ST. Axonal transport of the cytoplasmic matrix. *J Cell Biol*. 1984; 99: 212s-21s.

250. Narita K, Kawasaki F and Kita H. Mn and Mg influxes through Ca channels of motor nerve terminals are prevented by verapamil in frogs. *Brain Res*. 1990; 510: 289-95.

251. Merritt JE, Jacob R and Hallam TJ. Use of manganese to discriminate between calcium influx and mobilization from internal stores in stimulated human neutrophils. *J Biol Chem*. 1989; 264: 1522-7.

252. Pautler RG. Biological applications of manganese-enhanced magnetic resonance imaging. *Methods Mol Med*. 2006; 124: 365-86.

253. Pautler RG. In vivo, trans-synaptic tract-tracing utilizing manganese-enhanced magnetic resonance imaging (MEMRI). *NMR Biomed*. 2004; 17: 595-601.

254. Smith KD, Kallhoff V, Zheng H and Pautler RG. In vivo axonal transport rates decrease in a mouse model of Alzheimer's disease. *Neuroimage*. 2007; 35: 1401-8.

255. Xiao AW, He J, Wang Q, et al. The origin and development of plaques and phosphorylated tau are associated with axonopathy in Alzheimer's disease. *Neurosci Bull*. 2011; 27: 287-99.

256. Dai J, Buijs RM, Kamphorst W and Swaab DF. Impaired axonal transport of cortical neurons in Alzheimer's disease is associated with neuropathological changes. *Brain Res*. 2002; 948: 138-44.

257. Adalbert R, Nogradi A, Babetto E, et al. Severely dystrophic axons at amyloid plaques remain continuous and connected to viable cell bodies. *Brain*. 2009; 132: 402-16.

258. Christensen DZ, Huettenrauch M, Mitkovski M, Pradier L and Wirths O. Axonal degeneration in an Alzheimer mouse model is PS1 gene dose dependent and linked to intraneuronal Abeta accumulation. *Front Aging Neurosci*. 2014; 6: 139.

259. Hasan KM and Narayana PA. Computation of the fractional anisotropy and mean diffusivity maps without tensor decoding and diagonalization: Theoretical analysis and validation. *Magn Reson Med*. 2003; 50: 589-98.

260. Lin TH, Kim JH, Perez-Torres C, et al. Axonal transport rate decreased at the onset of optic neuritis in EAE mice. *Neuroimage*. 2014; 100: 244-53.

261. Massaad CA, Amin SK, Hu L, Mei Y, Klann E and Pautler RG. Mitochondrial superoxide contributes to blood flow and axonal transport deficits in the Tg2576 mouse model of Alzheimer's disease. *PLoS One*. 2010; 5: e10561.

262. Wang FH, Appelkvist P, Klason T, et al. Decreased axonal transport rates in the Tg2576 APP transgenic mouse: improvement with the gamma-secretase inhibitor MRK-560 as detected by manganese-enhanced MRI. *Eur J Neurosci*. 2012; 36: 3165-72.

263. Kim JH, Budde MD, Liang HF, et al. Detecting axon damage in spinal cord from a mouse model of multiple sclerosis. *Neurobiol Dis*. 2006; 21: 626-32.

264. Mac Donald CL, Dikranian K, Song SK, Bayly PV, Holtzman DM and Brody DL. Detection of traumatic axonal injury with diffusion tensor imaging in a mouse model of traumatic brain injury. *Exp Neurol*. 2007; 205: 116-31.

265. Bennett RE, Mac Donald CL and Brody DL. Diffusion tensor imaging detects axonal injury in a mouse model of repetitive closed-skull traumatic brain injury. *Neurosci Lett*. 2012; 513: 160-5.

266. Xie M, Tobin JE, Budde MD, et al. Rostrocaudal analysis of corpus callosum demyelination and axon damage across disease stages refines diffusion tensor imaging correlations with pathological features. *J Neuropathol Exp Neurol*. 2010; 69: 704-16.

267. Budde MD, Xie M, Cross AH and Song SK. Axial diffusivity is the primary correlate of axonal injury in the experimental autoimmune encephalomyelitis spinal cord: a quantitative pixelwise analysis. *J Neurosci*. 2009; 29: 2805-13.

268. Bazarian JJ, Zhong J, Blyth B, Zhu T, Kavcic V and Peterson D. Diffusion tensor imaging detects clinically important axonal damage after mild traumatic brain injury: a pilot study. *J Neurotrauma*. 2007; 24: 1447-59.

269. Wilde EA, McCauley SR, Hunter JV, et al. Diffusion tensor imaging of acute mild traumatic brain injury in adolescents. *Neurology*. 2008; 70: 948-55.

270. Bazarian JJ, Zhu T, Blyth B, Borrino A and Zhong J. Subject-specific changes in brain white matter on diffusion tensor imaging after sports-related concussion. *Magn Reson Imaging*. 2012; 30: 171-80.

271. Edgar JM, McLaughlin M, Yool D, et al. Oligodendroglial modulation of fast axonal transport in a mouse model of hereditary spastic paraplegia. *J Cell Biol*. 2004; 166: 121-31.

272. Sun J, Zhou H, Bai F, Ren Q and Zhang Z. Myelin injury induces axonal transport impairment but not AD-like pathology in the hippocampus of cuprizone-fed mice. *Oncotarget*. 2016; 7: 30003-17.

273. Beirowski B, Babetto E and Wrabetz L. Axon degeneration: Linking axonal bioenergetics to myelin. *J Cell Biol*. 2016; 215: 437-40.

274. Dixit R, Ross JL, Goldman YE and Holzbaur EL. Differential regulation of dynein and kinesin motor proteins by tau. *Science*. 2008; 319: 1086-9.

275. Lin WL, Lewis J, Yen SH, Hutton M and Dickson DW. Filamentous tau in oligodendrocytes and astrocytes of transgenic mice expressing the human tau isoform with the P301L mutation. *Am J Pathol*. 2003; 162: 213-8.

276. Maurin H, Chong SA, Kraev I, et al. Early structural and functional defects in synapses and myelinated axons in stratum lacunosum moleculare in two preclinical models for tauopathy. *PLoS One*. 2014; 9: e87605.

277. Higuchi M, Zhang B, Forman MS, Yoshiyama Y, Trojanowski JQ and Lee VM. Axonal degeneration induced by targeted expression of mutant human tau in oligodendrocytes of transgenic mice that model glial tauopathies. *J Neurosci*. 2005; 25: 9434-43.

278. Yoshita M, Fletcher E, Harvey D, et al. Extent and distribution of white matter hyperintensities in normal aging, MCI, and AD. *Neurology*. 2006; 67: 2192-8.

279. McAleese KE, Firbank M, Dey M, et al. Cortical tau load is associated with white matter hyperintensities. *Acta Neuropathol Commun*. 2015; 3: 60.

280. Nir TM, Jahanshad N, Villalon-Reina JE, et al. Effectiveness of regional DTI measures in distinguishing Alzheimer's disease, MCI, and normal aging. *Neuroimage-Clin*. 2013; 3: 180-95.

281. Liu Y, Spulber G, Lehtimaki KK, et al. Diffusion tensor imaging and tract-based spatial statistics in Alzheimer's disease and mild cognitive impairment. *Neurobiol Aging*. 2011; 32: 1558-71.

282. Masliah E, Mallory M, Hansen L, Alford M, DeTeresa R and Terry R. An antibody against phosphorylated neurofilaments identifies a subset of damaged association axons in Alzheimer's disease. *Am J Pathol*. 1993; 142: 871-82.

283. Mitew S, Kirkcaldie MT, Halliday GM, Shepherd CE, Vickers JC and Dickson TC. Focal demyelination in Alzheimer's disease and transgenic mouse models. *Acta Neuropathol*. 2010; 119: 567-77.

284. Benes FM, Farol PA, Majocha RE, Marotta CA and Bird ED. Evidence for axonal loss in regions occupied by senile plaques in Alzheimer cortex. *Neuroscience*. 1991; 42: 651-60.

285. De Vos KJ, Grierson AJ, Ackerley S and Miller CC. Role of axonal transport in neurodegenerative diseases. *Annu Rev Neurosci*. 2008; 31: 151-73.

286. Vana L, Kanaan NM, Ugwu IC, Wuu J, Mufson EJ and Binder LI. Progression of tau pathology in cholinergic Basal forebrain neurons in mild cognitive impairment and Alzheimer's disease. *Am J Pathol*. 2011; 179: 2533-50.

287. Ghoshal N, Garcia-Sierra F, Wuu J, et al. Tau conformational changes correspond to impairments of episodic memory in mild cognitive impairment and Alzheimer's disease. *Exp Neurol*. 2002; 177: 475-93.

288. Guo H, Albrecht S, Bourdeau M, Petzke T, Bergeron C and LeBlanc AC. Active caspase-6 and caspase-6-cleaved tau in neuropil threads, neuritic plaques, and neurofibrillary tangles of Alzheimer's disease. *Am J Pathol*. 2004; 165: 523-31.

289. Uribe V, Wong BK, Graham RK, et al. Rescue from excitotoxicity and axonal degeneration accompanied by age-dependent behavioral and neuroanatomical alterations in caspase-6-deficient mice. *Hum Mol Genet*. 2012; 21: 1954-67.

290. Pooler AM, Polydoro M, Maury EA, et al. Amyloid accelerates tau propagation and toxicity in a model of early Alzheimer's disease. *Acta Neuropathol Commun*. 2015; 3: 14.

291. Ahmed Z, Cooper J, Murray TK, et al. A novel in vivo model of tau propagation with rapid and progressive neurofibrillary tangle pathology: the pattern of spread is determined by connectivity, not proximity. *Acta Neuropathol*. 2014; 127: 667-83.

292. Bennett RE, DeVos SL, Dujardin S, et al. Enhanced Tau Aggregation in the Presence of Amyloid beta. *Am J Pathol*. 2017; 187: 1601-12.

293. Selenica ML, Brownlow M, Jimenez JP, et al. Amyloid oligomers exacerbate tau pathology in a mouse model of tauopathy. *Neurodegener Dis*. 2013; 11: 165-81.

294. Bolmont T, Clavaguera F, Meyer-Luehmann M, et al. Induction of tau pathology by intracerebral infusion of amyloid-beta -containing brain extract and by amyloid-beta deposition in APP x Tau transgenic mice. *Am J Pathol*. 2007; 171: 2012-20.

295. Ho WL, Leung Y, Cheng SS, et al. Investigating degeneration of the retina in young and aged tau P301L mice. *Life Sci*. 2015; 124: 16-23.

296. Coleman JE, Law K and Bear MF. Anatomical origins of ocular dominance in mouse primary visual cortex. *Neuroscience*. 2009; 161: 561-71.

297. Drager UC and Olsen JF. Origins of crossed and uncrossed retinal projections in pigmented and albino mice. *J Comp Neurol*. 1980; 191: 383-412.

298. Zago W, Buttini M, Comery TA, et al. Neutralization of soluble, synaptotoxic amyloid beta species by antibodies is epitope specific. *J Neurosci*. 2012; 32: 2696-702.

299. Shin RW, Iwaki T, Kitamoto T, Sato Y and Tateishi J. Massive accumulation of modified tau and severe depletion of normal tau characterize the cerebral cortex and white matter of Alzheimer's disease. Demonstration using the hydrated autoclaving method. *Am J Pathol*. 1992; 140: 937-45.

300. Umahara T, Tsuchiya K, Ikeda K, et al. Demonstration and distribution of tau-positive glial coiled body-like structures in white matter and white matter threads in early onset Alzheimer's disease. *Neuropathology*. 2002; 22: 9-12.

301. Kowall NW and Kosik KS. Axonal disruption and aberrant localization of tau protein characterize the neuropil pathology of Alzheimer's disease. *Ann Neurol*. 1987; 22: 639-43.

302. Brun A and Englund E. A white matter disorder in dementia of the Alzheimer type: a pathoanatomical study. *Ann Neurol*. 1986; 19: 253-62.

303. Scheltens P, Barkhof F, Leys D, Wolters EC, Ravid R and Kamphorst W. Histopathologic correlates of white matter changes on MRI in Alzheimer's disease and normal aging. *Neurology*. 1995; 45: 883-8.

304. Bosch B, Arenaza-Urquijo EM, Rami L, et al. Multiple DTI index analysis in normal aging, amnestic MCI and AD. Relationship with neuropsychological performance. *Neurobiol Aging*. 2012; 33: 61-74.

305. Schmierer K, Wheeler-Kingshott CA, Tozer DJ, et al. Quantitative magnetic resonance of postmortem multiple sclerosis brain before and after fixation. *Magn Reson Med*. 2008; 59: 268-77.

306. Gouw AA, Seewann A, Vrenken H, et al. Heterogeneity of white matter hyperintensities in Alzheimer's disease: post-mortem quantitative MRI and neuropathology. *Brain*. 2008; 131: 3286-98.

307. Singh S, Dallenga T, Winkler A, et al. Relationship of acute axonal damage, Wallerian degeneration, and clinical disability in multiple sclerosis. *J Neuroinflammation*. 2017; 14: 57.

308. Ljungberg MC, Ali YO, Zhu J, et al. CREB-activity and nmnat2 transcription are down-regulated prior to neurodegeneration, while NMNAT2 over-expression is neuroprotective, in a mouse model of human tauopathy. *Hum Mol Genet*. 2012; 21: 251-67.

309. Ali YO, Ruan K and Zhai RG. NMNAT suppresses tau-induced neurodegeneration by promoting clearance of hyperphosphorylated tau oligomers in a Drosophila model of tauopathy. *Hum Mol Genet*. 2012; 21: 237-50.

310. Kneynsberg A, Combs B, Christensen K, Morfini G and Kanaan NM. Axonal Degeneration in Tauopathies: Disease Relevance and Underlying Mechanisms. *Front Neurosci*. 2017; 11: 572.

311. Bambo MP, Garcia-Martin E, Pinilla J, et al. Detection of retinal nerve fiber layer degeneration in patients with Alzheimer's disease using optical coherence tomography: searching new biomarkers. *Acta Ophthalmol*. 2014; 92: e581-2.

312. Coppola G, Di Renzo A, Ziccardi L, et al. Optical Coherence Tomography in Alzheimer's Disease: A Meta-Analysis. *PLoS One*. 2015; 10: e0134750.

313. Matsuoka Y, Gray AJ, Hirata-Fukae C, et al. Intranasal NAP administration reduces accumulation of amyloid peptide and tau hyperphosphorylation in a transgenic mouse model of Alzheimer's disease at early pathological stage. *J Mol Neurosci*. 2007; 31: 165-70.

314. Matsuoka Y, Jouroukhin Y, Gray AJ, et al. A neuronal microtubule-interacting agent, NAPVSIPQ, reduces tau pathology and enhances cognitive function in a mouse model of Alzheimer's disease. *J Pharmacol Exp Ther*. 2008; 325: 146-53.

315. Mayo CD, Mazerolle EL, Ritchie L, Fisk JD and Gawryluk JR. Longitudinal changes in microstructural white matter metrics in Alzheimer's disease. *Neuroimage Clin*. 2017; 13: 330-8.

316. McAleese KE, Walker L, Graham S, et al. Parietal white matter lesions in Alzheimer's disease are associated with cortical neurodegenerative pathology, but not with small vessel disease. *Acta Neuropathol*. 2017; 134: 459-73.

317. Huang J, Friedland RP and Auchus AP. Diffusion tensor imaging of normal-appearing white matter in mild cognitive impairment and early Alzheimer disease: preliminary evidence of axonal degeneration in the temporal lobe. *AJNR Am J Neuroradiol*. 2007; 28: 1943-8.

318. Montagne A, Barnes SR, Sweeney MD, et al. Blood-brain barrier breakdown in the aging human hippocampus. *Neuron*. 2015; 85: 296-302.

319. van de Haar HJ, Burgmans S, Jansen JF, et al. Blood-Brain Barrier Leakage in Patients with Early Alzheimer Disease. *Radiology*. 2016; 281: 527-35.

320. Tang-Schomer MD, Johnson VE, Baas PW, Stewart W and Smith DH. Partial interruption of axonal transport due to microtubule breakage accounts for the formation of periodic varicosities after traumatic axonal injury. *Exp Neurol*. 2012; 233: 364-72.

321. Makani V, Zhang B, Han H, et al. Evaluation of the brain-penetrant microtubule-stabilizing agent, dictyostatin, in the PS19 tau transgenic mouse model of tauopathy. *Acta Neuropathol Commun*. 2016; 4: 106.

322. Rapoport M, Dawson HN, Binder LI, Vitek MP and Ferreira A. Tau is essential to beta -amyloid-induced neurotoxicity. *Proc Natl Acad Sci U S A*. 2002; 99: 6364-9.